

Erbium implanted thin film photonic materials

A. Polman^{a)}*FOM-Institute for Atomic and Molecular Physics, Kruislaan 407, 1098 SJ Amsterdam, The Netherlands*

(Received 16 September 1996; accepted for publication 4 March 1997)

Erbium doped materials are of great interest in thin film integrated optoelectronic technology, due to their Er^{3+} intra-4*f* emission at $1.54\ \mu\text{m}$, a standard telecommunication wavelength. Er-doped dielectric thin films can be used to fabricate planar optical amplifiers or lasers that can be integrated with other devices on the same chip. Semiconductors, such as silicon, can also be doped with erbium. In this case the Er may be excited through optically or electrically generated charge carriers. Er-doped Si light-emitting diodes may find applications in Si-based optoelectronic circuits. In this article, the synthesis, characterization, and application of several different Er-doped thin film photonic materials is described. It focuses on oxide glasses (pure SiO_2 , phosphosilicate, borosilicate, and soda-lime glasses), ceramic thin films (Al_2O_3 , Y_2O_3 , LiNbO_3), and amorphous and crystalline silicon, all doped with Er by ion implantation. MeV ion implantation is a technique that is ideally suited to dope these materials with Er as the ion range corresponds to the typical micron dimensions of these optical materials. The role of implantation defects, the effect of annealing, concentration dependent effects, and optical activation are discussed and compared for the various materials. © 1997 American Institute of Physics. [S0021-8979(97)07013-8]

TABLE OF CONTENTS

I. Introduction.	1	c. Ion beam induced epitaxial recrystallization.	28
II. Erbium Ion Implantation and Optical Characterization.	3	2. Optical activation and codoping.	28
A. Er implantation.	3	a. PL spectra and annealing behavior.	28
B. Optical characterization.	4	b. Er excitation.	29
III. Silica Glasses.	5	c. Maximum active Er concentration in CZ-Si.	29
A. Pure silica.	5	d. Erbium configuration in Si.	30
1. Optical activation of Er.	5	e. Quantum efficiency.	30
2. Er^{3+} as a probe for ion irradiation damage.	6	f. Luminescence quenching.	30
B. Phosphosilicate glass.	7	3. Electroluminescence.	32
C. Soda-lime silicate glass.	7	B. Amorphous Si.	33
D. Local environment of Er.	10	1. Optical activation.	33
E. Upconversion and optical gain estimates.	11	a. LPCVD <i>a</i> -Si.	33
F. Spontaneous emission near a dielectric interface.	14	b. PECVD <i>a</i> -Si.	34
IV. Al_2O_3 , Y_2O_3	15	c. Porous Si.	35
A. Optical activation.	15	2. Electroluminescence.	35
B. Absorption and emission cross sections.	17	VII. Other Materials and Other Rare-Earth Ions.	36
C. Upconversion in Al_2O_3	17	A. Er-implanted waveguide films.	36
D. Upconversion in Y_2O_3	20	B. Er-implanted Si.	36
E. Optical gain in Al_2O_3	21	VIII. Conclusions.	37
F. Optical mode imaging.	22		
V. LiNbO_3	23		
A. Amorphization and recrystallization.	23		
B. Optical activation.	25		
VI. Silicon.	26		
A. Crystal Si.	26		
1. Incorporation.	26		
a. Solid phase crystallization and segregation.	26		
b. Impurity effects.	27		

I. INTRODUCTION

Optical technologies are becoming more and more important in areas that have traditionally been the domain of electronics. The enormous bandwidth that is available using optical communication enables data information transfer and processing at rates that are orders of magnitude higher than what is the limit of electronic technologies. For example, a $1.5\ \mu\text{m}$ optical signal with a bandwidth of 8 nm has a cor-

^{a)}Electronic mail: polman@amolf.nl, <http://www.amolf.nl>

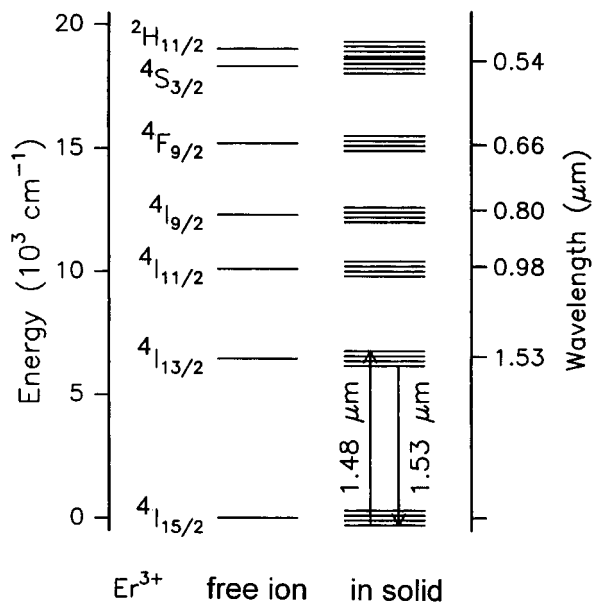


FIG. 1. Schematic energy level diagram of Er^{3+} . In the free ion the energy levels are sharp; in a solid the levels are split due to the Stark effect. Pump ($1.48 \mu\text{m}$) and signal ($1.53 \mu\text{m}$) wavelengths are indicated, together with the Russell-Saunders notation of the energy levels.

responding optical frequency bandwidth of 10^{12} Hz (1 THz). To fully exploit such high frequencies, it is important to develop new materials that can be used for the generation, guiding, switching, and amplification of light. Such materials can then be used in components in the optical communication network.

Rare-earth ions, specifically erbium, have played an important role in the development of optical communication technology in the past few years. Trivalent erbium (the preferred bonding state) has an incomplete $4f$ electronic shell that is shielded from the outer world by closed $5s$ and $5p$ shells.¹ As a result, rather sharp optical intra- $4f$ transitions can be achieved from erbium doped materials. The transition from the first excited state to the ground state in Er^{3+} occurs at an energy of 0.8 eV, corresponding to a wavelength of $1.54 \mu\text{m}$. This is an important telecommunication wavelength since standard silica-based optical fibers have their maximum transparency at this wavelength. An energy level diagram for Er^{3+} is plotted in Fig. 1, which also shows the Stark splitting of the Er manifolds, due to the electric field in the host.

In 1987 it was discovered^{2,3} that Er-doped silica fibers could be used as optical amplifiers⁴⁻⁶ operating at $1.54 \mu\text{m}$. A continuous pump laser is used to create population inversion between the ground and first excited state in Er^{3+} , whereupon stimulated emission can serve to amplify a high frequency telecommunication signal at $1.54 \mu\text{m}$. Such optical amplifiers are necessary to compensate for the losses in the processing and distribution of optical signals, while maintaining the high bandwidth and low crosstalk. Erbium-doped optical amplifiers can show a linear gain response, temperature and polarization insensitivity, and low noise.⁶ It is mostly due to the availability of Er-doped fiber amplifiers

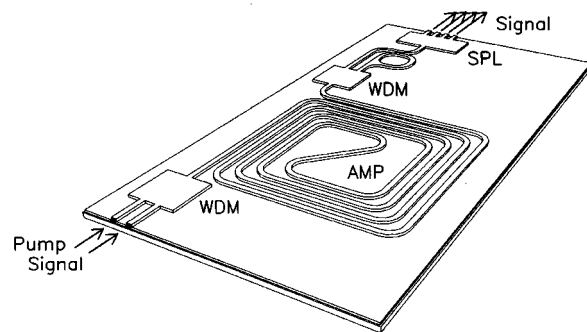


FIG. 2. Schematic of a planar optical amplifier (AMP) integrated with a 1×4 splitter (SPL) on a planar substrate. Wavelength division multiplexers (WDMs) to couple the pump and signal are also integrated. In this device the amplifier spiral serves to compensate for the fourfold intensity loss due to the splitting.

that optical telecommunication networks are as well developed as they are today, and the Er transition at $1.5 \mu\text{m}$ has clearly set the telecommunication wavelength standard at $1.5 \mu\text{m}$.⁷ Recently, a multiwavelength optical signal transmission rate as high as 100 Gbits/s was demonstrated in a 6300-km-long fiber link with fiber amplifiers to compensate for the signal attenuation after each 45 km section of fiber.⁸ Practical pump wavelengths for Er-doped materials are 980 nm, at which relatively inexpensive lasers are commercially available, or $1.48 \mu\text{m}$. In the latter case, a quasitwo-level system is achieved.

A logical next step in optical amplifier development is the planar amplifier, in which Er-doped channel waveguides are made on a planar substrate. Planar amplifiers offer the important advantage that they can be integrated with other waveguide devices such as splitters, switches, or multiplexers on a single chip. A schematic example of such a structure is given in Fig. 2, which shows a 1×4 splitter (SPL), combined with an Er-doped amplifier (AMP) section, which compensates for the fourfold intensity loss after the splitter. The waveguide is rolled up in a spiral geometry in order to fit onto a small area (typically mm^2). Wavelength division multiplexers are used to couple and decouple the signal and pump beams.

The radiative lifetime of the first excited state of Er^{3+} is usually in the millisecond range, depending on the material. As a result, the emission and absorption cross sections are relatively small (typically 10^{-21} – 10^{-20} cm^2). Therefore reasonable values of optical gain (~ 3 dB, a factor of 2) can only be reached when the signal beam encounters a large amount of excited Er^{3+} (10^{20} – 10^{21} Er/cm^2). Given the small length of a planar amplifier (compared to a typically 20-m-long Er-doped fiber amplifier) a high Er density, typically in the range of 0.1–1 at. %, is required. At such high Er concentrations, the distance between the Er ions is small and electric dipole-dipole interactions between excited Er^{3+} ions can reduce the gain performance of the amplifier.

In order to synthesize and optimize planar Er-doped waveguide films it is essential to study materials issues such as luminescence spectra, lifetimes, concentration dependence, and quenching effects, nonlinear upconversion ef-

fects, interactions with defects and impurities, and annealing behavior as well as quantum electrodynamic effects on spontaneous emission. This article reviews our work over the past six years on the synthesis of several Er-doped thin films using ion implantation.⁹ Results on several different silica glasses, ceramic oxide thin films (Al_2O_3 , Y_2O_3), as well as an electro-optic material (LiNbO_3) are studied and compared.

Erbium doping of silicon has also become an intensively studied subject. If efficient light emission from Er in Si could be achieved, the integration of electrical and optical functions on a single Si chip may be realized. This article also reviews our recent work on Er-doped silicon. A more extensive review on Er-doped Si will appear elsewhere.¹⁰ A complete record of the state of the art in rare-earth doped semiconductor research can be found in Ref. 11.

In this review we focus on ion implanted materials only, since several materials issues, including the effect of implantation defects, annealing behavior, diffusion, and optical activation, are specific to ion implantation. However, many issues that are discussed also apply to other methods. The aim of this review is to assemble and compare work done in this area in the past several years by the author and co-workers. It should be noted that several other research groups have contributed to work on Er-doped optical waveguide materials and silicon. A brief description of that work and a list of references are given near the end of this article.

In Sec. II, experimental techniques required for the fabrication and optical characterization of Er-implanted thin films are listed. Er ion sources and the details of photoluminescence spectroscopy equipment are described. In Sec. III, various silica glasses are doped with Er by implantation at energies in the range 400 keV–5.0 MeV. The annealing behavior and the effect of radiation damage on the Er^{3+} luminescence are discussed. Due to concentration quenching effects the luminescence lifetime is strongly dependent on Er concentration; it ranges from 1 to 15 ms. Extended x-ray absorption fine structure measurements show that in these silica glasses Er is bound to four to six oxygen atoms as first neighbors. Er-implanted channel waveguides in soda-lime glass show upconversion effects due to interactions between excited Er^{3+} ions, and the upconversion coefficient is determined. Upconversion limits the optical gain performance, and pump powers >100 mW are required to reach the net gain in these glasses. Also, quantum electrodynamic effects on the spontaneous emission rate of Er^{3+} near a dielectric interface are investigated.

Section IV describes Er implantation into polycrystalline Al_2O_3 thin films. By thermal annealing, Er concentrations up to 1 at. % can be optically activated in this material and have a luminescence lifetime of 4–8 ms. Miniature channel waveguide structures are made; these have much better confined optical modes than those in silica glass due to the high refractive index of Al_2O_3 . The Er^{3+} absorption and emission cross section spectra, upconversion coefficient, and excited state absorption cross section are determined. An optimized Er-doped channel waveguide is then designed and fabricated. It shows an optical gain of 2.3 dB when pumped at a power of 9 mW at 1.48 μm . Upconversion luminescence is used in

a new technique to make two-dimensional spatial images of optical modes in a planar waveguide. Er implantation is also performed on Y_2O_3 thin films, which have a similar crystal structure as Al_2O_3 . Er-doped Y_2O_3 waveguides show stronger upconversion than Al_2O_3 , which is due to the long luminescence lifetimes in Y_2O_3 as a result of the low-energy phonon spectrum of this material.

In Sec. V, Er implantation into single crystal LiNbO_3 is discussed. High temperature annealing is required to recrystallize the implantation-amorphized LiNbO_3 crystal. A rather complex recrystallization scenario involving competition between columnar solid phase epitaxy, random nucleation and growth, and polycrystal alignment is derived. Sharply peaked Er^{3+} luminescence spectra with a luminescence lifetime of 2.9 ms are observed. The maximum Er concentration that can be optically activated is 0.18 at. %.

Section VI reviews work on Er implantation into silicon. Crystal Si is easily amorphized by an Er ion beam. Solid phase epitaxy at 600 °C leads to segregation and trapping of up to 2×10^{20} Er/cm³ in the crystal. The segregation and trapping behavior is temperature and concentration dependent. While high Er concentrations can be trapped in the crystal, the maximum Er concentration that can be optically activated in Czochralski-grown Er is only 3×10^{17} Er/cm³, and the excitation quantum efficiency is 10^{-6} . The presence of impurities such as oxygen increases the active Er concentration and the quantum efficiency, and also serves to reduce the luminescence quenching that is observed at temperatures >100 K. An impurity Auger model for the excitation and deexcitation of Er in Si is discussed. Optimized Er-implanted light-emitting diodes codoped with oxygen show room temperature electroluminescence at 1.54 μm with an internal quantum efficiency of 10^{-4} . Experiments are also performed on amorphous Si as this material can accommodate much higher Er concentrations than crystal Si due to its network and its defect structure. By codoping with oxygen, a temperature quenching between 10 and 300 K by only a factor 3 is observed, resulting in clear room temperature emission at 1.54 μm . Er-implanted amorphous Si light-emitting diodes show room temperature electroluminescence with an internal quantum efficiency of 10^{-4} . Porous Si is also implanted with Er, and shows room temperature luminescence, with characteristics similar to those of Er-implanted amorphous Si.

II. ERBIUM ION IMPLANTATION AND OPTICAL CHARACTERIZATION

A. Er implantation

Ion implantation is a convenient way to incorporate Er ions into thin films, as the Er concentration depth profile can be tailored by varying the ion energy and fluence. In this review, experiments were performed using either a 1.7 MV tandem accelerator from National Electrostatics Corporation or a 1 MV single-ended Van de Graaff accelerator from High Voltage Engineering Europa B.V. In the tandem accelerator, ErO^+ ions were extracted in a sputter ion source, using a Cs-covered cathode containing a mixture of Er and Al powders. The negative molecules were dissociated and charge exchanged in a gas-stripper canal in the high-voltage termi-

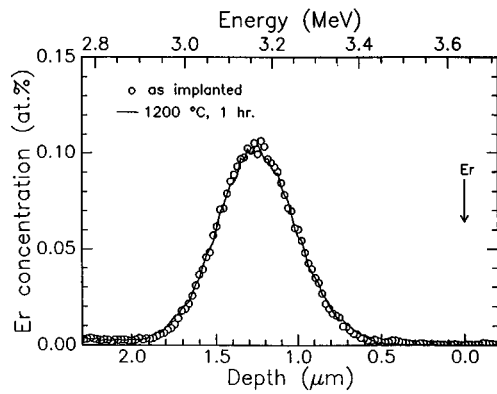


FIG. 3. Erbium part of a Rutherford backscattering spectrum (4 MeV He, scattering angle 170°) for an Er-implanted (3.5 MeV, 5×10^{15} Er/cm²) SiO₂ film. The energy scale on the top axis is converted to a depth scale on the bottom axis. The vertical scale is converted to Er concentration. The Er surface energy (depth=0) is indicated by an arrow. (From Ref. 15.)

nal. In the single-ended machine, positive Er ions were extracted from a sputter ion source with solid Er as a cathode, and a Wien filter at the high-voltage terminal was used for a coarse mass separation before acceleration. For both machines, the accelerated Er⁺ ions were mass selected in a switching magnet. In general, it is difficult to make negatively charged Er ions so that beam currents from a tandem accelerator are usually lower than from a single-ended machine. Er⁺ ion currents up to 10 μA are typical for a Van de Graaff accelerator.

Due to the high stopping cross section, the Er penetration depth in a material is relatively small. Implantation energies of several MeV are required to reach projected ion ranges in the micron range typical of optical waveguide materials. This is illustrated in Fig. 3 which shows an Er depth profile,¹² measured using Rutherford backscattering spectrometry (RBS), of an SiO₂ film implanted with 3.5 MeV Er ions to a total fluence of 5×10^{15} ions/cm². The Er profile peaks at a depth of 1.25 μm and has a full width at half-maximum (FWHM) of 0.56 μm. The corresponding straggle or standard deviation is $\sigma = 0.24$ μm. The peak Er concentration is 0.1 at. %.

SiO₂ films were implanted with Er at different energies in the range 0.25–5 MeV, and the depth distributions were measured using RBS. The Er projected range and straggle derived from these data are plotted in Fig. 4(a) as a function of implantation energy. A roughly linear increase with ion energy is found for both the range and the straggle. This linear increase is due to the fact that for a heavy ion the total energy loss by atomic and electronic collisions is not very dependent on energy in the MeV energy range.

Ion range and straggle were also measured for Er implanted into crystal Si. During implantation, the wafer was tilted 7° off the ion beam direction to avoid channeling. The results are shown in Fig. 4(b), and they show slightly smaller ranges and straggle than they do for SiO₂. This is in agreement with the difference in energy loss in the two materials. A Monte Carlo program named TRIM'89¹³ is often used to estimate depth profiles and straggle after ion implantation. Comparing such calculations with the measured data in Fig.

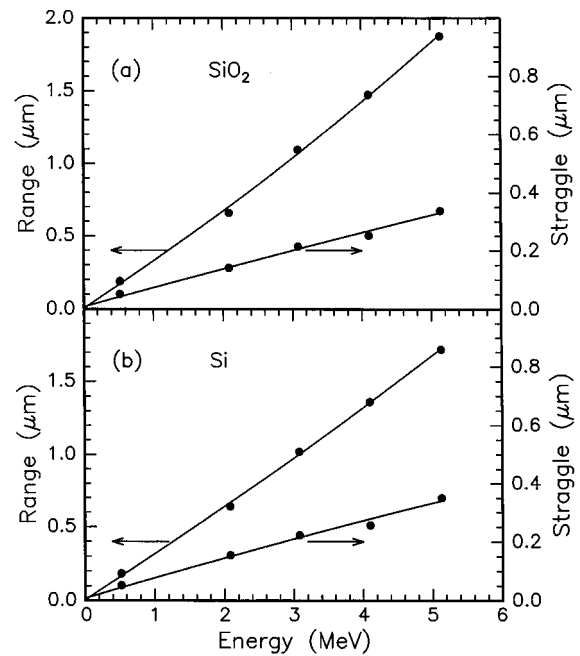


FIG. 4. Ion range and straggle for different Er implantation energies measured using RBS for (a) SiO₂ thin films and (b) crystal Si.

4, it is found that TRIM'89 underestimates both range and straggle by up to a factor of 2.

B. Optical characterization

Photoluminescence spectroscopy measurements were used throughout to optically characterize the Er-implanted films. In most experiments, an Ar ion laser was used as an excitation source since its emission is resonant with the $^4I_{15/2} \rightarrow ^2H_{11/2}$ and $^4I_{15/2} \rightarrow ^4S_{3/2}$ absorption transitions in Er³⁺. Depending on the exact shape of the absorption spectrum, which varies from material to material, a specific laser line (476, 488, 496, 502, or 515 nm) was used to obtain optimum emission. Some experiments were performed using a Ti:sapphire laser that was tuned across the $^4I_{15/2} \rightarrow ^4S_{11/2}$ transition in Er³⁺ around 980 nm. Both Ar laser and Ti:sapphire excitation were performed using near normal incidence of the laser beam to the sample surface. In comparing luminescence intensities among different thin films, it should be realized that the laser beam generates a standing wave pattern in the film. Hence the Er excitation efficiency depends on where the ions are located relative to the node/antinode interference pattern in the waveguide.

Experiments on optical waveguides were performed using excitation with a Philips 1.48 μm InGaAsP diode laser, the output of which was first coupled into one end of an optical fiber. The other (tapered) end was then aligned to the waveguide using piezo-electric actuators. Details of such a setup are reported elsewhere.¹⁴ A HP 8168 laser, tunable around 1.53 μm, was used to generate the signal in the optical gain measurements.

In all experiments, a standard single-grating monochromator was used to disperse the luminescence light onto a detector. A Northcoast EO-817S detector was used for most measurements in the 0.9–1.7 μm wavelength range. It has a

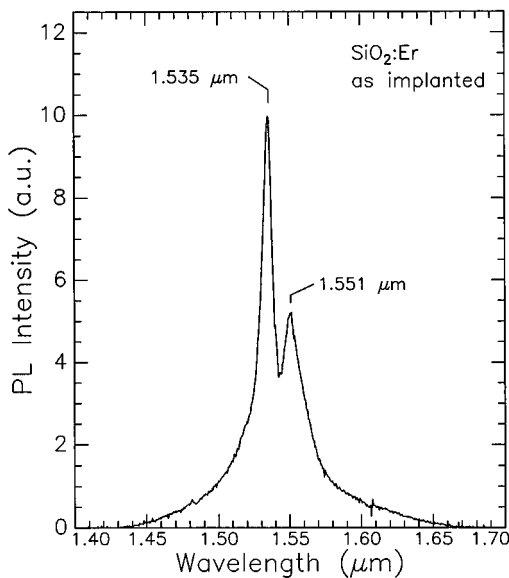


FIG. 5. Room-temperature PL spectrum for an Er-implanted (5×10^{15} Er/cm², 3.5 MeV, peak concentration 0.1 at. %) SiO₂ film on a Si substrate. ($\lambda_{\text{pump}} = 488$ nm, pump power = 250 mW, spectral resolution = 1 nm, from Ref. 15.)

time resolution of 30 μ s, sufficient for most luminescence lifetime measurements. A Northcoast EO-817P detector, with less sensitivity but faster response time (< 1 μ s), was also used. A Hamamatsu 7102 near-infrared sensitive photomultiplier tube was used for measurements in the 0.3–1.1 μ m wavelength range. In addition, an ANDO AQ6312B spectrum analyzer was used for the optical gain measurements.

III. SILICA GLASSES

A. Pure silica

1. Optical activation of Er

Silica glass (amorphous SiO₂) films, 10 μ m thick, were grown on Si(100) substrates by thermal oxidation in a high pressure steam ambient.¹⁵ The films were implanted at room temperature with 5×10^{15} 3.5 MeV Er/cm². The RBS spectrum after implantation is shown in Fig. 3. Thermal annealing was performed for 1 h in a standard tube furnace for temperatures in the range 300–1200 °C. A RBS spectrum after annealing at 1200 °C is also shown in Fig. 3, and it shows no measurable diffusion of Er.

Figure 5 shows a room temperature photoluminescence (PL) spectrum for an as-implanted sample measured with a spectral resolution of 1 nm. An Ar⁺ ion laser (488 nm, 250 mW) was used for excitation. A sharp PL spectrum is observed with a main peak at 1.535 μ m and a side peak at 1.551 μ m. The spectrum is characteristic of $^4I_{13/2} \rightarrow ^4I_{15/2}$ transitions in Er³⁺ (see Fig. 1). The spectral width of the main peak (11 nm FWHM) and the wide tails of the spectrum are a result of Stark splitting of the excited and ground state in the host electric field, plus additional homogeneous and inhomogeneous broadening. The two peaks are the only resolved Stark structure.

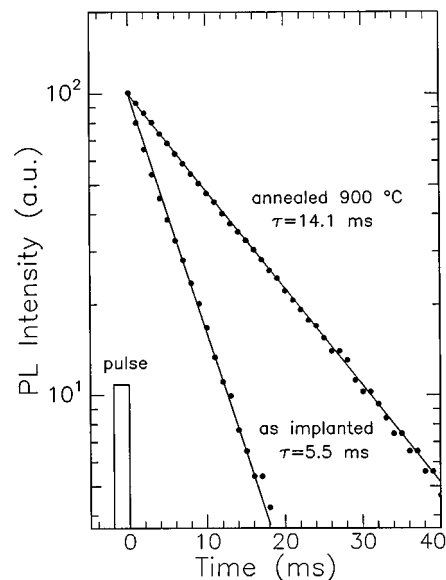


FIG. 6. PL decay measurements at 1.535 μ m, measured at room temperature, of as-implanted (5×10^{15} Er/cm², 3.5 MeV, 0.1 at. % peak) and annealed (900 °C, 1 h) thermally grown SiO₂ films. The timing of the excitation pulse is indicated schematically. (From Ref. 15.)

It is interesting that the as-implanted sample shows a measurable PL intensity at room temperature. This should be compared with results on ceramic oxides or some Er-implanted semiconductors in which an annealing treatment is always necessary to obtain optically active Er³⁺ (see Secs. IV–VI). Apparently, the bonding nature of the SiO₂ network provides the environment for the Er to be incorporated into an active configuration. Recent *in situ* measurements have shown that the effective viscosity of a SiO₂ film during ion irradiation is equal to the thermal viscosity at 1000 °C.¹⁶ The high atomic mobility related to such a low viscosity may be the reason that the Er can find an optically active site in the silica network during irradiation.

Figure 6 shows luminescence lifetime measurements for an as-implanted SiO₂ sample and a sample annealed at 900 °C. In both cases a single-exponential decay is observed. The lifetime for the as-implanted sample is 5.5 ms. Annealing at 900 °C increases the lifetime to 14.1 ms. The lifetime increase is attributed to the annealing of irradiation damage that can couple to the Er³⁺ ion and cause nonradiative decay. Earlier studies have shown that annealing temperatures above 400 °C are required to anneal implantation damage such as dangling bonds and vacancy complexes (e.g., E' and B_2 oxygen vacancy centers) as well as bond angle and length distortions in the silica network.^{17–20}

Figure 7(a) shows the PL peak intensity at 1.535 μ m as a function of annealing temperature. Annealing did not lead to a change in spectral shape. It did lead to an increase in the PL intensity for temperatures up to 900 °C. Lifetime measurements were also made at different annealing temperatures and are plotted in Fig. 7(b). In a simple model the PL intensity is given by

$$I_{\text{PL}} \propto [\text{Er}_{\text{act}}] \frac{\tau}{\tau_{\text{rad}}}, \quad (1)$$

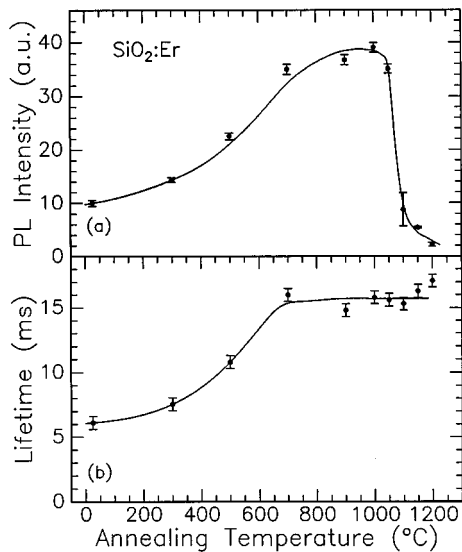


FIG. 7. (a) Room-temperature PL peak intensity and (b) PL lifetime for Er-implanted (5×10^{15} Er/cm², 3.5 MeV, 0.1 at. % peak) thermally grown SiO₂ films measured at 1.54 μ m for samples annealed at different temperatures. Annealing was performed in vacuum for 1 h. The lines are a guide for the eye. (From Ref. 15.)

with $[Er_{act}]$ the optically active Er concentration, τ the measured luminescence lifetime, and τ_{rad} the radiative lifetime (the lifetime in the absence of nonradiative processes). The data in Fig. 7 show an intensity increase up to 900 °C concomitant with the lifetime increase, indicating that the intensity increase is mainly due to an increase in the luminescence quantum efficiency, and not due to an increase in the active Er concentration.

The rapid decrease in PL intensity above 1000 °C in Fig. 7(b) is explained by precipitation of Er, as can be seen in the transmission electron microscopy (TEM) micrograph of Fig. 8. This micrograph was taken on a sample annealed at

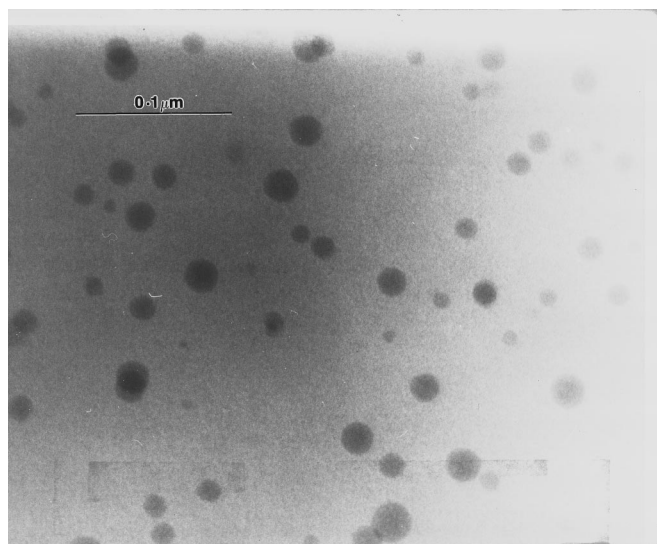


FIG. 8. Cross sectional TEM micrograph of an Er-implanted (5×10^{15} Er/cm², 3.5 MeV, 0.1 at. % peak) thermally grown SiO₂ film annealed at 1200 °C for 1 h. The micrograph is taken at the peak of the Er profile at 1.25 μ m depth. (From Ref. 15.)

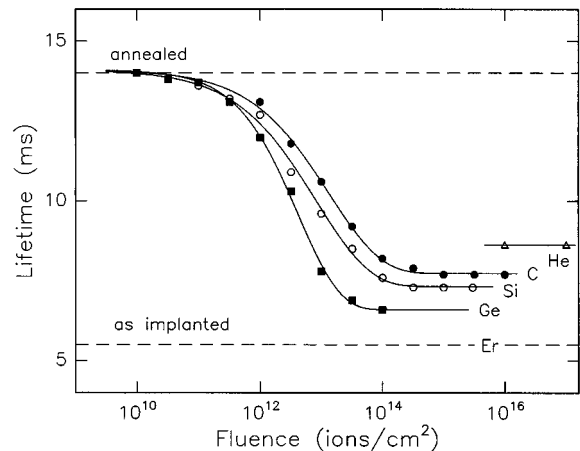


FIG. 9. PL decay times at 1.54 μ m of Er-implanted (5×10^{15} Er/cm², 3.5 MeV, 0.1 at. % peak, annealed at 900 °C) thermal SiO₂ films after irradiation with 1 MeV He (triangles), 3.5 MeV C (closed circles), 5.5 MeV Si (open circles), or 8.5 MeV Ge (squares) ions as a function of the fluence. The lifetimes for films after Er implantation (as implanted) and after annealing are indicated by dashed lines. The solid lines are guides for the eye. (From Ref. 21.)

1200 °C for 1 h and shows the area around the peak of the implant at a 1.25 μ m depth. Clearly, 10–20-nm-diam precipitates can be observed. Energy-dispersive x-ray analysis revealed that these precipitates contain Er. They were not observed for a sample annealed at 1050 °C. It is likely that these precipitates do not exhibit optical transitions, i.e., do not contribute to $[Er_{act}]$ in Eq. (1). The precipitation phenomena are then not reflected in the lifetime data [Fig. 7(b)] as these are only a probe of the optically active ions dispersed in the silica network.

2. Er³⁺ as a probe for ion irradiation damage

As the Er³⁺ luminescence is sensitive to irradiation damage in the glass (see Sec. III A1), the luminescence lifetime can also be used as a probe of such defects.²¹ Er-implanted SiO₂ films (5×10^{15} Er/cm², 3.5 MeV) were first annealed at 900 °C to increase the Er³⁺ PL lifetime to 14.1 ms (see Fig. 6). Radiation damage was then introduced into the annealed films using 1 MeV He, 3.5 MeV C, 5.5 MeV Si, or 8.5 MeV Ge ions. The ion ranges for these implants were well beyond the Er depth profile so no chemical interaction between the Er and the implanted species took place. Figure 9 shows lifetime measurements taken after irradiation by each of these ions for fluences in the range 10^{10} – 10^{16} cm⁻². In all cases, the lifetime is decreased by irradiation with fluences as low as 10^{11} ions/cm² and continues to decrease with fluence until saturation occurs above $\sim 10^{14}$ ions/cm².

From the C, Si, and Ge data in Fig. 9 the threshold fluences ϕ_t have been estimated and are defined as the fluence necessary to reduce the lifetime to a value halfway between the initial and final values. The fluence ϕ_t is listed in Table I for the three irradiation conditions and ranges from 3.0×10^{12} to 7.8×10^{12} ions/cm². To quantify these numbers, the energy loss profiles for C, Si, and Ge in SiO₂ were calculated using TRIM89¹³ and convoluted with the Er concentration profile measured with RBS. In this way the average

TABLE I. Threshold fluences (ϕ_t) determined from the curves in Fig. 9, together with the calculated average nuclear (γ_n) and electronic (γ_e) energy deposition rates. The saturation lifetime for high fluence irradiation (τ_{sat}) is also listed.

Ion	ϕ_t (10^{12} cm^{-2})	γ_n	γ_e	τ_{sat}
3.5 MeV C	7.8	1.6	1330	7.7
5.5 MeV Si	4.5	12	2140	7.3
8.5 MeV Ge	3.0	45	2100	6.6

lattice vacancy formation rate due to nuclear displacements (γ_n) and the average ionization rate due to electronic energy loss (γ_e) around the Er ions were calculated. These results are also listed in Table I.

For a given implantation fluence, γ_n varies by a factor of 28 for the three different ions whereas γ_e varies by only a factor of 1.6. Given the fact that ϕ_t varies only by a factor of ~ 2.6 , it is concluded that electronic interactions play a dominant role in determining the lifetime changes after ion irradiation. For each ion (C, Si, or Ge) the electronic energy deposition density at which the threshold fluence is reached can be estimated, i.e., $\gamma_e \phi_t$. Using the parameters in Table I, values in the range $(0.6-1.0) \times 10^{23} \text{ eV/cm}^3$, i.e., $\sim 0.9-1.5 \text{ eV/atom}$ are found. This number is in good agreement with the energy density at which radiation induced compaction²² as well as the density of E centers²³ saturate after irradiation of SiO_2 .

Figure 9 clearly shows the difference in saturation damage for the four different irradiation conditions as reflected in the saturation lifetime τ_{sat} . The fact that the high-energy heavy ions create “heavier” damage than the lower-energy lighter ions may be explained by differences in the collision cascade density, differences in damage interaction with precursor damage in the silica,^{24,25} or differences in the interaction of damage produced by electronic and nuclear stopping.^{22,26} These results are corroborated by work by Chengru *et al.*,²³ who have shown that the maximum E' defect density increases with increasing ion mass and energy. It is important to realize that the irradiation fluence for 1 MeV He that causes a significant decrease in the lifetime is a typical fluence required for taking a RBS spectrum using a 1 MeV He beam. This implies that the optical properties of these Er-doped materials are severely affected by RBS analysis. The observation that the luminescence lifetime can be “tuned” to the desired value using ion irradiation may be of use if electroluminescence devices based on Er-doped silica are fabricated.

These radiation damage studies are important in several technological fields. SiO_2 dielectric layers are routinely used in the fabrication of microelectronic devices, and their threshold voltage and leakage behavior can be influenced by irradiation. Silica-based containers are used in nuclear waste container technology because of the known mechanical resistance of these glasses to irradiation.²⁷ Furthermore, silica-based optical fibers are the standard in telecommunication technology, and radiation defects can give rise to significant transmission losses in the fibers.²⁸⁻³⁰

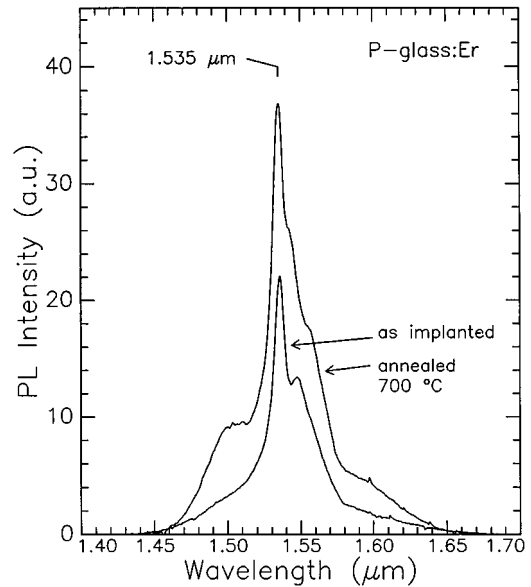


FIG. 10. Room-temperature PL spectra for as-implanted ($3.8 \times 10^{15} \text{ Er/cm}^2$, 2.9 MeV, 0.1 at. % peak) and annealed (700 °C, 1 h) phosphosilicate glass films. ($\lambda_{\text{pump}} = 488 \text{ nm}$, power = 250 mW, resolution = 1 nm) From Ref. 15.

B. Phosphosilicate glass

Phosphosilicate glass is a well-known waveguide core material as its refractive index is several percent higher than that of a pure silica cladding. These layers can be deposited by low-pressure chemical vapor deposition from silane, oxygen, and phosphine.³¹ Layers doped with 7 at. % P were used in these experiments.¹⁵ They were implanted with $3.8 \times 10^{15} \text{ 2.9 MeV Er/cm}^2$.

Room temperature PL spectra are shown in Fig. 10 for an as-implanted sample and for a sample annealed at 700 °C for 1 h. As can be seen, annealing leads to a 40% increase in peak intensity at 1.54 μm as well as a change in spectral shape. The latter indicates a change in the local environment around Er upon annealing. The FWHM spectral width of these spectra for phosphosilicate glass is typically 25 nm.

The annealing temperature dependence of the 1.54 μm integrated PL intensity and lifetime is plotted in Fig. 11. Only a very weak dependence is seen for the intensity, and the lifetime remains constant at 12 ms for all samples. This behavior is quite different from that of pure silica (Sec. III A), in which annealing was required to optimize both the intensity and the lifetime. This indicates that the implantation-induced defects in the phosphosilicate glass network structure are annealed out during implantation or they do not couple to the Er^{3+} ions.

C. Soda-lime silicate glass

Soda-lime silicate glass is a multicomponent glass containing approximately 70 mol % SiO_2 , 14 mol % Na_2O , 6 mol % Ca_2O , and small quantities of other constituents. Optical waveguides can be made in this glass using a relatively simple $\text{Na}^+ \leftrightarrow \text{K}^+$ ion exchange process.³² By immersing the glass in a KNO_3 solution at 375 °C, Na^+ ions from a surface layer are replaced by K^+ , resulting in a typically 1%

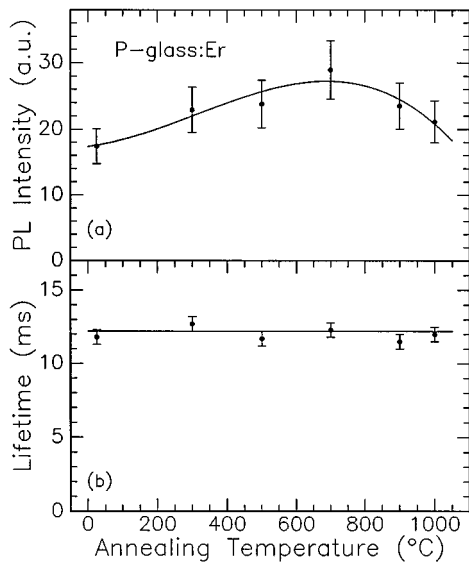


FIG. 11. (a) Room-temperature integrated PL intensity and (b) PL lifetime, both measured at $1.54 \mu\text{m}$, for Er-implanted ($3.8 \times 10^{15} \text{ Er/cm}^2$, 2.9 MeV, 0.1 at. % peak) phosphosilicate glass samples annealed at different temperatures for 1 h. The solid lines are guides for the eye. (From Ref. 15.)

increase in refractive index. Depending on the ion exchange time, diffusion depths as large as $10 \mu\text{m}$ can be achieved, enough to produce a waveguide with a well-confined mode at a wavelength of $1.5 \mu\text{m}$. All Er implants described hereafter were performed on 1-mm-thick commercially available soda-lime silicate glass (Fisher premium) samples that were coated with a 40 nm Al film to prevent charging during implantation. The Al film may also prevent outdiffusion of Na, which has been observed to occur during ion implantation in some cases.¹⁹

Soda-lime glass was implanted at room temperature with 500 keV Er ions.^{33,34} Figure 12 shows a room temperature PL spectrum of a sample implanted with a fluence of $3.7 \times 10^{15} \text{ Er/cm}^2$ (Er peak concentration 0.4 at. %), annealed at 512°C . The spectrum peaks at $1.537 \mu\text{m}$ with a FWHM of

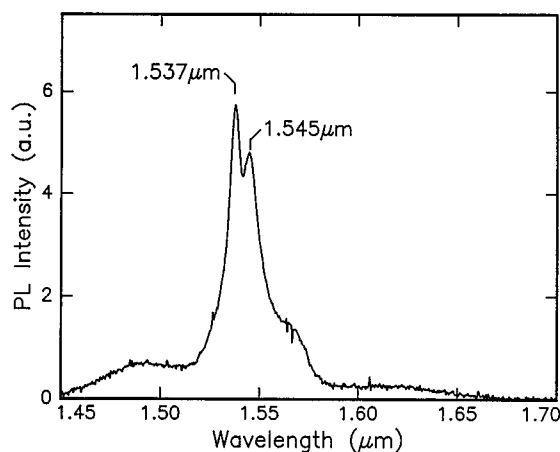


FIG. 12. Room-temperature PL spectrum of Er-implanted soda-lime silicate glass ($3.7 \times 10^{15} \text{ Er/cm}^2$, 500 keV, 0.4 at. % peak) after thermal annealing at 512°C . ($\lambda_{\text{pump}} = 514.5 \text{ nm}$, power = 70 mW, resolution = 2.3 nm). From Ref. 33.

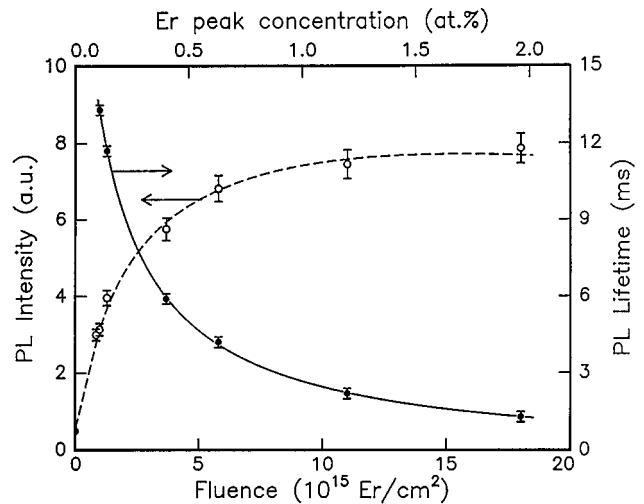


FIG. 13. PL peak intensity (open data points, left axis) and lifetime (solid data points, right axis) at $\lambda = 1.54 \mu\text{m}$ of Er-implanted (500 keV) soda-lime glass as a function of Er fluence. All samples were annealed at 512°C . The Er peak concentration is indicated on the top axis. The solid line is a guide for the eye; the dotted line is calculated using Eq. (1). (From Ref. 33.)

19 nm . The spectrum is broader than that of Er-implanted pure silica (Sec. III A), which is characteristic for a multi-component glass. An advantage of a large spectral width is that optical amplification is possible over a large bandwidth.

Annealing is necessary to optimize the Er^{3+} PL intensity in soda-lime glass. For this particular glass, the transformation temperature lies around 650°C , and the best intensities are observed for annealing just below this temperature. Note that in Sec. III A it was found that pure silica, which has a transformation temperature of around 1100°C , shows an optimum anneal temperature of 900°C . Hence we conclude that in general the transformation temperature is a characteristic annealing temperature for the activation of Er in these silica glasses.

Figure 13 shows the PL peak intensity as well as luminescence lifetime as a function of Er fluence (peak concentration range 0.15–2.0 at. %). All samples were annealed at 512°C . The PL intensity levels off for higher Er concentration, and the luminescence lifetime decreases with concentration. A threefold increase in fluence, from 6×10^{15} to $1.8 \times 10^{16} \text{ Er/cm}^2$, leads to nearly the same PL intensity and a threefold decrease in lifetime from 4.0 to 1.3 ms.

These data can be fully described by Eq. (1), assuming that (a fixed fraction of) all implanted Er is optically active. Using the measured lifetime τ at each Er fluence, Eq. (1) can be fitted through the intensity data as a function of fluence (or concentration). This is shown as the solid line, which fits the data perfectly. The fact that the data can be fitted with Eq. (1) assuming a linear increase of $[\text{Er}_{\text{act}}]$ with Er fluence implies that in this soda-lime silicate glass no precipitation of Er occurs at concentrations up to 2.0 at. %. It is known that multicomponent glasses can accommodate large impurity concentrations. In principle, these high Er densities enable high optical gain but, as we will see further on, interactions between excited Er ions will reduce the gain at high concentrations.

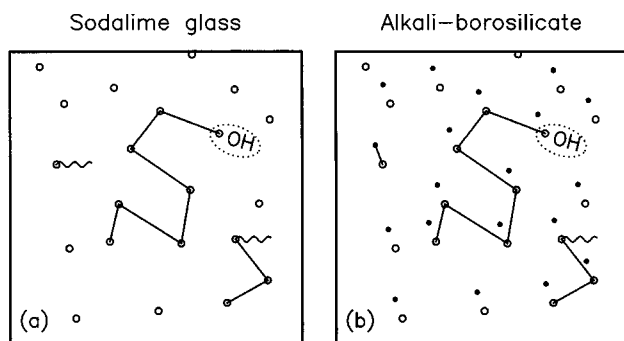


FIG. 14. Schematic of the concentration quenching processes in Er-implanted soda-lime glass (a) and borosilicate glass (b). (From Ref. 38.) The open circles indicate Er^{3+} ions. In (a), excitation migrates among Er^{3+} ions until a quenching center, such as an OH impurity, is met. In (b) Er^{3+} can also couple to nearby irradiation damage (closed circles).

To study the concentration dependence of the lifetime in more detail, the lifetime data in Fig. 13 are replotted (dots) in Fig. 15 as luminescence decay rates ($1/\tau$). A nearly linear increase with Er fluence is seen. The increase can be due to two effects: (1) an increased defect density in the glass at higher Er fluences (even though the samples were annealed at 512 °C) or (2) a concentration quenching phenomenon, also known to occur in bulk glasses.^{35–37} In the latter case, energy migrates through the material by a resonant interaction between Er ions until a quenching center is met. This is plotted schematically in Fig. 14(a). This migration will become more efficient at smaller Er–Er distances, hence higher concentrations, but will only reduce the lifetime if the material actually contains impurities or defects that couple to an Er ion.

To distinguish between these two options the following experiment was performed.³⁸ A soda-lime glass sample was first implanted with a relatively low Er fluence of $1.4 \times 10^{15} \text{ Er/cm}^2$. Subsequently, radiation damage was introduced in the Er-doped region by 1.8 MeV Au irradiation at various fluences. The Au energy is such that the projected range is well beyond the depth of the Er profile so that there is no chemical interaction between Au and Er. TRIM'89 simulations show that the Er and Au irradiations produced similar irradiation damage densities in the Er-doped region. After the combined Er and Au irradiation the samples were annealed at 512 °C.

Luminescence decay measurements were made for various Au fluences and are plotted in Fig. 15 (crosses). As can be seen, the additional radiation damage does not affect the Er decay rate (after annealing). This implies that the increase in decay rate for increased Er concentration (“Er-only” data in Fig. 15) is not due to additional radiation damage but, rather, due to a concentration quenching effect. Within a simple picture, the total decay rate as a function of Er concentration can then be written as³⁷

$$W(\text{Er}) = W_0 + 8\pi C_{\text{Er-Er}}[\text{Er}][Q], \quad (2)$$

with W_0 the decay rate in the absence of migration (presumably equal to the radiative decay rate W_{rad}), $[Q]$ the density of quenching centers, and $C_{\text{Er-Er}}$ a coupling constant. Equation (2) describes the linear behavior with Er fluence seen in

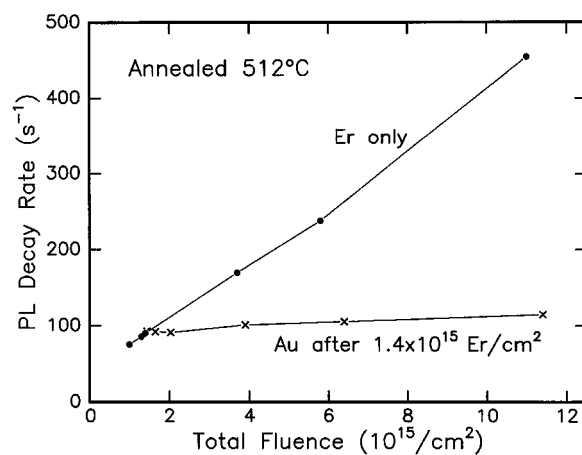


FIG. 15. Erbium PL decay rates at 1.54 μm in Er-implanted (500 keV) soda-lime glass as a function of total implanted fluence after annealing at 512 °C. Data are shown for samples implanted with Er only (closed circles replotted from Fig. 13) and for samples implanted first with $1.4 \times 10^{15} \text{ Er/cm}^2$ and then with 1.8 MeV Au to fluences ranging from 1×10^{14} to $1 \times 10^{16} \text{ Er/cm}^2$ (crosses). All samples were annealed at 512 °C after the irradiations were completed. (From Ref. 38.)

Fig. 15. Possible quenching centers in these silicate glasses are hydroxyl groups^{39,40} since the second harmonic of the OH stretch vibration is resonant with the Er 1.5 μm emission. A systematic comparison between Er-implanted silicate glasses with different OH impurity content showed a correlation between OH content and luminescence lifetime.³⁸

The OH content in soda-lime glass was measured³⁸ using infrared absorption spectroscopy: $[Q] = 8 \times 10^{18} \text{ OH/cm}^3$. Hence the coupling constant $C_{\text{Er-Er}} = 2.3 \times 10^{-39} \text{ cm}^6 \text{ s}^{-1}$ can be found. Extrapolation of the data in Fig. 15 to $[\text{Er}] = 0$ leads to an estimate of the radiative decay rate (in the absence of concentration quenching) $W_{\text{rad}} = 42 \text{ s}^{-1}$ ($\tau = 22 \text{ ms}$). This value is in agreement with an independent measurement that will be shown in Sec. III F.

The dependence of the luminescence decay rate on the Er concentration was also studied for an Er-implanted (400 keV) alkali-borosilicate glass.³⁸ The data are plotted in Fig. 16, together with the data for soda-lime glass from Fig. 15. For all concentrations a higher decay rate is found for borosilicate glass than for soda-lime glass. Above $3 \times 10^{20} \text{ Er/cm}^3$ the PL decay rate in borosilicate glass depends linearly on Er fluence. Below $3 \times 10^{20} \text{ Er/cm}^3$ the decay is a steeper function of Er density than above $3 \times 10^{20} \text{ Er/cm}^3$. The high dose data for Er-implanted borosilicate can be described using Eq. (2) and the known value for $[Q]$ ($2.6 \times 10^{19} \text{ OH/cm}^3$).³⁸ It is found that $W_0 = 718 \pm 2 \text{ s}^{-1}$ and $C_{\text{Er-Er}} = (8.6 \pm 0.5) \times 10^{-40} \text{ cm}^6/\text{s}$ (solid line in Fig. 16). This model, however, which assumes a constant number of sinks ($[Q]$) and a constant W_0 does not explain the low concentration data.

It is suggested that, for the case of borosilicate glass, ion implantation-induced defects that couple directly to the Er (i.e., not through a migration process) provide additional quenching sites for the Er. This is schematically shown in Fig. 14(b), where the black dots represent beam-induced defects. In this model the rate W_0 is equal to $W_{\text{rad}} + W_i$, with

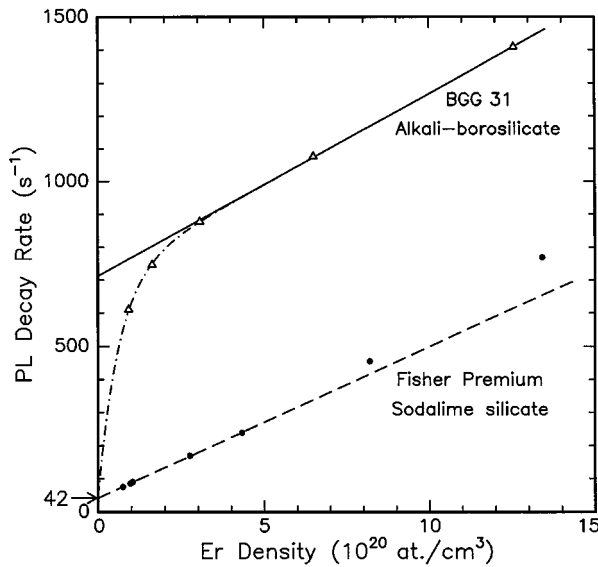


FIG. 16. PL decay rate at $1.54 \mu\text{m}$ as a function of implanted Er fluence for two different glasses: soda-lime silicate (annealed at 512°C , the same data as in Fig. 15), and borosilicate glass (annealed at 400°C). The solid and dashed lines are fits to concentration quenching models. (From Ref. 38.)

W_{rad} the purely radiative decay rate and W_i a nonradiative term due to direct coupling to the defects. A simple damage overlap model can be used to estimate the density of irradiation induced defects; it follows an exponentially saturating function of fluence φ proportional to $[1 - \exp(-\varphi/\varphi_c)]$ with φ_c a characteristic fluence.⁴¹ W_i can then be written as a function of φ as

$$W_i(\varphi) = W_{\text{sat}}[1 - \exp(-\varphi/\varphi_c)]. \quad (3)$$

Substituting $W_0 = W_{\text{rad}} + W_i$ in Eq. (2) (with the ion flux φ converted to Er peak concentration) and fitting to the data in Fig. 16 leads to the dashed line, which shows good agreement. We find $\varphi_c = (6.8 \pm 0.4) \times 10^{14} \text{ Er/cm}^2$, in agreement with a typical fluence at which the density of irradiation defects in silica glass would saturate.^{22,23}

The different behavior for borosilicate glass is attributed to the presence of boron in the network. Electron spin resonance studies have shown that B enhances the irradiation sensitivity for electronic damage in silica by orders of magnitude due to the formation of B-related point defects.⁴² Additional measurements on different types of borosilicate glasses have also shown a correlation between the quenching rate and the B content.³⁸

D. Local environment of Er

EXAFS measurements were performed⁴³ on thermally grown SiO_2 films implanted with $3.4 \times 10^{16} \text{ 2.9 MeV Er/cm}^2$ (1.0 at. % peak), and annealed at 900°C . A bulk pure silica sample, doped with Er in the melt (0.3 at. %) was also analyzed. The Fourier transforms of the EXAFS spectra are shown in Fig. 17.

Let us note here that relative differences in the distance scale between these spectra may be compared, but phase shifts have to be taken into account to convert these spectra to radial distribution functions. Detailed analyses, taking into

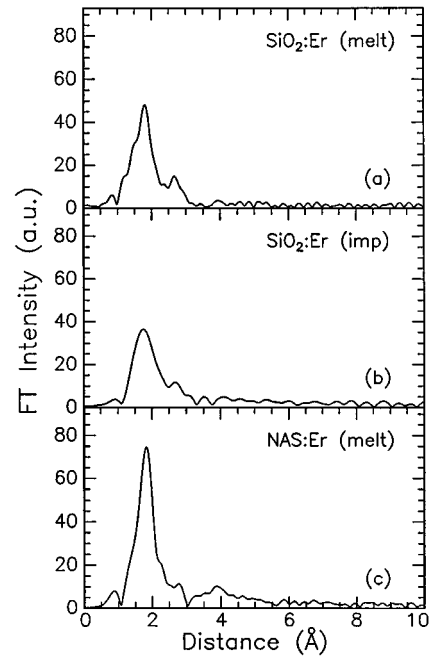


FIG. 17. Fourier transform EXAFS data for (a) pure silica doped with 0.3 at. % Er in the melt, (b) Er-implanted thermally grown SiO_2 ($3.4 \times 10^{16} \text{ Er/cm}^2$, 2.9 MeV, peak concentration 1.0 at. %, annealed at 900°C), and (c) sodium-silicate glass doped with 1.15 at. % in the melt. (From Ref. 43.)

account measurements on various Er-doped model compounds, show that in the pure silica samples Er has a nearest neighbor shell at a distance of 0.228 nm (bulk doped) or 0.225 nm (implanted), consisting of 6.0 or 5.5 O atoms, respectively. A second nearest neighbor (Si) at a distance of 0.311 nm (mean-square displacement $\Delta\sigma^2 = 2.3 \times 10^{-6} \text{ nm}^2$) is observed for the melt-doped sample. It could not be seen in the implanted sample due to the lower statistics in that measurement. The Er–O distances, $\Delta\sigma^2$, and the coordination numbers are summarized in Table II.

Measurements for sodium-silicate glass doped with Er in the melt (1.15 at. %) are also included in Fig. 17. In this material 6.3 O atoms are found at 0.226 nm from the Er, with no detectable standard deviation. These data are also included in Table II. No second nearest neighbor is observed in the EXAFS data for the sodium-silicate glass.

Several conclusions can be drawn from these data. First of all, the implanted and bulk-doped samples show very similar results. Erbium is coordinated with about 6 O atoms in a first shell. The relatively large standard deviation for the second neighbor Si distance for the bulk-doped sample indi-

TABLE II. Nearest neighbor distance ($R_{\text{Er-O}}$) with standard deviation ($\Delta\sigma^2$), and coordination number (CN) as determined from EXAFS measurements in Fig. 17.

Sample	$R_{\text{Er-O}}$	$\Delta\sigma^2$ (10^{-6} nm^2)	CN
$\text{SiO}_2\text{:Er}$ (melt)	0.228	0.8	6.0
$\text{SiO}_2\text{:Er}$	0.225	1.1	5.5
Soda-lime	0.226	0	6.3

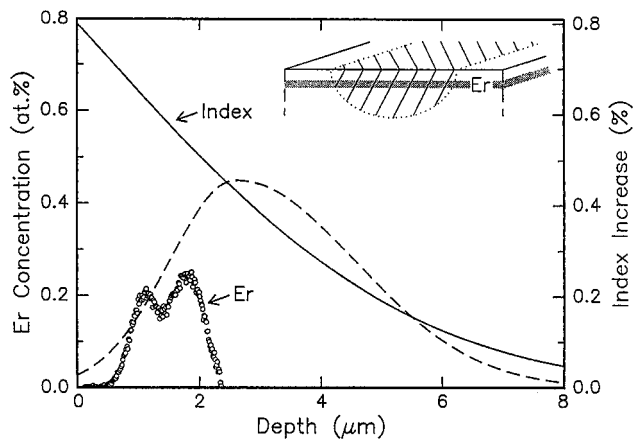


FIG. 18. Schematic of an Er-implanted soda-lime silicate glass waveguide. The Er depth profile measured by RBS is indicated by open circles, the refractive index profile by the solid line, and a calculation of the optical mode profile is shown by a dashed line. The inset shows a cross sectional view of the waveguide; the shaded area is the Er-implanted region, the hatched region enclosed by the surface, and the dotted ellipsoid indicates the ion exchanged region, i.e., the waveguide. (From Ref. 44.)

cates that the Er is not directly bonded to Si but is, instead, connected through a bridging atom, such as O. The low standard deviation (disorder) in the Er–O bonds for the soda-lime glass may be understood by the known effect of alkali ions as network modifiers. It may be that the Na^+ ions break up the Si–O network and thus allow the ErO_6 complex to relax to its lowest-energy state. This decoupling can then lead to a narrower Er–O bond length distribution than in pure silica. In this model, the Si would be decoupled from the Er, and indeed no Er–Si shell is observed. In none of the three samples did the EXAFS analysis give evidence of direct Er–Er bonds.

E. Upconversion and optical gain estimates

Erbium-doped optical waveguides were made in the following way.⁴⁴ First, soda-lime silicate glass was implanted on one side with 6×10^{15} 3 MeV Er/cm² and 1.2×10^{16} 5.0 MeV Er/cm². During implantation the sample was kept at 300 °C to avoid surface roughening.¹⁶ The sample was then annealed at 512 °C in air. Subsequently, a thin Al film was deposited and, by use of photolithographic techniques, 5-μm-wide channels were etched into the Al. Channel waveguides were then defined by $\text{Na}^+ \leftrightarrow \text{K}^+$ ion exchange. Waveguides were made in Er-implanted glass as well as in unimplanted glass for reference. The Al mask was then etched off and a transparent silicone resin cladding (refractive index $n=1.43$) was deposited. Finally, the end faces of the 3.0-cm-long waveguide were polished. Single-mode silica optical fibers were then aligned with the end faces and a fixed by an ultraviolet (UV)-hardening acrylate. The fiber-to-sample coupling loss was estimated to be 2–3 dB at 1.5 μm.

The geometry of the Er-implanted waveguide is shown schematically in Fig. 18. The open circles show the Er depth profile in the waveguide, determined using RBS. The Er peak concentration is roughly 0.2 at. % at a depth ranging from 1 to 2 μm. The solid curve shows the typical refractive

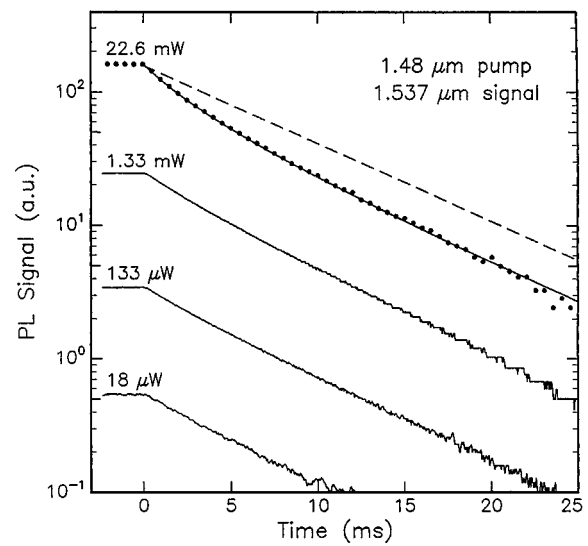


FIG. 19. PL decay curves, measured at 1.54 μm, that follow pumping to steady state using 1.48 μm excitation at 0.018, 0.133, 1.33, and 22.6 mW in an Er-implanted soda-lime glass channel waveguide (6×10^{15} Er/cm² at 3.0 MeV + 1.2×10^{16} Er/cm² at 5.0 MeV, annealed at 512 °C). The dashed line shows a single exponential decay with $\tau=7.2$ ms, and the solid line through the data for 22.6 mW is calculated using an upconversion coefficient $C_{\text{up}}=3.2 \times 10^{-18}$ cm³/s. (From Ref. 44.)

index profile after ion exchange⁴⁵ relative to the index of bulk soda-lime glass ($n=1.50$), while the dashed line indicates the 1.54 μm optical mode density. The mode peaks at a depth (2.5 μm) slightly deeper than the Er profile. The mode width is 3 μm FWHM in depth and 10 μm FWHM in the lateral dimension. The inset of Fig. 18 shows a schematic cross section of the waveguide.

PL spectroscopy measurements were performed on the waveguides by pumping with an InGaAsP diode laser operating at 1.48 μm. The pump light is absorbed high in the $^4I_{13/2}$ manifold of Er^{3+} . The energy then almost instantaneously equilibrates over the $^4I_{13/2}$ sublevels (see Fig. 1). The Er luminescence signal was collected perpendicular to the waveguide plane.

Figure 19 shows 1.54 μm luminescence decay measurements on the waveguides at four different pump powers ranging from 18 μW to 22.6 mW in the waveguide. For low pump powers the decay is single exponential with a lifetime of 7.2 ms. This corresponds to the lifetime found in Fig. 13 (Sec. III C) for a concentration of 0.2 at. %. For the highest pump power in Fig. 19 a clear nonexponential decay with a fast initial component is observed.

These data can be explained by an upconversion effect due to an interaction between excited Er^{3+} ions. This is indicated schematically in Fig. 20, which shows three possible interactions between Er ions. Figure 20(a) shows the excitation migration effect involving a single excited Er^{3+} ion, as was discussed in Sec. III C. Figure 20(b) shows a cooperative upconversion interaction between two Er^{3+} ions both excited to the first excited state, in which one is demoted back to the ground state and one is promoted to the $^4I_{9/2}$ level. Depending on whether this doubly excited ion will decay back to the first excited state or to the ground state, this upconversion interaction depletes the first excited state

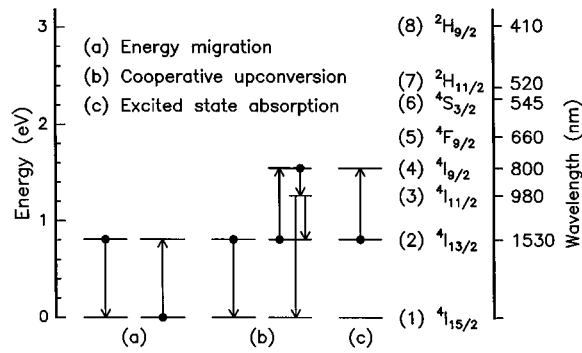


FIG. 20. Schematic of three different concentration quenching effects in Er-doped materials: (a) energy migration, (b) cooperative upconversion, (c) excited state absorption.

population by one or two ions. This upconversion interaction depends on the excited Er concentration, and will therefore lead to nonexponential decay.

Assuming that the lifetime of the $^4I_{9/2}$ level is short, the upconversion effect can be included in a two-level rate equation for the fraction n_2 of Er ions in the $^4I_{13/2}$ level:

$$\frac{dn_2}{dt} = R_{\uparrow}(1 - n_s) - R_{\downarrow}n_2 - \frac{n_2}{\tau} - [\text{Er}]C_{\text{up}}n_2^2. \quad (4)$$

Here τ is the spontaneous decay time resulting from radiative and nonradiative decay without upconversion, R_{\uparrow} and R_{\downarrow} are the rates of absorption and stimulated emission of the pump light, and C_{up} is the cooperative upconversion coefficient. Upconversion is described by a quadratic term since it involves two excited ions. $R_{\uparrow} = I_p \sigma_a / h\nu_p$ and $R_{\downarrow} = I_p \sigma_e / h\nu_p$, with σ_a and σ_e , respectively, the absorption and emission cross sections (which are known),^{35,46} $h\nu_p$ the pump photon energy, and I_p the pump intensity, which can be estimated from the total power using the known mode profile.⁴⁵ Note that the stimulated emission term $R_{\downarrow}n_2$ has to be included in Eq. (4) because the pump laser spectrum may partly overlap with the $^4I_{13/2} \rightarrow ^4I_{15/2}$ emission spectrum of Er^{3+} . Note that in all calculations excited state absorption, which brings an excited Er^{3+} ion to the $^4I_{9/2}$ level by the absorption of a second pump photon [see Fig. 20(c)], is neglected.

TABLE IV. Measured upconversion coefficients ($^4I_{13/2} + ^4I_{13/2} \rightarrow ^4I_{9/2} + ^4I_{15/2}$ transition) for various hosts.

Material	C_{up} ($10^{-18} \text{ cm}^3/\text{s}$)	Reference
Soda-lime silicate glass (implanted)	3	44
Soda-lime silicate glass (sputtered)	3	48
Phosphosilicate glass	90	48
Ge/A/P-doped fused silica fiber	3	49
Barium-silicate glass	2	50
Aluminophosphosilicate glass	10	50
Polycrystalline $\gamma\text{-Al}_2\text{O}_3$	4	65
$\text{Y}_3\text{Al}_5\text{O}_{12}$ (YAG)	54	67
Polycrystalline Y_2O_3	0.5	14
LiNbO_3	<0.14	96

This is justified by the fact that the lifetime of the $^4I_{9/2}$ level is short. Table III lists the various parameters in these equations for the case of soda-lime silicate glass, as determined above, or taken from the literature.^{46,47}

Using the data in Fig. 19 and the numbers listed in Table III, Eq. (4) can be fitted, and C_{up} determined to be $3 \times 10^{-18} \text{ cm}^3/\text{s}$. This is an important number as it enters in all the rate equations for optical gain calculations. The upconversion coefficient is listed in Table IV, together with coefficients measured on other materials. The value for soda-lime glass is similar to that found for Er in sputter-deposited glasses ($3 \times 10^{-18} \text{ cm}^3/\text{s}$),⁴⁸ indicating that the local environment and distribution of Er are similar in implanted and sputtered materials. In contrast, Er-implanted phosphosilicate glass shows $C_{\text{up}} = 9 \times 10^{-17} \text{ cm}^3/\text{s}$, 30 times higher than that for soda-lime glass.⁴⁸ A similarly high upconversion coefficient was reported for Er-doped fused silica codoped with Ge, Al, and P, a glass typically used for fiber amplifiers ($C_{\text{up}} = 10^{-16} \text{ cm}^3/\text{s}$).⁴⁹ The calculated upconversion coefficient for Er-doped bariumsilicate and aluminophosphosilicate glasses is $C_{\text{up}} = 2 - 10 \times 10^{-18} \text{ cm}^3/\text{s}$.⁵⁰

The difference in C_{up} for the different glasses may be explained by a difference in overlap between the $^4I_{13/2} \rightarrow ^4I_{15/2}$ emission and $^4I_{13/2} \rightarrow ^4I_{9/2}$ absorption spectra. The phosphosilicate glasses, which all show high upconver-

TABLE III. Parameters used in the upconversion and optical gain calculations in soda-lime glass.

Parameter	Symbol	Value	Reference
Pump wavelength	λ_p	1.48 $\mu\text{m}/980 \text{ nm}$	
Signal wavelength	λ_s	1.536 μm	
Pump absorption cross section	σ_p^a	$1.0 \times 10^{-21} \text{ cm}^2 / 1.0 \times 10^{-21} \text{ cm}^2$	46
Pump emission cross section	σ_p^e	$0.5 \times 10^{-21} \text{ cm}^2 / 0$	46
Signal absorption cross section	σ_s^a	$4.1 \times 10^{-21} \text{ cm}^2$	46
Signal emission cross section	σ_s^e	$5.0 \times 10^{-21} \text{ cm}^2$	46
Density of soda-lime glass	ρ_{SLS}	$0.67 \times 10^{23} \text{ at./cm}^3$	
OH concentration	$[\text{OH}]$	$8 \times 10^{18} \text{ OH/cm}^3$	
Concentration of implanted Er	$[\text{Er}]$	$1.4 \times 10^{20} \text{ Er/cm}^3$	
Er^{3+} first excited state lifetime	τ	$(42 \text{ s}^{-1} + [\text{Er}][\text{OH}] \times 5.8 \times 10^{-38} \text{ cm}^6 \text{ s}^{-1})^{-1}$	This work, Sec. III C
Cooperative upconversion coefficient	C_{up}	$3 \times 10^{-18} \text{ cm}^3/\text{s}$	
Waveguide amplifier length		3.0 cm	
Waveguide loss	α	1.0 dB/cm	
Optical mode size		$6 \times 10 \mu\text{m}^2$	

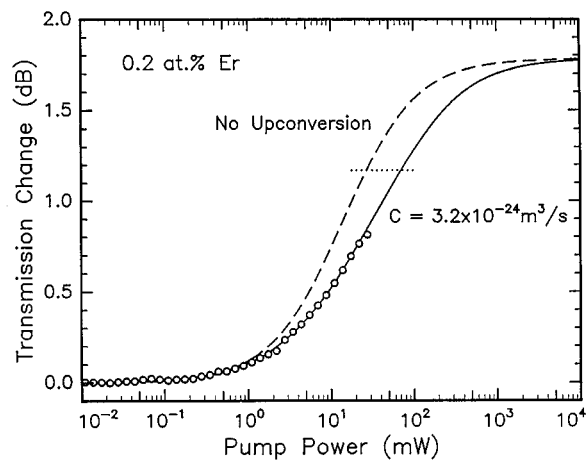


FIG. 21. Transmission change of a $1.536\ \mu\text{m}$ signal measured as a function of $1.48\ \mu\text{m}$ pump power in the soda-lime glass waveguide (open circles). The solid line is a calculation using the measured upconversion coefficient. The dotted line indicates the point at which the signal absorption rate equals the stimulated emission rate. The dashed line shows a calculation without upconversion. (From Ref. 44.)

sion coefficients, show a higher spectral overlap. In addition, it was found that in some phosphosilicate glasses Er clustering occurs;⁴⁸ this will lead to efficient upconversion. Our data in Sec. III C have shown that such clustering does not occur in Er-implanted soda-lime glass.

Figure 21 shows the transmission change of a $1.536\ \mu\text{m}$ signal, measured as a function of $1.48\ \mu\text{m}$ pump power in the Er-implanted waveguide (Er peak concentration 0.2 at. %). Without pumping, the absorption by the Er leads to a loss of 1.2 dB. For pump powers above 1 mW, the transmission increases, and a signal change of 0.8 dB is found at the maximum available pump power of 28 mW. The calculated level at which the absorption and stimulated emission are equal is indicated by the dashed line in Fig. 21. It shows that no net gain is achieved in this case. The line drawn through the data is a calculation based on rate equations including upconversion; the dashed line assumes $C_{\text{up}}=0$. In comparing the two calculations, it can be seen that upconversion shifts the 0 dB power point by a factor of 3, thereby increasing the pump power necessary for net gain to 70 mW.

Several improvements in waveguide design are possible. First of all, the total achievable gain could be increased by extending Er doping to a greater depth (keeping the peak concentration the same). Gain calculations were performed for this case⁵¹ using an optical propagation model described in Ref. 52, and using the input parameters listed in Table III. The result is shown in Fig. 22. A small net gain can be achieved at rather high pump powers ($>300\ \text{mW}$ at $1.48\ \mu\text{m}$).

An improvement in the gain could be achieved by using a $980\ \text{nm}$ pump that is resonant with the second excited state ($^4I_{9/2}$ level). This avoids the problem of pump stimulated emission which effectively lowers the maximum achievable inversion. A gain calculation for this case is also shown in Fig. 22. The gain threshold is roughly 100 mW, and a moderate gain of 3.0 dB (1.0 dB/cm) is possible at a pump power of 200 mW.

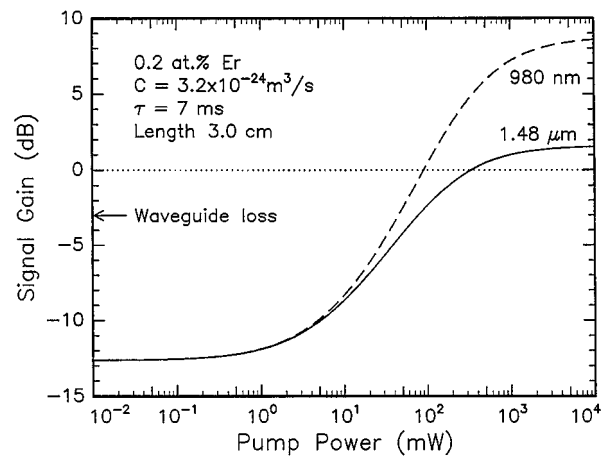


FIG. 22. The calculated net gain at $1.536\ \mu\text{m}$ as a function of pump power in a 3-cm-long soda-lime glass waveguide with the Er depth profile spread all through the waveguide depth at a concentration of 0.2 at. %. The intrinsic waveguide loss (no Er) of 1.0 dB/cm is indicated by an arrow. Results are shown for two pump wavelengths: $980\ \text{nm}$ and $1.48\ \mu\text{m}$. (From Ref. 51.)

The pump powers required to achieve net optical gain are still relatively high and are attributed to three effects.

- (1) The Er luminescence lifetime is relatively low due to concentration quenching effects (migration to OH impurities),
- (2) Cooperative upconversion increases the effective decay rate when high densities of Er are excited.
- (3) The waveguide mode profile is relatively wide ($3 \times 10\ \mu\text{m}$) due to the small index contrast between core and cladding, resulting in low pump intensities.

An improvement in the gain performance could be achieved by lowering the OH quenching impurity density. However, calculations⁵¹ have shown that the main limiting factor at high pump powers is upconversion. It is therefore important to engineer the glass composition to obtain an upconversion coefficient that is as low as possible. Such glasses should have narrow and nonresonant emission and absorption cross section spectra for the $^4I_{13/2} \rightarrow ^4I_{15/2}$ and $^4I_{13/2} \rightarrow ^4I_{9/2}$ transitions, respectively. Since the mismatch between these spectra can be accommodated by the annihilation or generation of phonons, glasses with low-energy phonon spectra are desirable.

The effect of upconversion can also be reduced by lowering the Er concentration. This is illustrated in Fig. 23, in which three gain calculations are shown for Er concentrations of 0.06, 0.2, and 1.0 at. %. A waveguide loss of 1 dB/cm is assumed.

All other parameters were kept fixed, except for the $1.54\ \mu\text{m}$ PL decay rate, which depends on the Er density [Er] due to the concentration quenching as shown in Fig. 13 and Eq. (2). In Fig. 23 it can be seen that the maximum achievable gain increases for the increasing Er concentration that is expected if enough pump power is available to excite all the Er. The gain threshold, however, shows more complicated behavior as a function of Er density. For a very low Er concentration (0.06 at. %) the gain threshold is high (300 mW) because almost all Er must be inverted in order to produce

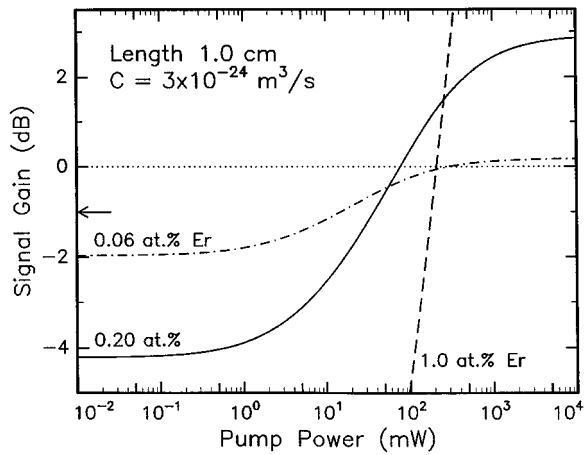


FIG. 23. Calculations of the net optical gain in a soda-lime silicate glass channel waveguide for a $1.536 \mu\text{m}$ signal as a function of 980 nm pump power. Results are shown for three Er concentrations: 0.06, 0.20, and 1.0 at. % Er. The arrow indicates the intrinsic waveguide loss. (From Ref. 44.)

sufficient gain to overcome the waveguide loss of 1.0 dB/cm. When the Er concentration is increased to about 0.2 at. %, the net gain may be reached for a lower degree of inversion, resulting in a lower gain threshold (76 mW). At even higher Er concentration (1.0 at. %) the luminescence lifetime τ strongly decreases due to concentration quenching and cooperative upconversion. Therefore more pump power is required to reach inversion, and the threshold increases to 215 mW.

We can conclude that the gain performance of these silica-based waveguides is limited by deexcitation of Er due to cooperative upconversion if the Er concentration exceeds roughly 0.1 at. % ($7 \times 10^{19} \text{ Er/cm}^3$). A reduction in the up-conversion coefficient, for instance, by choosing a different host for the Er, can lead to a large reduction of the pump threshold for net gain. Further improvements may be possible by reducing the waveguide propagation loss as well as by reducing the optical mode dimensions. Taking all these things into consideration, the choice of the optimum Er concentration is primarily determined by the amount of pump intensity that is available for a particular waveguide geometry.

F. Spontaneous emission near a dielectric interface

An important consequence of using ion implantation for optical doping is that the optically active ions are always placed near the surface. As will be shown now, the presence of a dielectric interface can have a pronounced effect on the spontaneous emission rate of Er.⁵³

A soda-lime silicate glass sample (refractive index $n = 1.50$) was covered with a 120-nm-thick Al film and then implanted with 500 keV Er ions. After implantation, the Al layer was etched off, and the sample was annealed at 512°C . The Er depth profile, measured using RBS, showed an Er surface concentration of 0.25 at. % that gradually decreased to 0 at. % at a depth of roughly 200 nm.

Luminescence lifetime measurements at $1.537 \mu\text{m}$ were performed on the sample and are shown in Fig. 24. The inset

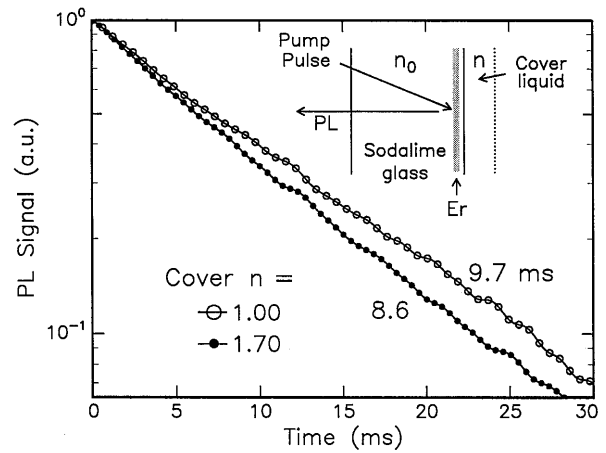


FIG. 24. PL decay traces of the $1.537 \mu\text{m}$ emission from an Er-implanted (peak concentration 0.25 at. %) soda-lime silicate glass sample. The open circles were measured with the sample in air, and the closed circles are with a methylene-iodide film ($n = 1.70$) covering the surface. The inset shows the measurement geometry. (From Ref. 53.)

shows the measurement geometry. With the sample kept in air, a decay time of 9.7 ms was measured. When the surface is covered with a methylene-iodide ($n = 1.70$) film, the lifetime reduces to 8.6 ms. When the methylene-iodide film is blown off the surface, the lifetime returns to 9.7 ms.

Additional measurements were performed using other transparent liquids with refractive indices in the range $n = 1.3$ – 1.7 . PL decay rates for these samples are plotted in Fig. 25. The decay rate shows a clear increase with increasing refractive index. These data are one of the simplest demonstrations of Fermi's golden rule, which states that the spontaneous emission rate is proportional to the final density of states (DOS). In the case of Er luminescence, the final DOS is composed of an electronic part (the Er^{3+} ground

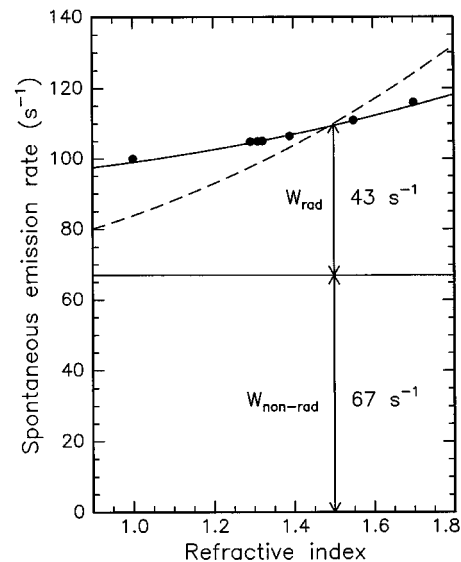


FIG. 25. Measured PL decay rates at $1.537 \mu\text{m}$ as a function of refractive index of the covering liquid (closed circles). The index of soda-lime glass is 1.50. (From Ref. 53.) The dashed line is a calculation assuming pure radiative decay, and the solid line assumes both radiative and nonradiative components in the decay.

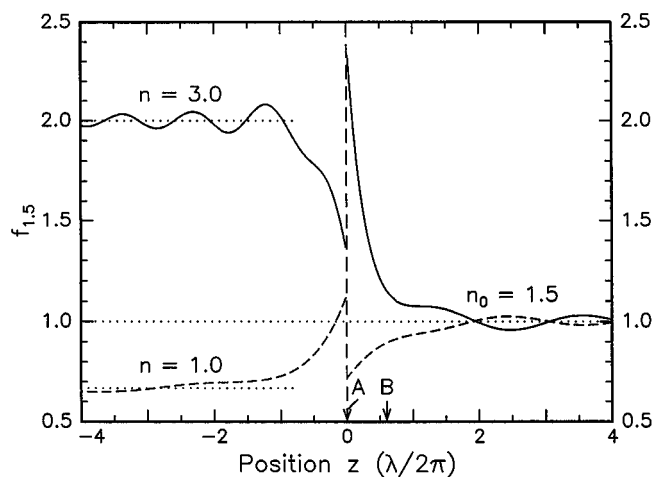


FIG. 26. The local classical density of optical states on both sides of an interface between two dielectric media. The refractive index on the right-hand side is $n = 1.50$. Calculations are shown for $n = 1.00$ and $n = 3.00$ on the left-hand side. Data are normalized to the density of states for a medium with $n = 1.50$. (From Ref. 53.)

state) and a photon field. The latter is influenced by the presence of a dielectric layer on the surface, near the Er.

In order to make a quantitative estimate of the effect of the index on the Er PL decay rate, one can define a local DOS by coherently summing a complete set of plane waves coming in and reflecting and refracting at the interface. The result of such a calculation, using an isotropic combination of polarizations, is given in Fig. 26. The DOS ($f_{1.5}$) is plotted relative to the DOS in an infinite medium with index $n = 1.50$. The distance from the glass surface is given in units of $\lambda/2\pi$, where λ is the wavelength in vacuum.

As can be seen, the DOS is discontinuous at the interface. This discontinuity is caused by the polarization component parallel to the interface. The oscillations on either side of the interface have a periodicity of $\lambda/2n$ and are due to interference between incoming and reflecting waves. For large distances from the interface the DOS is proportional to n .

The normalized DOS in Fig. 26 determines the radiative decay rate for Er, at a distance z from the interface when a liquid with index n covers the glass, relative to the rate in bulk soda-lime glass. The distance z can be integrated out by weight averaging it over the known Er depth profile.⁶³ In addition to radiative decay, Er may also show nonradiative decay, which is not sensitive to changes in the optical DOS as it does not involve a photon field. The total PL decay rate can then be written as

$$W_{\text{tot}}(n) = W_{\text{nr}} + f_{1.5}(n)W_r, \quad (5)$$

where W_{nr} is the nonradiative decay rate and W_r the radiative decay rate in the absence of an interface ($n = 1.50$). The dashed line in Fig. 25 shows the result of a calculation of W_{tot} assuming $W_{\text{nr}} = 0$ and $W_r = 110 \text{ s}^{-1}$. As can be seen, the measured decay rate shows a much weaker dependence on n than the calculation. Therefore a nonradiative component has to be introduced: The solid line is obtained using $W_r = 45 \text{ s}^{-1}$ and $W_{\text{rad}} = 65 \text{ s}^{-1}$, and fits the data very well.

From these rates the PL quantum efficiency, defined as W_r/W_{tot} , can be determined;⁵³ it amounts to 45%. These data provide the first experimental determination of the luminescence quantum efficiency of Er^{3+} luminescence in silica glass, a parameter of great interest in all optical gain calculations and optical amplifier design routines. Note that the purely radiative rate of $W_r = 45 \text{ s}^{-1}$ ($\tau = 22 \text{ ms}$) corresponds nearly exactly to the value derived by extrapolating the concentration dependence of the Er decay rate to zero concentration, as shown in Fig. 15. From this we conclude that the optimum lifetime achievable for Er in soda-lime glass is 22 ms and that concentration quenching effects due to energy migration and coupling to quenching sites reduce the lifetime to a lower value, depending on the Er concentration.

IV. Al_2O_3 , Y_2O_3

A. Optical activation

Al_2O_3 is an interesting host for Er because the waveguide fabrication technology is well developed for this material. High-quality, low-loss Al_2O_3 waveguide structures are readily made on silicon substrates using standard lithographic techniques.⁵⁴ The advantage of Al_2O_3 ($n = 1.64$) waveguide cladded with SiO_2 ($n = 1.45$) is that the high index contrast between core and cladding results in high confinement of the optical mode in the guide, leading to efficient pumping and amplification. In addition, the high index contrast allows for the use of small waveguide bending radii ($< 100 \mu\text{m}$),⁵⁵ making compact waveguide devices possible. Furthermore, the similarity in valence and crystal structure between Al_2O_3 and Er_2O_3 may allow for incorporation of high concentrations of Er in the Al_2O_3 crystal structure.

Al_2O_3 films were deposited on thermally oxidized Si(100) substrates by radio-frequency magnetron sputtering from an Al_2O_3 target. The SiO_2 thickness was $6 \mu\text{m}$, and the Al_2O_3 thickness 430 nm. The deposition was carried out at a pressure of 0.8 Pa in an oxidizing ambient of 90% Ar and 10% O_2 . The resulting structure of Al_2O_3 is a cubic polycrystalline phase. Details of the sputtering process and film properties can be found elsewhere.⁵⁴ Single-mode ridge waveguides have been realized using these films, and their optical loss can be minimized to 0.35 dB/cm by thermal annealing at 825 °C.

Figure 27 shows a RBS spectrum of an Al_2O_3 film implanted with 800 keV Er to a fluence of $2.3 \times 10^{15} \text{ Er/cm}^2$. The Er depth profile is Gaussian in shape, and peaks at a depth of 140 nm with a FWHM of 80 nm. The Er peak concentration is 0.23 at. %. A concentration of 0.4 at. % Ar is also observed throughout the alumina film due to the sputtering process. Neither the Er profile nor the Ar concentration in the film changed significantly with annealing.

The PL spectrum of the Er-implanted sample after annealing in vacuum at 950 °C is shown in Fig. 28. The spectrum peaks at $1.533 \mu\text{m}$ with a FWHM of 55 nm. This is substantially broader than for Er-implanted SiO_2 (11 nm FWHM), phosphosilicate glass (25 nm FWHM), or soda-lime silicate glass (19 nm FWHM) (see Secs. III A–III C), and offers a larger bandwidth for wavelength division mul-

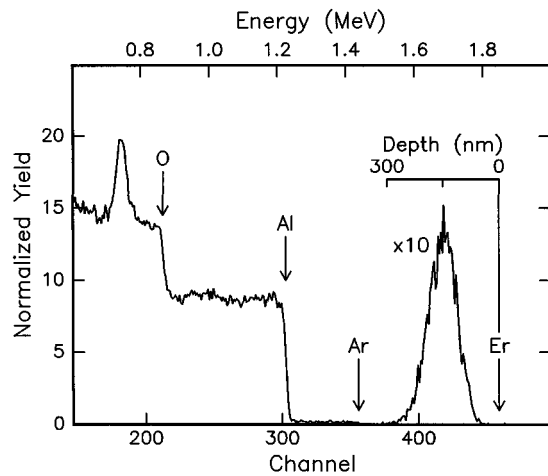


FIG. 27. Rutherford backscattering spectrum of an Er-implanted (2.3×10^{15} Er/cm², 800 keV) Al₂O₃ film on a SiO₂ buffer layer on Si. (From Ref. 60.)

tiplexed signal amplification. Spectra for samples implanted at different fluences and annealed at different temperatures have different intensities but similar shapes, with small variations in relative intensity between the different lines.

Figure 29(a) shows the PL peak intensity as a function of anneal temperature for samples with an Er peak concentration of 0.23 at. %. A gradual increase of the PL intensity is seen upon annealing to 600 °C, after which the intensity is six times higher than that for the as-implanted case. A further, and more rapid, increase with temperature is seen above 600 °C; another factor of 6 is gained after 950 °C annealing. The discontinuous behavior around 800 °C is reproducibly seen in different sample sets. The luminescence decay was also monitored, and found to be single exponential in each case. Figure 29(b) shows the $1/e$ lifetime determined from the luminescence decay as a function of anneal temperature. The lifetime increases from ~ 1 ms for the as-implanted sample to 6–7 ms for samples annealed above 700 °C.

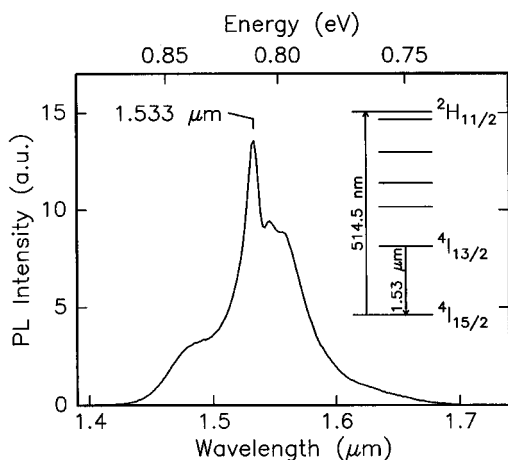


FIG. 28. PL spectrum, taken at room temperature, of an Er-implanted (2.3×10^{15} Er/cm², 800 keV, peak concentration 0.23 at. %) Al₂O₃ film annealed at 950 °C. ($\lambda_{\text{pump}} = 514.5$ nm, resolution 2 nm). From Ref. 59.

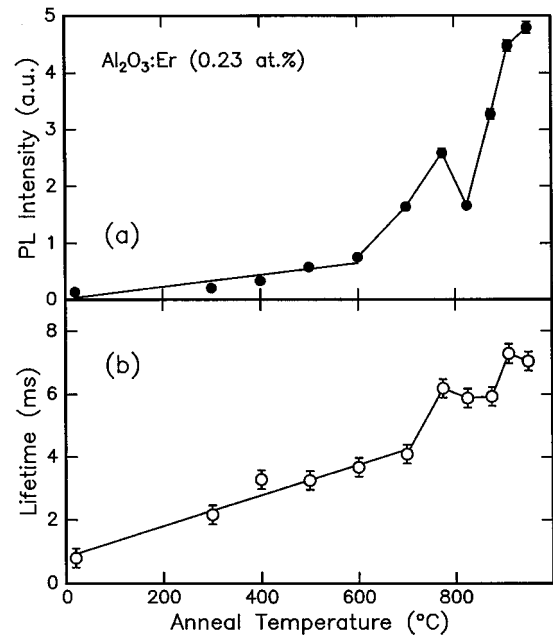


FIG. 29. PL (a) peak intensity and (b) lifetime at $\lambda = 1.533 \mu\text{m}$ measured as a function of anneal temperature for Er-implanted (2.3×10^{15} Er/cm², 800 keV, 0.23 at. % peak) Al₂O₃ films. Thermal annealing was performed for 1 h in vacuum. The solid lines are guides for the eye. (From Ref. 59.)

The observed annealing behavior may be split into two different regimes. Below ~ 700 °C, similar increases in PL intensity and lifetime are seen, indicating that the increase in intensity is predominantly caused by the increase in lifetime. The increase in lifetime is explained by a decrease in the number of nonradiative decay channels as a result of the annealing of implantation-induced defects in the Al₂O₃ crystal structure. Previous studies have indeed shown that temperatures up to ~ 700 °C are required to anneal implantation-induced damage in Al₂O₃.^{56,57} In the temperature regime above 700 °C, the increase in PL intensity is not accompanied by a strong increase in lifetime. The intensity increase is therefore attributed to an increase in the fraction of optically active Er ions. The discontinuous behavior around 825 °C coincides with the attainment of minimum optical loss in Al₂O₃ waveguides after annealing at 825 °C.^{54,58} Apparently the microstructural changes taking place around 825 °C affect the PL intensity.

Figure 30 shows the Er concentration dependence of PL intensity and lifetime after annealing at 825 °C. In these experiments uncladded Al₂O₃ films were implanted with 800 keV Er at room temperature.^{59,60} Implantation fluences ranged from 1×10^{14} to 1×10^{16} Er/cm², corresponding to peak concentrations in the range 0.01–1.0 at. %. The bottom axis in Fig. 30 shows the Er implantation fluence on a logarithmic scale; the corresponding Er peak concentration is shown on the top axis. The PL intensity (closed data points, left axis) increases by a factor of 50 as the concentration is increased from 0.01 to 1 at. %.

The lifetime (open data points, right axis) decreases slowly with increasing concentration from 8 to 4 ms. The sublinear increase in intensity is accounted for approximately by the decrease in lifetime. This becomes clear from a cal-

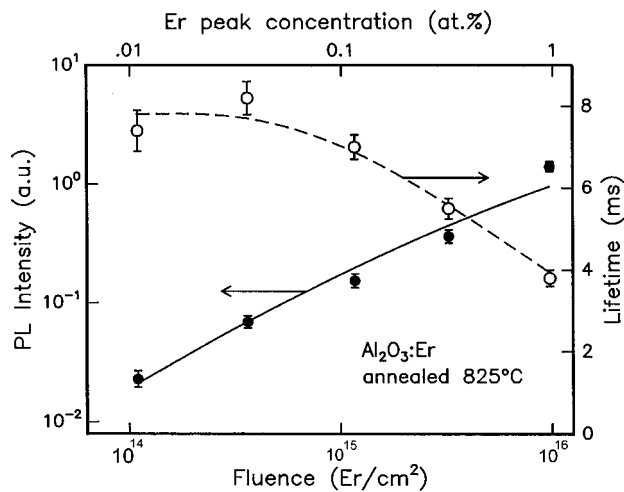


FIG. 30. PL peak intensity (left axis) and lifetime (right axis) as a function of implanted Er fluence (800 keV). The corresponding Er peak concentration is indicated on the top axis. All samples were annealed for 1 h at 825 °C in vacuum. The dashed line through the lifetime data is a guide for the eye. The solid line is calculated from the dashed line using Eq. (1). (From Ref. 59.)

ulation of the PL intensity (solid line) using the curve through the lifetime data (dashed line), assuming that the PL intensity is proportional to the active Er fluence multiplied by the lifetime [see Eq. (1) in Sec. III A1]. The reasonable agreement with the intensity data suggests that the *fraction* of active Er ions does not change with concentration.

The decrease in lifetime is explained by an increase in the number of nonradiative decay channels, which may involve implantation-induced defects or concentration quenching at high Er concentrations. It should be noted that much longer lifetimes at high Er concentration are achieved in Al₂O₃ than in, e.g., soda-lime silicate glass, which showed a decrease in lifetime from 22 ms (low concentration limit) to 1.5 ms upon increasing the Er concentration to 1.0 at. % (Sec. III C). The difference is attributed to the relatively high density of quenching centers in soda-lime glass. Apparently such quenching centers are not present in Al₂O₃. In addition, energy exchange between Er ions, which results in migration followed by luminescence quenching, is less efficient in a material with widely spread Stark levels. In fact, the PL spectra for Er-implanted Al₂O₃ are two to three times broader than those for silicate glass.

B. Absorption and emission cross sections

The performance of an Er-doped amplifier depends on the magnitude and wavelength dependence of the emission and absorption cross sections. Together with the Er concentration profile, the optical intensity profile, and the waveguide loss, knowledge of these parameters enables a first order estimate of the potential optical gain. Direct measurement of both emission and absorption cross sections is difficult; in practice it is easier to measure absorption by standard techniques, and calculate the emission cross section from the absorption results. This is referred to as McCumber theory, or the method of reciprocity.^{61,62}

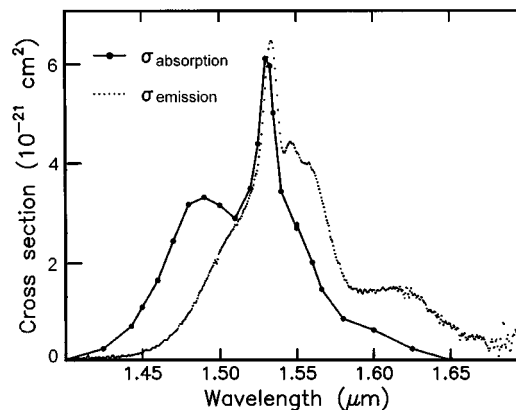


FIG. 31. Absorption and emission cross sections derived from prism coupling measurements on Er-implanted (2.5×10^{16} Er/cm², 1.35 MeV, 1.5 at. % peak) Al₂O₃ planar waveguides. (From Ref. 63.)

Prism coupling measurements can be used to determine the optical absorption of Er-implanted Al₂O₃ planar waveguides as a function of wavelength.⁶³ In these measurements, light from a tunable laser is coupled into an Er-implanted planar waveguide using a prism, travels through the waveguide film, and is coupled out through a second prism. By varying the distance between the prisms, the absorption in the waveguide can be determined. Since the optical mode profile and Er depth profile are known, the absorption cross section spectrum can be derived from such data. Results for a 0.6-μm-thick Al₂O₃ planar film implanted at 77 K with 1.35 MeV to a fluence of 2.5×10^{16} Er/cm² (peak concentration 1.5 at. %) and annealed at 825 °C are shown in Fig. 31.

The emission spectrum, measured using standard PL spectroscopy and normalized so that it matches the emission spectrum calculated using McCumber theory,⁶³ is shown also in Fig. 31. The peak cross section for absorption is found to be 5.8×10^{-21} cm² at 1.530 μm. At the commonly used 1.48 μm pump wavelength for Er-doped amplifiers, the absorption cross section is $\sigma^a = 3.0 \times 10^{-21}$ cm².

The peak emission cross section is $\sigma^e = 6.1 \times 10^{-21}$ cm², in the same range as that found in, e.g., Al₂O₃ codoped silica glass fiber (4.4×10^{-21} cm²).⁶⁴ The cross sections that we have determined here will be used to make optical gain estimates in Sec. IV C.

C. Upconversion in Al₂O₃

For determination of the optimum Er concentration in an Er-doped Al₂O₃ waveguide amplifier it is first necessary to determine the upconversion coefficient as well as the excited state absorption (ESA) cross section in Al₂O₃. In order to do such measurements, 9-mm-long Er-doped Al₂O₃ channel waveguides were made. The Al₂O₃ films were 600 nm thick and the ridges 1.5 μm wide. Details of the fabrication are described in Ref. 65. Two samples were made with Er peak concentrations of 0.12 and 1.4 at. %. The end faces of the waveguides were mechanically polished and a 1.48 μm InGaAsP laser diode pump beam was coupled into the waveguide through a tapered optical fiber that was aligned using

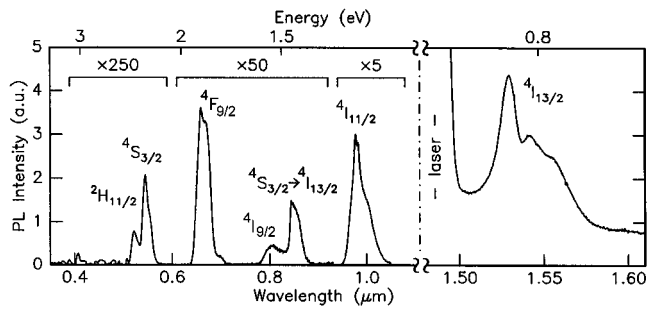


FIG. 32. PL spectrum of an Er-implanted Al_2O_3 ridge waveguide (1.4 at. % Er) pumped at $1.48 \mu\text{m}$ at a power of 2 mW in the waveguide. The transitions are indicated by their initial states (see Fig. 20 for a level diagram). All but one of the transitions terminate at the ground state; the one exception is also indicated by its final state. Note the multiplication factors ($\times 5$, $\times 25$, $\times 250$). (From Ref. 65.)

piezo actuators. Powers of up to 10 mW were coupled into the guides, resulting in pump intensities of up to $4 \times 10^5 \text{ W/cm}^2$.

Figure 32 shows the PL spectrum obtained by coupling 2 mW of $1.48 \mu\text{m}$ pump light into the Al_2O_3 waveguide (high concentration sample: 1.4 at. % Er). A spectral range of $0.35\text{--}1.6 \mu\text{m}$ was covered using a photomultiplier and a liquid nitrogen-cooled Ge detector, and the PL spectra were corrected for detector sensitivities. The luminescence peak around $1.53 \mu\text{m}$ is characteristic of Er^{3+} emission in its first excited state, and is identical to that in Fig. 28. The peak at $1.48 \mu\text{m}$ is due to scattering of the pump laser light. In addition, several other luminescence peaks can be distinguished, each characteristic of an intra- $4f$ transition in Er^{3+} , as can be seen in Fig. 32. The occurrence of these emission peaks is indicative of upconversion.

The 980 nm line can be attributed to both cooperative upconversion and ESA [see Figs. 20(b) and 20(c)]. Additional measurements⁶⁵ of the pump power dependence of the 980 nm and $1.53 \mu\text{m}$ luminescence show a quadratic relation between the 980 nm and the $1.53 \mu\text{m}$ luminescence, indicating that cooperative upconversion is the dominant effect. Similarly, it can be shown⁶⁵ that the luminescence at 520 nm ($^2H_{11/2}$) and 545 nm ($^4S_{3/2}$) is attributed to a second order cooperative upconversion interaction between Er^{3+} ions in the $^4I_{11/2}$ state (populated from the $^4I_{9/2}$ state). The luminescence at 660 nm is due to transitions from the $^4F_{9/2}$ level (populated from higher lying levels) to the ground state. The measurements indicate that in a waveguide with a high Er concentration (1.4 at. %) cooperative upconversion is the dominant upconversion process.

The low concentration sample (0.12 at. % Er) exhibits a luminescence spectrum similar to that in Fig. 32 but now the intensities of the higher order emission peaks are strongly reduced.⁶⁵ Figure 33 shows the $1.53 \mu\text{m}$ and 980 nm luminescence intensity observed in the low concentration sample as a function of pump intensity, on logarithmic scales. The luminescence intensity at each wavelength is proportional to the fraction of excited Er^{3+} ions in the corresponding energy level, and the measured data were converted to these fractions as is discussed in detail in Ref. 65.

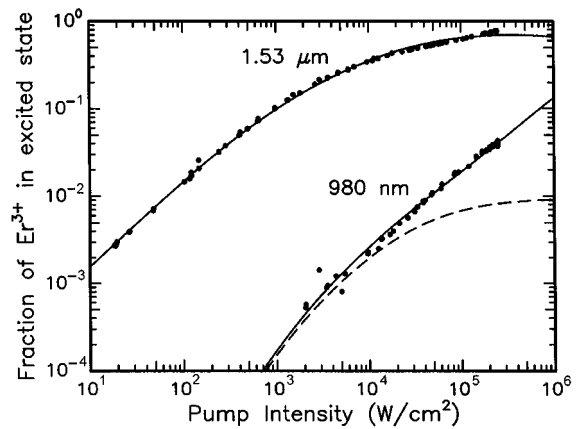


FIG. 33. Population fractions of Er^{3+} in the $^4I_{13/2}$ state ($1.53 \mu\text{m}$) and $^4I_{11/2}$ state (980 nm) vs $1.48 \mu\text{m}$ pump intensity. Data are shown on logarithmic scales for the low concentration (0.12 at. % Er) ridge waveguide (solid dots). The solid lines are fits to the data including effects of cooperative upconversion and ESA. The dashed line shows the contribution of cooperative upconversion to the 980 nm luminescence. (From Ref. 65.)

The luminescence around $1.53 \mu\text{m}$, originating from the first excited state, initially shows a linear dependence on pump intensity, i.e., a slope of 1 in Fig. 33. As higher intensities are reached, the luminescence deviates from linear behavior, and eventually saturates. This is expected because the population of Er^{3+} ions in the ground state is depleted, and less Er^{3+} is left to be excited. Above the pump intensity where the $1.53 \mu\text{m}$ emission starts to deviate from a straight line, luminescence around 980 nm ($^4I_{11/2}$) appears. Its intensity increases much more strongly with pump power than the $1.53 \mu\text{m}$ emission in this range.

The behavior shown Fig. 33 can be modeled by solving rate equations that govern the populations in each level, as is discussed in detail in Ref. 65. In these calculations both cooperative upconversion and excited state absorption were taken into account, with the upconversion coefficient and ESA cross section as free parameters. The upconversion coefficient is as defined in Eq. (4). The Er luminescence lifetime under low power conditions was 7.8 ms. The measured lifetime of the third excited state (980 nm luminescence) was $30 \mu\text{s}$ (and will be discussed further). The cross sections determined in Sec. IV B were used. Using the fit of these calculations through the data, the measured PL intensity was converted to a population scale. As can be seen, for the highest pump intensity used in the measurement, the population in the first excited state is 70%. Note that the maximum achievable degree of inversion at this pump wavelength is limited to 78% due to the stimulated emission of the pump.

At the highest pump power used in Fig. 33 nearly 5% of the Er is in the third excited state, emitting 980 nm luminescence. If this 980 nm emission were a result of cooperative upconversion only, its intensity would depend quadratically on the $1.53 \mu\text{m}$ intensity. Such behavior is indicated in Fig. 33 by the dashed line, and it clearly does not fit the data. Therefore, for this low concentration sample, both ESA and well as cooperative upconversion determine the total upconversion behavior. The upconversion coefficient determined

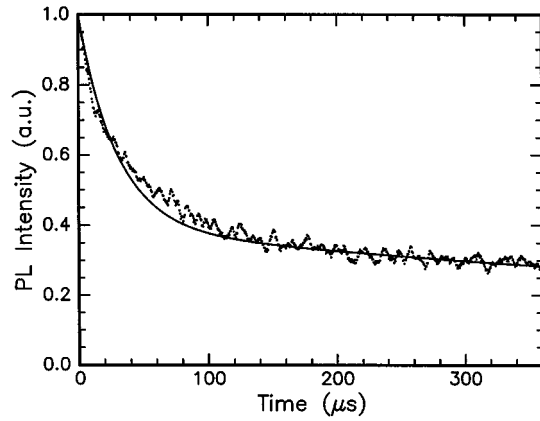


FIG. 34. Luminescence decay of the 980 nm luminescence (dots) after switching off the pump source for a pump intensity in the waveguide of 5×10^4 W/cm². Data are shown for the ridge waveguide with 0.12 at. % Er. The solid line is a fit to the data taking into account ESA (fast decaying component) and cooperative upconversion (slow decaying component). (From Ref. 65.)

from the fits in Fig. 33 was $C_{up} = (4 \pm 1) \times 10^{-18}$ cm³/s, and the ESA cross section $\sigma_{ESA} = (0.9 \pm 0.3) \times 10^{-21}$ cm².

Figure 34 shows the luminescence decay of the 980 nm emission after pumping at an intensity of 5×10^4 W/cm². Initially the decay proceeds very rapidly, then the decay rate decreases, and after 300 μ s 30% of the original population is still present. This is due to the two different mechanisms that populate the $^4I_{11/2}$ state: ESA and cooperative upconversion. At the moment the pump is switched off, ESA stops, and the Er population that was excited through ESA will decay with the lifetime of the $^4I_{11/2}$ state. Upconversion, however, continues to populate this state even after the pump is switched off due to the long lifetime (7.8 ms) of the first excited state. Therefore, a long tail can be observed in the 980 nm decay. The ratio between the intensities of the fast and slow decay components of the 980 nm light reflects the contributions of each upconversion mechanism to the population of the $^4I_{11/2}$ state: $\sim 60\%$ by ESA and $\sim 40\%$ by cooperative upconversion.

A quantitative analysis of the decay curve in Fig. 34 is obtained by solving the rate equations numerically. The result is shown as the solid line. From this fit, the lifetime of the third excited state is deduced: 30 μ s. Comparison of this number to typical radiative decay rates for Er³⁺ (several ms) indicates that the decay of the $^4I_{11/2}$ energy level is dominated by multiphonon emission rather than by radiative decay.

A detailed analysis⁶⁵ of the absorption and emission spectra of Er³⁺ shows that both the ESA and cooperative upconversion effects are not exactly resonant; they have mismatches on the order of 100–1000 cm⁻¹. These processes, therefore involve the emission of phonons at such energies, which is possible in Al₂O₃ because the highest phonon energy is 870 cm⁻¹ (0.1 eV) for transverse optical phonons.⁶⁶ As roughly one phonon is necessary to accommodate the mismatch, the probability for upconversion and ESA may still be appreciable, but considerably lower than for resonant excitation. The ESA cross section determined above is nearly

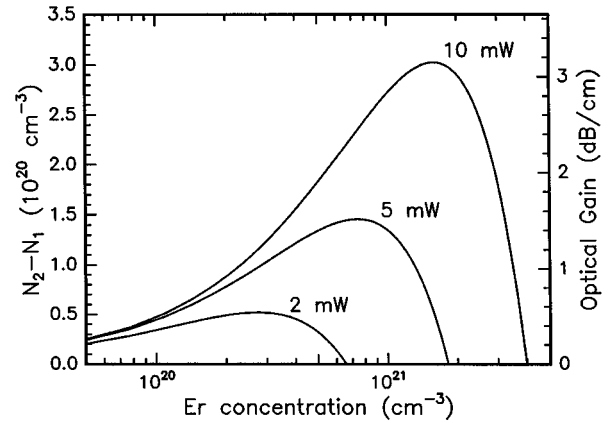


FIG. 35. Difference between the concentration of Er in the first excited state and that in the ground state, $N_2 - N_1$, vs the concentration in the waveguide. Results are shown for three pump powers in the waveguide (1.48 μ m). The right axis shows the corresponding optical gain at 1.53 μ m, excluding waveguide losses. Upconversion and ESA are taken into account. (From Ref. 65.)

a factor of 10 smaller than the maximum absorption cross section for excitation of the first excited state.

The upconversion coefficient of 4×10^{-18} cm³/s measured here for Er in Al₂O₃ is similar to that found for Er-doped soda-lime glass and much lower than that for P-doped silica glasses (see Table IV). It is also much lower than that for Er-doped YAG, which has a similar crystal structure as Al₂O₃ ($C_{up} = 5.4 \pm 10^{-17}$ cm³/s).⁶⁷

One possible way to lower the upconversion coefficient is by adding heavy elements to the Al₂O₃ matrix in order to lower the phonon energy. On the other hand, a lower phonon energy would also result in a longer lifetime for the $^4I_{11/2}$ energy level, causing a buildup of population in this level, and thus reducing the population of the first excited state. Measurements on Er-implanted Y₂O₃, a low-phonon host, will be discussed in Sec. IV D.

The coefficients determined in our discussion here may now be used to calculate the optimum Er concentration for an Er-doped optical amplifier operating at 1.53 μ m. The optical gain is given by $\sigma^e N_2 - \sigma^a N_1$ times the fraction of signal light that propagates in the core of the waveguide. N_1 and N_2 are the Er concentrations in the ground and first excited states, respectively. At 1.53 μ m, $\sigma^e \approx \sigma^a$ (see Fig. 31), so the important parameter becomes $N_2 - N_1$. Figure 35 shows calculations of $N_2 - N_1$ versus the Er concentration in an Al₂O₃ waveguide for three different pump powers based on all the parameters discussed above.

The right axis in Fig. 35 shows the corresponding calculated optical gain at 1.53 μ m (excluding waveguide loss). The Er concentration is assumed to be constant within the core of the guide, and 40% of the signal is confined in the core. As can be seen, for each pump power there is an optimum Er concentration that increases with increasing pump power. For low pump power the maximum achievable optical gain is small, and above a certain concentration threshold the optical gain begins to decrease because there is not enough pump power to excite all the Er³⁺. The higher the pump power, the higher this concentration threshold, and the higher the optical gain. Figure 35 shows that high values of

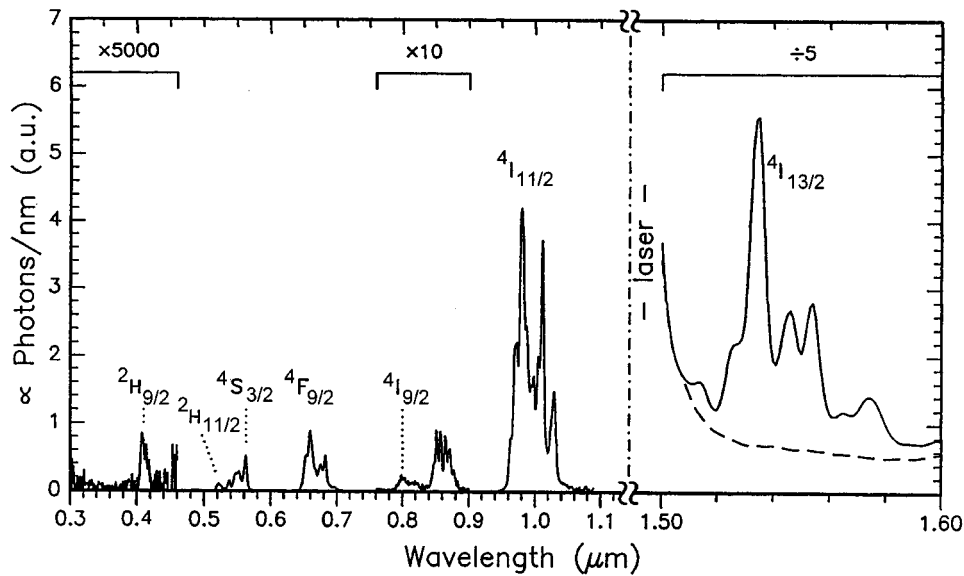


FIG. 36. Room-temperature PL spectrum of an Er-implanted (1×10^{16} Er/cm², 800 keV) Y₂O₃ film. A 1.48 μ m pump laser was coupled into the planar waveguide and the luminescence was detected through a fiber positioned normal to the sample surface, close to the input pump fiber. (From Ref. 14.)

optical gain at 1.53 μ m (0.5–3 dB/cm) can be achieved even for low pump powers (2–10 mW). Note that the calculations are performed in the small signal limit, i.e., the signal power is much smaller than the pump power. Optical gain measurements in Al₂O₃ waveguides will be discussed in Sec. IV E.

D. Upconversion in Y₂O₃

Y₂O₃ is an interesting host material for Er³⁺ because Er₂O₃ and Y₂O₃ have the same crystal structure with nearly the same lattice constant, and the ionic radii of Y³⁺ and Er³⁺ are very similar (0.0892 nm vs 0.0881 nm). Y₂O₃ waveguide films can be made using, e.g., reactive sputter deposition,^{68,69} and channel waveguides with optical losses of around 0.5 dB/cm can be made using ion beam etching.

Polycrystalline Y₂O₃ films 500 nm thick were deposited on a 3- μ m-thick thermally grown SiO₂ film on a Si(100) wafer and subsequently implanted¹⁴ with 800 keV Er to a fluence of 1×10^{16} Er/cm². The Er profile peaks at a depth of 140 nm with a FWHM of 100 nm and a peak concentration of 0.75 at. %. The implanted layer was annealed in vacuum at 700 °C for 1 h. The end faces of the sample were mechanically polished and a 1.48 μ m pump beam was coupled into the planar waveguide through a tapered optical fiber. Figure 36 shows a room-temperature PL spectrum of the Er-doped planar waveguide collected using an optical fiber positioned normal to the waveguide surface, close to the input pump fiber. The laser power in the input fiber was 43 mW, corresponding to an input power density on the order of 10^6 W/cm². As no channel waveguide was made to confine the light in one dimension, the power density rapidly decreases along the waveguide due to diffraction.

The infrared part of the spectrum (1.1–1.6 μ m) shows the typical Er³⁺ luminescence peaking at 1.534 μ m superimposed on a background due to scatter from the pump laser at 1.48 μ m. The spectrum also shows clear and manifold peaked luminescence around 410, 525, 550, 660, 800, 980,

and 1534 nm that is attributed to transitions from the ²H_{9/2}, ²H_{11/2}, ⁴S_{3/2}, ⁴F_{9/2}, ⁴I_{9/2}, ⁴I_{11/2}, and ⁴I_{13/2} to the ground state manifold, respectively (see Fig. 20 for a level diagram). The peak around 860 nm can be ascribed to radiative decay from the ⁴S_{3/2} state to the first excited ⁴I_{13/2} state. The sharply resolved manifold lines indicate that inhomogeneous broadening is small, even at room temperature. This implies that the Er³⁺ ions are located on well-defined positions in the Y₂O₃ crystal. Note that the Er³⁺ emission from Er-implanted polycrystalline Al₂O₃ films showed a much broader spectrum (Fig. 28). The difference may be attributed to the larger size mismatch for Er and Al compared to that for Er and Y. A difference in the grain structure of the two types of films may also affect the PL line shape.

PL lifetime measurements were performed on the Er-implanted Y₂O₃ planar waveguide at different wavelengths, and are shown in Fig. 37. The 1.534 μ m decay shows non-exponential behavior similar to that observed for soda-lime glass. (Sec. III E) and Al₂O₃ (Sec. IV C) channel waveguides at high pump powers. The 1/e decay time is 6.0 ms. The decay traces for the 980, 660, and 560 nm emissions showed decay times of 2.5, 0.9, and 0.9 ms, respectively.

All emission peaks, apart from the one at 1.535 μ m, are due to upconversion interactions between the Er³⁺ ions. From a systematic study of both the power dependence of all emission lines¹⁴ and the lifetime measurements in Fig. 37 it follows that the higher energy emissions are due to first and second order cooperative upconversion, promoting Er³⁺ ions to the ⁴I_{9/2} and ⁴F_{7/2} levels, respectively. From the higher lying levels, direct decay to the ground state or decay to lower lying states will take place, resulting in the various emission lines in Fig. 36. The very small ultraviolet contribution at 410 nm can be attributed to ESA of an Er³⁺ ion in the ⁴S_{3/2} state, or from upconversion involving Er³⁺ ions in the ⁴S_{3/2} and ⁴I_{13/2} states.

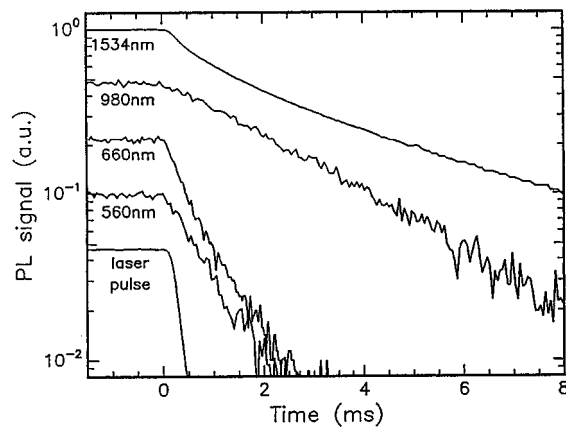


FIG. 37. Room-temperature PL decay measurements for Er-implanted Y_2O_3 ($1 \times 10^{16} \text{ cm}^{-2}$, 800 keV, 0.75 at. % peak, annealed at 700 °C), taken at 560, 660, 980, and 1534 nm. The laser pulse timing is indicated schematically. (From Ref. 14.)

A rough estimate of the upconversion coefficient in Y_2O_3 was made in Ref. 14; it amounts to $C_{\text{up}} = 5 \times 10^{-19} \text{ cm}^3/\text{s}$, an order of magnitude smaller than that in Al_2O_3 (see Table IV). This may be explained by the combined effect of (1) the narrow emission and absorption spectra in Y_2O_3 which make the upconversion effect off resonant, and (2) the low phonon energies in Y_2O_3 which cause multiple phonons to be required to bridge the mismatch for upconversion. The strongest fundamental lattice vibrations in Y_2O_3 occur in the $300\text{--}380 \text{ cm}^{-1}$ range,⁷⁰ much lower than in, for example, Al_2O_3 (870 cm^{-1})⁷¹ or silica (1100 cm^{-1}).

Despite the low value for C_{up} , however, the data in Fig. 36 show that upconversion is actually rather efficient in Y_2O_3 . Stronger upconversion emission is observed in Y_2O_3 than in Al_2O_3 , although the measurements on Y_2O_3 were made on planar waveguides, with much less confined optical modes than the channel waveguides for Al_2O_3 . In fact, the small UV emission at 410 nm is only observed in Y_2O_3 and not in Al_2O_3 . The efficient upconversion in Y_2O_3 is a consequence of the long luminescence lifetimes of the Er^{3+} levels. For example, while the 980 nm emission lifetime in Y_2O_3 is 2.5 ms, it is $< 1 \mu\text{s}$ in silica and $30 \mu\text{s}$ in Al_2O_3 . This indicates that fast nonradiative relaxation of excited Er^{3+} ions is not prevalent in Y_2O_3 . This is due to the relatively low-phonon energy in this material. The long lifetimes in Y_2O_3 will lead to the buildup of large populations of the higher lying levels due to upconversion.

Although upconversion processes put a limit on the performance of optical amplifiers operating at $1.5 \mu\text{m}$, they may be used to fabricate visible and possibly even ultraviolet lasers pumped with readily available infrared pump sources. Several reports have already shown upconversion lasing in bulk rare-earth-doped materials^{72–76} and optical fibers.⁷⁷ Reports on upconversion lasing in planar waveguides are beginning to appear as well.^{78,79}

E. Optical gain in Al_2O_3

Optical gain measurements were performed⁸⁰ on Al_2O_3 channel waveguides doped with Er by multiple energy (100–

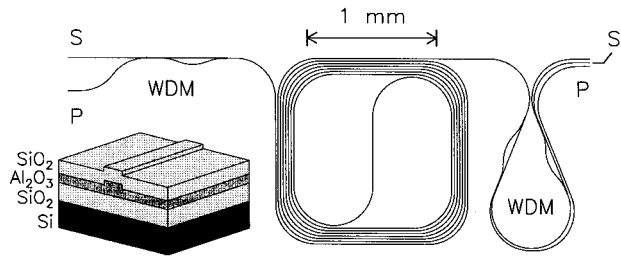


FIG. 38. Layout of a 4-cm-long Er-doped spiral waveguide amplifier integrated with wavelength division multiplexers (WDMs). *P* and *S* indicate the pump and signal in- and outputs. In the actual device, the waveguide between the spiral and output WDM is longer than drawn here. The inset shows a cross section through the waveguide. The Al_2O_3 core dimensions are $0.6 \times 2.0 \mu\text{m}$. (From Ref. 80.)

1500 keV) Er implantation to a total fluence of $1.2 \times 10^{16} \text{ Er/cm}^2$. In this way, the top half of the waveguide was doped at a constant Er concentration of 0.28 at. % Er ($2.7 \times 10^{20} \text{ Er/cm}^3$). Using photolithography and etching, a spiral waveguide structure was made; it is shown sketched in Fig. 38.

Several optical functions are combined in this photonic integrated circuit. Pump and signal beams are coupled into separate waveguides indicated in Fig. 38 by *P* and *S*, respectively. Pump and signal are then combined into a single waveguide using a wavelength division multiplexer (WDM). The amplifying section consists of a 4-cm-long waveguide, rolled up to fit into an area 1 mm^2 . After amplification, two WDM structures are used to separate the pump and signal beams. The WDMs operate on the multimode interference principle; their design is discussed in Sec. IV F.^{81,82} The entire device fits within an area of $1.5 \times 9.5 \text{ mm}^2$. The pump and signal beams were coupled in through tapered optical fibers that were aligned with the input waveguides using piezo actuators.

Measurements of the enhancement of the $1.53 \mu\text{m}$ optical signal intensity as a function of $1.48 \mu\text{m}$ pump power were performed and are shown in Fig. 39. The pump power in the waveguide was derived from the measured pump power in the input fiber using a fiber-to-chip coupling loss of 7 dB, described in Ref. 80. Figure 39 shows that as the pump power is increased the signal rapidly increases; the net optical gain is reached at a pump power of 3 mW in the waveguide. For higher pump powers, saturation of the gain is observed; at 9 mW a net (small-signal) gain of 2.3 dB is achieved.

Calculations of the optical gain were performed based on a rate equation model for the Er^{3+} ions. All calculations include a waveguide loss of 0.35 dB/cm .⁵⁴ In the calculation, the Er^{3+} population in the ground state and in the first and second excited states is considered, and upconversion, effects of pump and signal emission, and absorption (also through ESA) are taken into account. The changes in pump and signal intensities are integrated numerically along the length of the waveguide. The parameters used in the calculation were all determined earlier in this article and are listed in Table V.

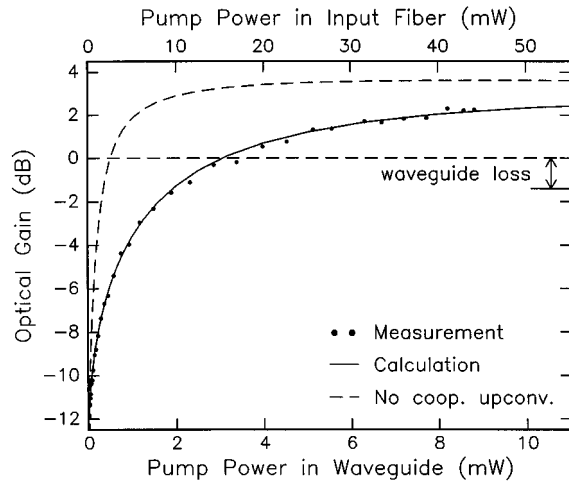


FIG. 39. Measurement of the (small-signal) optical gain at $1.53 \mu\text{m}$ in the waveguide structure of Fig. 38 as a function of pump power in the input fiber (top axis) and in the waveguide (bottom axis). The pump wavelength was $1.48 \mu\text{m}$ and the waveguide is doped with $2.7 \times 10^{20} \text{ Er/cm}^2$ (0.28 at. %). Calculations of the data are included for two cases: with and without upconversion. (From Ref. 80.)

The solid line in Fig. 39 is a calculation of the optical gain as a function of pump power for this particular amplifier. Also shown is a calculation in which the effects of cooperative upconversion are set to zero (dashed line). In this case, the net gain would be achieved at 0.5 mW, and a higher saturation value would be reached. This shows that cooperative upconversion is one of the main limiting factors in the performance of Er-doped waveguide amplifiers. Note that the saturation gain is determined by the maximum degree of inversion that is achievable using a pump wavelength of $1.48 \mu\text{m}$: 78%. Measurements as a function of signal wavelength show a net gain bandwidth of 50 nm at 9 mW pump power.⁸⁰

Several improvements are possible in the design of the waveguide. Figure 40 shows a calculation of the small-signal optical gain of an optimized Er-doped Al_2O_3 waveguide amplifier based on the experimental results of this study. In this

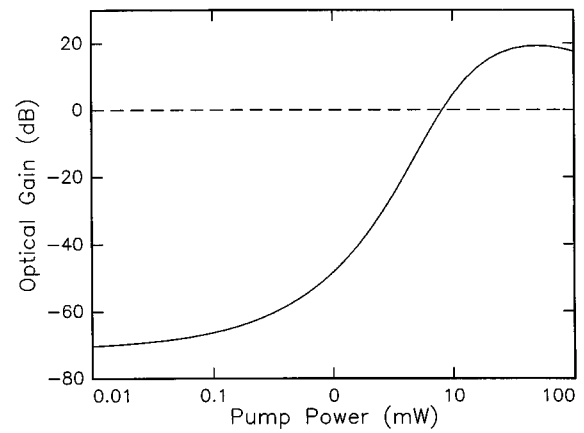


FIG. 40. Calculation of the optical gain at $1.53 \mu\text{m}$ in an optimized waveguide amplifier (length 15 cm) for a $1.48 \mu\text{m}$ pump. The waveguide is doped with $2.7 \times 10^{20} \text{ Er/cm}^2$ throughout the core of the waveguide. (From Ref. 80.)

calculation, the Er was distributed throughout the complete core of the waveguide, rather than in the top half of the waveguide as was the case for the Er-implanted films above. This may be achieved by, e.g., cosputtering Er and Al_2O_3 during the fabrication of the waveguide films rather than using ion implantation. The waveguide is chosen to be 15 cm long, and the Er concentration is the same as above ($2.7 \times 10^{20} \text{ cm}^{-3}$). As can be seen, a net optical gain of nearly 20 dB is possible at a pump power of 50 mW. The proposed 15-cm-long spiral amplifier can fit within the same area ($1.5 \times 9.5 \text{ mm}^2$) as the 4-cm-long amplifier fabricated here. In Fig. 40 the effect of excited state absorption is also apparent: For pump powers above 50 mW the gain decreases because ESA depletes the population of the $^4I_{13/2}$ level. The saturation signal output power is calculated to be 7 dB m (5 mW).

The Er-implanted Al_2O_3 waveguides described here show the best performance of a planar amplifier reported so far. Optical gain has been demonstrated in Er-doped channel waveguides, doped with relatively low Er concentrations. Consequently, the waveguide length required to achieve reasonable gain was rather large (10 cm and larger).^{83–86} Because of the large optical mode dimensions of these devices, high pump powers ($\approx 100 \text{ mW}$) are necessary to reach the net gain. In addition, due to their large waveguide bending radius ($\approx \text{cm}$) these amplifiers take up a large area on a planar substrate.

F. Optical mode imaging

While upconversion is an unwanted effect in Er-doped waveguide amplifiers, it can be used in an advantageous way to probe the local optical mode densities in optical waveguide structures, as will now be described. Direct imaging of the light intensity distribution in a waveguide is difficult, since the light propagates along the waveguide, and only a small fraction of the intensity is scattered in other directions. Imaging of this scattered light is possible, but because scattering occurs at inhomogeneities in the waveguide, the scattered light does not directly relate to the intensity distribu-

TABLE V. Parameters used in the upconversion and optical gain calculations in Al_2O_3 .

Parameter	Symbol	Value
Er concentration	[Er]	$2.7 \times 10^{20} \text{ Er/cm}^2$
Pump wavelength	λ_p	$1.48 \mu\text{m}$
Signal wavelength	λ_s	$1.53 \mu\text{m}$
Pump absorption cross section	σ_p^a	$2.7 \times 10^{-21} \text{ cm}^2$
Pump emission cross section	σ_p^e	$0.77 \times 10^{-21} \text{ cm}^2$
Signal absorption cross section	σ_s^a	$5.8 \times 10^{-21} \text{ cm}^2$
Signal emission cross section	σ_s^e	$6.1 \times 10^{-21} \text{ cm}^2$
ESA cross section ($^4I_{13/2} + \text{pump} \rightarrow ^4I_{9/2}$)	σ_{ESA}	$0.85 \times 10^{-21} \text{ cm}^2$
Er^{3+} first excited state lifetime ($^4I_{13/2}$)	τ	7.8 ms
Er^{3+} second excited state lifetime ($^4I_{9/2}$)		30 μs
Cooperative upconversion coefficient ($^4I_{13/2} + ^4I_{13/2} \rightarrow ^4I_{9/2} + ^4I_{15/2}$)	C_{up}	$4 \times 10^{-18} \text{ cm}^3/\text{s}$
Waveguide amplifier length		4 cm
Waveguide loss		0.35 dB/cm
Optical mode size		$0.6 \times 2.0 \mu\text{m}^2$
Overlap mode intensity with Er profile		36%

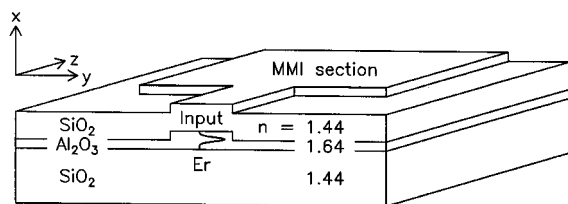


FIG. 41. Schematic of an Er-implanted Al_2O_3 multimode interference waveguide. The 21- μm -wide multimode section is center fed by a 2- μm -wide input waveguide. The refractive indices of the layers are indicated, together with the Er depth profile. (From Ref. 82.)

tion. Other methods for studying intensity distributions in waveguides such as imaging of the cleaved end faces of the waveguide only give the field intensity distribution at the end face, and they are destructive.

By imaging the isotropically emitted 540 nm upconversion luminescence from the Er^{3+} ions, the intensity distribution, and therefore the optical modes of the 1.48 μm pump light in the waveguide, can be measured. A multimode interference (MMI) coupler structure is used to demonstrate this principle.⁸² A 600-nm-thick Al_2O_3 film was doped with Er using 1.3 MeV Er ion implantation, with the sample held at 77 K during the implant. The Er fluence was $1.62 \times 10^{16} \text{ Er/cm}^2$. The Er implantation profile has a Gaussian shape and is peaked at a depth of 270 nm with a FWHM of 160 nm, as shown by RBS measurements. The Er peak concentration is 1.4 at. %. A 21- μm -wide MMI section, center fed by a 2- μm -wide input waveguide was used and is described elsewhere.⁸² Figure 41 shows a schematic of the MMI structure.

Approximately 5 mW of 1.48 μm light from an InGaAsP pump laser was coupled into the single-mode section. The luminescence emission from the multimode section was imaged using an optical microscope that was mounted normal to the sample surface (x dimension in Fig. 41).

Figure 42(a) shows a two-dimensional image of the 21- μm -wide Er-doped Al_2O_3 MMI waveguide section pumped with 1.48 μm laser light. The original image is clearly visible to the eye, and the emission spectrum peaks in the green at 540 nm. In Fig. 42(a) the green intensity distribution is converted to a gray scale. A distinct interference pattern is

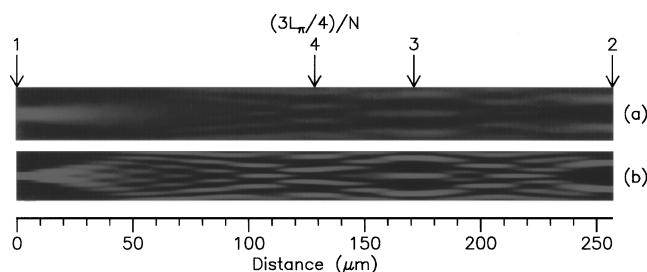


FIG. 42. (a) Optical microscope image of the upconversion luminescence from an Er-doped (1.4 at. % Er) multimode interference coupler pumped at 1.48 μm . The originally green intensity distribution was converted to gray scale. (b) Calculation of the optical mode density by using the rate equations governing the infrared-to-green upconversion process. The arrows indicate the positions of the input (1), and of two- three-, and fourfold images of the input field. (From Ref. 82.)

observed due to the interference of six different optical modes that are coherently excited at the entrance of the MMI section. Because the different modes propagate at different phase velocities, phase shifts between the modes occur and lead to interference. An interesting feature of multimode interference is its self-imaging property: At certain positions in the waveguide single or multiple images of the input intensity distribution are reproduced. Self-imaging and other interference effects are applied in many integrated optic devices for the routing, splitting, switching, and multiplexing of light.^{81,87-90}

Figure 42(b) shows the calculated upconversion luminescence intensity profile. It is based on the coherent superposition of the six modes, which gives the total 1.48 μm intensity, that is then converted to green intensity profiles using the upconversion rate equations and coefficients determined in Sec. IV C. The calculated intensity distribution resembles the measured profile quite well.

Note that the technique of using upconversion luminescence in principle allows for probing the 1.48 μm mode intensity in the waveguide at the diffraction limit of the luminescence light. For the 540 nm light used here, this means the measuring resolution is ~ 3 times better than if the 1.48 μm pump light propagating in the waveguide were imaged directly. This technique can now be used to study optical mode densities in more complicated waveguide structures and in photonic bandstructure⁹¹ materials.

V. LiNbO_3

A. Amorphization and recrystallization

LiNbO_3 is a key material in integrated optics due to its excellent nonlinear optical properties. Optical switches and modulators have been made in LiNbO_3 and are commercially available. Rare-earth-doped waveguide amplifiers in LiNbO_3 could be used to compensate for the intrinsic optical losses in such splitters and modulators. In addition, the electro-optical properties can be used to fabricate rare-earth-doped mode-locked, Q -switched, or tunable waveguide lasers.^{92,93} Planar and channel waveguides can be made in LiNbO_3 by Ti indiffusion or proton exchange, and they show optical losses as low as 0.1–0.2 dB/cm.⁹³

Ion implantation is an attractive technique by which to dope LiNbO_3 with Er as it enables adjustment of the Er depth profile to the shape of the optical mode profile. Experiments were performed⁹⁴⁻⁹⁶ on commercially available x -cut LiNbO_3 single crystals that were implanted at room temperature with $5 \times 10^{15} \text{ Er/cm}^2$ at 3.5 MeV. Figure 43 shows a RBS channeling spectrum of an Er-implanted ($5 \times 10^{15} \text{ Er/cm}^2$, 3.5 MeV) LiNbO_3 single crystal.

As can be seen in Fig. 43, a 1.25- μm -thick fully disordered surface layer has formed after implantation. The TEM diffraction image of this layer is shown in Fig. 44(a) and shows it is fully amorphous. Channeling spectra are also shown in Fig. 43 after rapid thermal annealing (RTA) in flowing O_2 at 500 $^\circ\text{C}$ for 20 and 40 s. As can be seen, the layer recrystallizes in a layer-by-layer fashion, at a rate of $32 \pm 5 \text{ nm/s}$, leaving behind highly any disordered material. Longer annealing at 500 $^\circ\text{C}$ does not improve the crystal

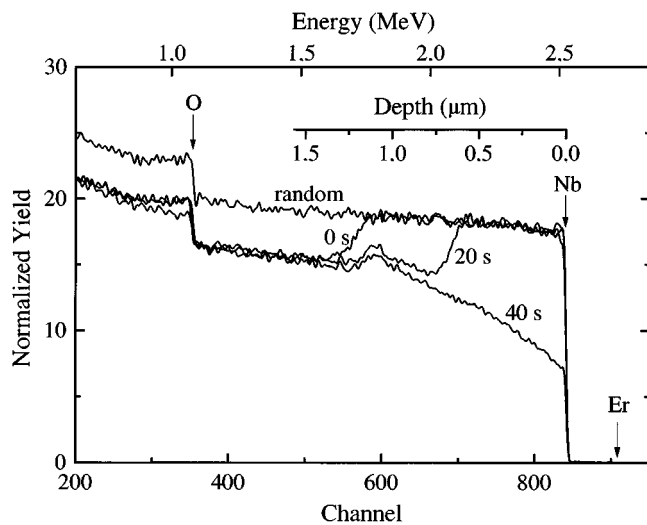


FIG. 43. RBS channeling spectra of Er-implanted (5×10^{15} Er/cm², 3.5 MeV) single crystal LiNbO₃. Spectra are shown after implantation and after RTA at 500 °C for 20 or 40 s. (From Ref. 95.)

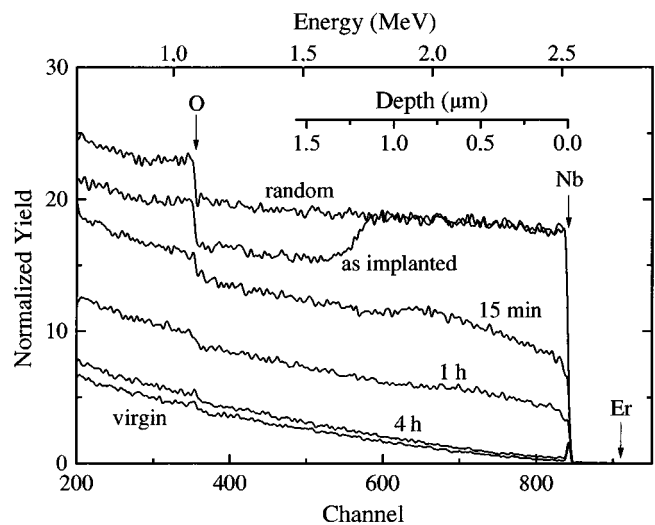


FIG. 45. RBS channeling spectra of Er-implanted (5×10^{15} Er/cm², 3.5 MeV) x-cut LiNbO₃ single crystals annealed for different times at 1060 °C in a wet oxygen atmosphere. Also shown is the random spectrum of the as-implanted sample. (From Ref. 95.)

quality. No segregation or redistribution of Er is observed after annealing at 500 °C (not shown).

Figure 45 shows channeling spectra of implanted samples (3.5 MeV, 5×10^{15} Er/cm²) after annealing at 1060 °C in a vacuum tube furnace for times up to 4 h. Annealing for 15 min results in the formation of a highly disordered layer with a minimum yield $\chi_{\min} = 40\% - 60\%$. The plan-view bright-field TEM image of this sample is shown in Fig. 44(b). It reveals grains with a typical size of 0.5–1.5

μm. The diffraction pattern [Fig. 43(c)] demonstrates that the layer is fully crystalline and that all crystals have the same orientation. These data indicate that tube furnace annealing at 1060 °C results in a columnar epitaxial crystallization process. The large density of grain boundaries then explains the high yield in the channeling RBS spectra. Prolonged annealing for 1 or 4 h leads to a further reduction in the channeling yield (Fig. 45) that is attributed to grain growth. After annealing at 8 h (not shown) the channeling data are identical to those for a virgin sample. Secondary ion mass spectrometry (SIMS) data on annealed samples (not shown)⁹⁵ showed significant diffusion of Er after annealing at 1060 °C, and a diffusion coefficient of 8×10^{-14} cm²/s.⁹⁵

By combining the data for the 500 and 1060 °C anneals (Figs. 43 and 45), the following can be concluded. Solid phase epitaxy (SPE) of the amorphous LiNbO₃ layer takes place at 500 °C and leads to the formation of crystalline columns. This columnar epitaxy will also take place during the heating transient in the tube furnace as it is heated up to 1060 °C. Note that the typical heating rate in the particular furnace is 10 °C/s and SPE at 500 °C takes place in typically 40 s. The prolonged annealing at 1060 °C then serves to cause grain growth and epitaxial alignment of the columnar structure, leading to a perfect crystal after 8 h at 1060 °C.

High temperature anneals were also performed in a RTA at higher heating rates than were achievable in a tube furnace. Figure 46 shows a RBS channeling spectrum for a sample annealed in the RTA at 1060 °C for 1 min using a heating rate of 100 °C/min. In this spectrum, χ_{\min} is only $2.3 \pm 0.2\%$, identical to the value found for virgin samples. Plan-view TEM showed⁹⁶ that the sample is single crystal with no grain boundaries. The channeling spectrum from Fig. 45 for the 15 min furnace anneal at 1060 °C is also plotted for comparison, and shows much higher disorder than the RTA annealed sample. A sample annealed in the RTA at

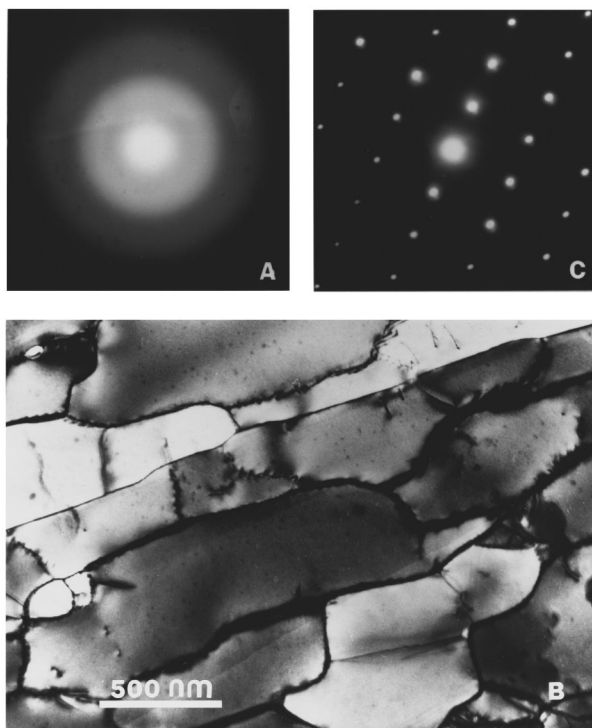


FIG. 44. Plan-view TEM image of an Er-implanted (5×10^{15} Er/cm², 3.5 MeV) x-cut LiNbO₃ single crystal. Electron diffraction patterns are shown (a) after implantation and (c) after annealing for 15 min at 1060 °C. (b) A plan-view bright-field image after annealing at 1060 °C. (From Ref. 95.)

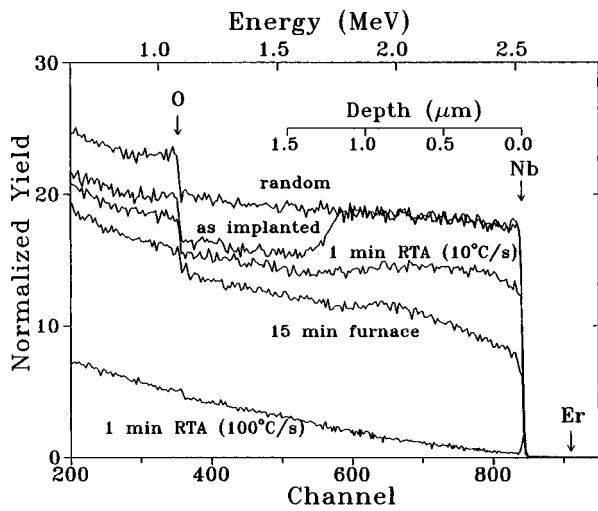


FIG. 46. RBS channeling spectra of Er-implanted (5×10^{15} Er/cm², 3.5 MeV) x-cut LiNbO₃ single crystals. One sample was annealed for 15 min at 1060 °C in a tube furnace, and two others were annealed for 1 min at 1060 °C in a RTA at two different heating rates (10 or 100 °C/s). Random and channeling spectra for an as-implanted sample are also shown. (From Ref. 94.)

a lower heating rate (10 °C/s), comparable to that in the tube furnace, also shows high disorder (see Fig. 46).

These data indicate that the heating rate during annealing is crucial in determining the final crystal quality. Additional TEM data by Fleuster⁹⁶ have shown that slow heating results in a large grain structure with high disorder that is hard to anneal (long anneal times are required at 1060 °C). In contrast, fast heating initially leads to the random nucleation of a fine grained structure that has no orientation relation to the substrate. As the annealing continues, this fine grain polycrystalline layer is epitaxially aligned, a process that takes less time than alignment of a coarse grained columnar structure, and as a result nearly perfect epitaxy is achieved after only 1 min, and with only very slight Er diffusion or segregation.⁹⁶ Samples crystallized at 1060 °C for 1 min show essentially the same PL intensity and lifetime as those annealed for longer times at 1060 °C.

B. Optical activation

Figure 47 shows room-temperature PL spectra of Er-implanted (5×10^{15} Er/cm², 3.5 MeV) LiNbO₃ single crystals annealed in the RTA in flowing oxygen for different times at 500 °C.⁹⁵ All measurements were performed using a 496.5 nm pump beam. The spectrum for an as-implanted sample shows a clearly measurable signal at room temperature. It is rather broad (48 nm FWHM), and peaks at 1.533 μm. It was found that the PL intensity increased by a factor of 5 as the laser irradiation continued for 2 h during a PL measurement. This indicates that irreversible photoinduced structural changes take place in amorphous LiNbO₃ during laser irradiation.

Thermal annealing at 500 °C at increased lengths of time causes an increase in intensity and a sharpening of the PL spectrum. This is consistent with the fact that prolonged annealing at 500 °C causes a gradual crystallization of the layer

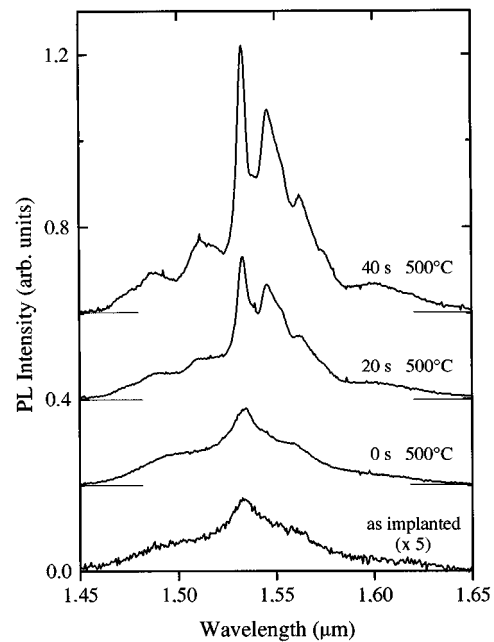


FIG. 47. Room-temperature PL spectra of Er-implanted (5×10^{15} Er/cm², 3.5 MeV) LiNbO₃ single crystals annealed for different times at 500 °C in flowing oxygen using RTA. The "0 s" sample was heated to 500 °C and then quenched; the 20 and 40 s samples were each held at 500 °C for their respective times and then quenched. ($\lambda_{\text{pump}} = 496.5$ nm, pump power = 100 mW, resolution = 3.2 nm). The spectra were shifted vertically for clarity. (From Ref. 95.)

as is shown in Fig. 43. Crystallization leads to incorporation of Er on a well-defined lattice site and hence a sharper PL spectrum. Work on melt-doped and indiffused LiNbO₃ has shown that Er is incorporated on an octahedral position close to the Li site^{97,98} that is surrounded by six oxygen atoms.

The sample annealed at 500 °C for 40 s shows a 10 times higher PL intensity than the as-implanted (amorphous) layer. At the same time the PL lifetime at 1.533 μm (data not shown) increased from 1.65 (amorphous) to 2.9 ms (crystallized).⁹⁵ Both the spectrum and lifetime after annealing are very similar to that of bulk Er-doped LiNbO₃ grown from the melt ($\tau = 3.0$ ms).

The tenfold intensity increase upon annealing is attributed to this lifetime increase as well as to an increase in the optically active Er concentration. It should be noted that additional annealing at 1060 °C (which increases the crystal quality, as shown in Sec. V A) did not significantly increase the PL intensity or lifetime. Annealing at such a high temperature did, however, lead to significant diffusion of the implanted Er.⁹⁵ Therefore, to take advantage of the Gaussian-implanted Er depth profile in planar waveguide structures, low temperature (e.g., 500 °C) anneals should be used. More research is needed to study the optical properties, such as scattering loss and absorption in such low-temperature annealed films, which are full of grain boundaries as shown in Fig. 44.

Figure 48 shows the concentration dependence of the 1.53 μm PL intensity and lifetime in LiNbO₃.⁹⁴ Samples were implanted with 3.5 MeV Er at fluences ranging from 5×10^{14} to 3×10^{16} Er/cm², corresponding to peak concentrations from 0.05 to 0.44 at. %. After implantation all

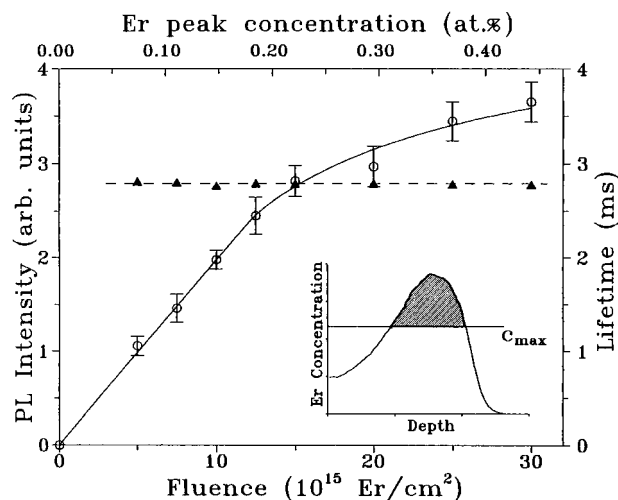


FIG. 48. PL intensity and lifetime as a function of Er fluence (3.5 MeV) in x-cut LiNbO₃ after annealing at 1060 °C for 1 min in RTA (heating rate 100 °C/s.). The corresponding Er peak concentration is plotted on the top axis. The inset shows a schematic of the Er depth profile and the limit to the Er concentration that can be optically activated in LiNbO₃. (From Ref. 95.)

samples were annealed in a RTA at 1060 °C for 1 min (100 °C/s rise time) in flowing O₂. The PL intensity shows a linear increase with fluence for Er fluences up to 1.5×10^{15} Er/cm², and levels off above this fluence. The luminescence lifetime at 1.53 μ m is independent of concentration: 2.8 ms. The leveling off of the PL intensity at high Er concentration suggests that there is a limit to the concentration of Er³⁺ ions that can be optically activated in LiNbO₃, [Er]_{max}. Any Er at concentrations above [Er]_{max} would then remain inactive. Using measured Gaussian Er depth profiles for each fluence, the total areal density of optically active Er can then be determined by calculating the integrated areal density of Er below [Er]_{max}, as indicated schematically by the inset in Fig. 48. The areal density should then be proportional to the Er PL data in Fig. 48. Such a procedure was performed using the Er depth profiles for the different fluences, measured using SIMS,⁹⁴ with [Er]_{max} as a free parameter. The result for the best fit is shown as the line drawn in Fig. 48 and corresponds to a value for [Er]_{max} of 0.18 at. %. This is close to the equilibrium solubility of Er in LiNbO₃.

Estimates of the cooperative upconversion coefficient for Er-implanted and annealed LiNbO₃ were also made and showed that $C_{up} < 1.4 \times 10^{-19}$ cm³/s.⁹⁶ This is much smaller than that for Er-doped silica glasses or Al₂O₃ (see Secs. III E and IV C). This may be attributed to the rather narrow emission and absorption spectra of Er in LiNbO₃ that causes the upconversion energy transfer process to be less resonant.

VI. SILICON

A. Crystal Si

Erbium doping of silicon has recently become an extensively studied subject because of the possibility of obtaining light emission from Si at 1.5 μ m. In a semiconductor, optically or electrically generated charge carriers can recombine at an Er-related trap site in the crystal and transfer their recombination energy to the Er³⁺ ion, which then becomes

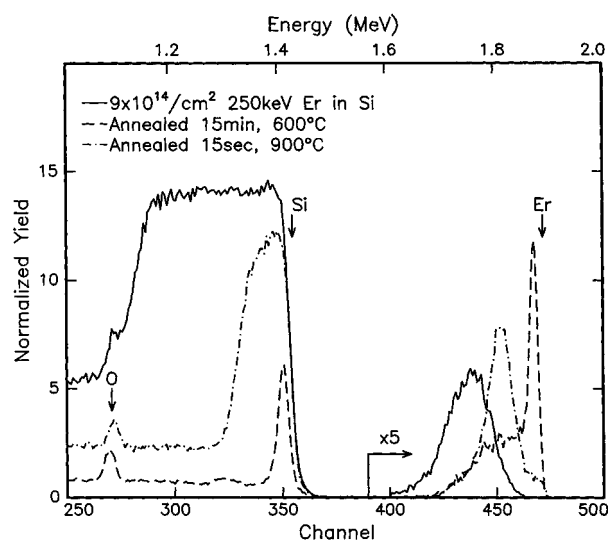


FIG. 49. RBS channeling spectra for Er-implanted (9×10^{14} Er/cm², 250 keV) CZ-Si(100) at 90 K. Spectra are shown after implantation and after annealing at 600 or 900 °C. The Er portion of the spectra was magnified by a factor of 5. (From Ref. 100.) The surface channels of O, Si, and Er are indicated by arrows.

excited and subsequently decays by the emission of a photon. In this way, it may be possible to obtain efficient light emission from Si that is otherwise impossible due to its indirect band gap. If sufficiently high Er concentrations ($\sim 10^{19}$ – 10^{20} Er/cm³) could be incorporated and optically activated in Si, it would become possible to fabricate light-emitting diodes, lasers, or optical amplifiers based on silicon.⁹⁹ By integrating these devices with electrical functions in the Si chip, opto-electronic integrated circuits may be fabricated.

The equilibrium solubility of Er in Si is not known, but by analogy with the transition metals it is estimated to be 10^{14} – 10^{16} cm⁻³. Therefore, nonequilibrium incorporation methods have to be used to incorporate sufficiently high Er concentrations. Ion implantation is such a method. The incorporation of and the optical properties of Er in crystal and amorphous Si will now be discussed and measurements of electroluminescence in Er-doped Si *p-n* diodes will be given. It should be noted that the field of Er doping of Si is rapidly expanding, and we shall not provide a complete representation of the state of the art at this time. References to other work on Er in Si are given in Sec. VII. A review specifically devoted to Er in Si will be published elsewhere.¹⁰ The latest work on rare-earth-doped semiconductors in general is reported in Ref. 11.

1. Incorporation

a. Solid phase crystallization and segregation. Czochralski (CZ)-grown Si(100) was used in these experiments, with an oxygen background concentration as measured using SIMS of $(1.7 \pm 0.5) \times 10^{18}$ O/cm³. The Si wafer was implanted¹⁰⁰ on one side with 250 keV Er to a total fluence of 9×10^{14} Er/cm². During implantation the sample was kept at 90 K. RBS channeling spectra, shown in Fig. 49 show that a 160-nm-thick amorphous (*a*-Si) surface layer has formed after implantation. The Er profile peaks at a depth of 70 nm

with a FWHM of 60 nm. After annealing for 15 min in a vacuum tube furnace at 600 °C, the *a*-Si layer has recrystallized by SPE, leaving a thin (~ 10 nm) disordered layer at the surface. The channeling minimum yield in the recrystallized layer is $\chi_{\min} < 5\%$, indicating good crystal quality. The Er was redistributed, with 65% of the Er remaining trapped in crystal Si (c-Si) and the remainder in the surface disordered layer. Detailed measurements of the time dependence of the segregation process¹⁰¹ have shown that the Er is segregated in a narrow (nm) segregation spike in the amorphous Si in front of the moving interface. After crystallization the Er profiles are identical under both channeling and random conditions, indicating that the Er is not on substitutional lattice sites nor on tetrahedral interstitial sites.

The crystallization process is very sensitive to the anneal temperature as can be seen in Fig. 49, which also shows a channeling spectrum after annealing at 900 °C. In this case, the initial regrowth is epitaxial, but 60 nm from the surface the quality of the regrown crystal deteriorates rapidly. In the epitaxial region (deeper than 60 nm), Er is trapped at concentrations similar to those for the 600 °C anneal. Once damaged crystal growth begins, Er starts being trapped at higher concentrations. The sample is recrystallized to the surface as evidenced by both the moderate channeling in the Si signal and the redistribution of some Er to the surface. TEM has shown¹⁰⁰ that the damaged surface layer for the 900 °C annealed sample is heavily twinned, which causes the high yield in the RBS channeling spectrum in Fig. 49.

The twinning may be due to disruption of the *a*-Si/*c*-Si growth front by Er precipitation or silicidation in the segregation spike in front of the interface. However, no evidence for the presence of precipitates or silicides was found by high resolution TEM. Alternatively, a high Er concentration in the spike (exceeding the solubility) may cause it to be energetically favorable to nucleate twins, to use the twin boundaries as trapping sites for Er.

The recrystallization process is sensitive not only to the anneal temperature but also to the Er concentration. Figure 50 presents RBS channeling spectra for five different Er doses ($0.4, 0.9, 1.3, 2.4, \text{ and } 5.4 \times 10^{15} \text{ Er/cm}^2$) at 250 keV. Each of these implants creates a 140–160-nm-thick *a*-Si surface layer. Thermal annealing was then performed for 15 min at 600 °C. The Si portion of the channeling spectra [Fig. 50(a)] shows that the two lowest fluence Er samples exhibit good epitaxy with $\chi_{\min} < 5\%$. The higher concentration samples all initially regrow epitaxially, but for each sample epitaxy is disrupted at a certain depth (indicated by arrows). The higher the Er dose, the sooner epitaxial growth is disrupted.

Figure 50(b) shows the Er parts of the RBS spectra plotted on the same depth scale as the Si parts. The two low fluence samples have Er profiles similar to those shown in Fig. 49, with Er trapped in high quality crystal and a narrow Er peak at the surface. The high-dose samples all show rapid increases in Er concentration once epitaxy is disrupted. The comparison of the Er concentrations for each sample at the depth where single crystal regrowth is interrupted (indicated by arrows) demonstrates that epitaxy is disrupted once a fixed Er concentration, $1.2 \times 10^{20} \text{ Er/cm}^3$, in the crystal is

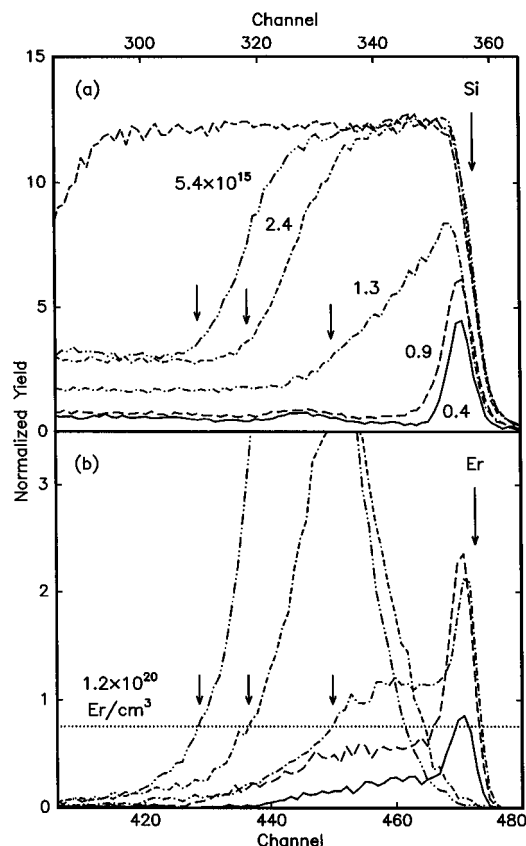


FIG. 50. The (a) Si and (b) Er portions of RBS channeling spectra after 600 °C anneals of CZ-Si(100) implanted with $0.4, 0.9, 1.3, 2.4, \text{ and } 5.4 \times 10^{15} \text{ Er/cm}^2$ at 250 keV. The channel scales are plotted so that Si and Er have the same relative depth scales. The dotted line in (b) indicates the critical concentration where epitaxy is disrupted. (From Ref. 100.)

reached. Additional measurements have shown that this critical concentration depends on the anneal temperature (at 500 °C: $2 \times 10^{20} \text{ Er/cm}^3$; at 900 °C: $6 \times 10^{19} \text{ Er/cm}^3$).¹⁰¹

In experiments under conditions below the threshold for epitaxial breakdown, it was found that the Er segregation coefficient is very Er concentration dependent.¹⁰² Very low Er densities are nearly completely segregated out of the crystal, while at higher Er densities significant partitioning takes place at the *a*-Si/*c*-Si interface with a segregation coefficient of 0.2. These findings were explained in terms of a model¹⁰² in which defects in the *a*-Si near the interface act as traps for the Er. At low Er densities, all the Er would be soluble in these traps, and it can therefore escape from the growing crystal. At high Er fluences, when all traps in the *a*-Si are filled, Er is forced to go into either the crystal or the amorphous layer, and as a result both segregation and trapping are observed.

b. Impurity effects. It has been shown that impurities may affect the segregation and trapping of Er.^{101,103} Figure 51(a) shows RBS spectra for $1.6 \times 10^{15} \text{ Er/cm}^2$ implants into CZ-Si [$(1.7 \pm 0.5) \times 10^{18} \text{ O/cm}^3$], both as implanted, and after annealing at 550 °C. The SPE results in significant segregation, with the Er segregation spike reaching all the way to the surface. Note that the depth scales are very different from the experiments described above that were performed at a low implantation energy (250 keV).

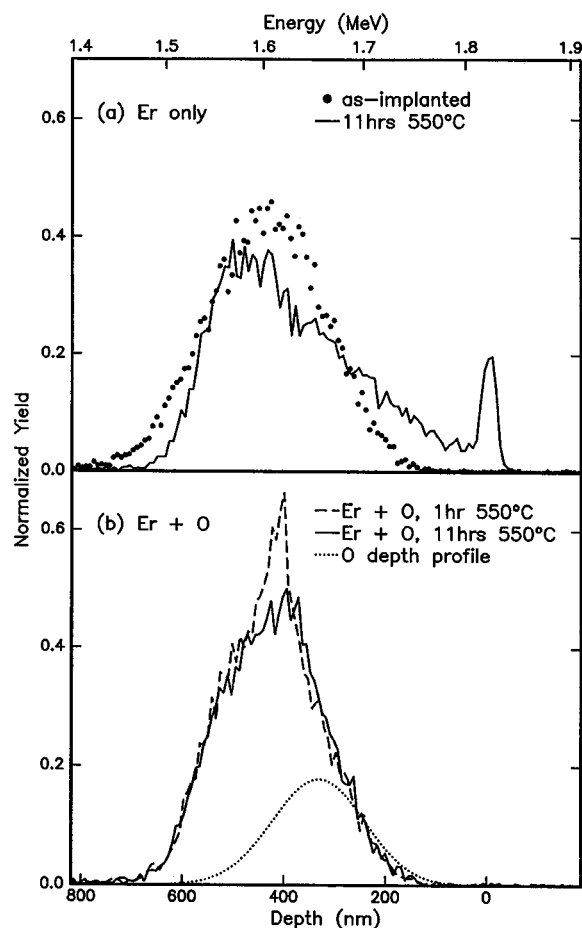


FIG. 51. The Er portion of RBS spectra of (a) 780-nm-thick Er-implanted a -Si (1.6×10^{15} Er/cm², 1.5 MeV), as implanted and after SPE at 550 °C (11 h), (b) after SPE (1 and 11 h) for a similar a -Si layer but coimplanted with 5×10^{15} 160 keV O/cm². The O depth profile is indicated by the dotted line. (From Ref. 102.)

Some samples were coimplanted with 5×10^{15} 160 keV oxygen. This energy was chosen to place the O profiles slightly closer to the surface than the Er profile; this is shown schematically in Fig. 51(b). After SPE at 550 °C, the Er profile coincides almost completely with that for the as-implanted sample, indicating that the presence of oxygen causes a dramatic reduction in the segregation. One explanation is that Er forms complexes with oxygen, and that these complexes are less easily segregated from the crystal. EXAFS measurements on Er- and O-doped Si have shown that Er is indeed coordinated by four to six O atoms.¹⁰⁴ Another explanation for the effect of oxygen is that it fills the defect traps in the a -Si in front of the moving interface, and thereby increases the trapping.

c. Ion beam induced epitaxial recrystallization. Ion irradiation through an a -Si/c-Si interface can be used to cause crystallization at much lower temperatures than are required for pure thermal crystallization. Ion beam induced epitaxial crystallization (IBIEC) experiments were performed on 250 keV 4×10^{15} Er/cm²-implanted samples.¹⁰⁵ IBIEC was performed using a 1 MeV Si beam, which has a range well beyond the Er-doped a -Si surface layer. The total Si fluence was 1×10^{17} ions/cm². The sample was attached with silver

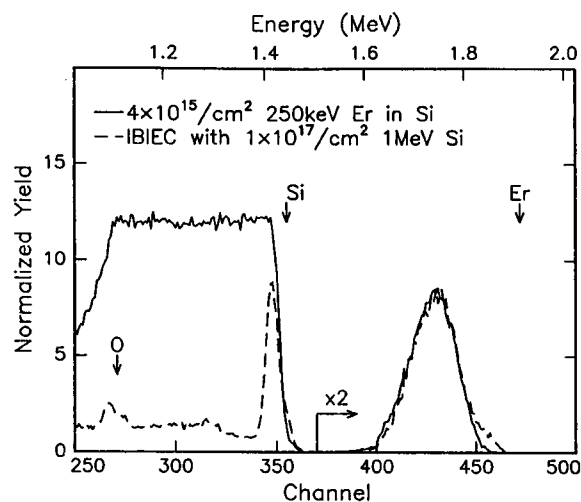


FIG. 52. RBS channeling spectra for Er-implanted (4×10^{15} Er/cm², 250 keV) CZ-Si before and after IBIEC with 1×10^{17} 1 MeV Si/cm² at 320 °C. The Er part of the spectrum is multiplied by a factor of 2. (From Ref. 105.)

paint to a copper block held at a constant temperature of 320 °C.

Figure 52 shows RBS spectra of the Er-implanted sample after IBIEC. A spectrum for the as-implanted sample is also shown. The channeling spectrum after IBIEC shows that the a -Si has regrown to the surface with a < 20 -nm-thick disordered layer remaining at the surface. χ_{\min} of the regrown layer is around 10%. A highly disordered region is observed in the spectrum below channel 250, corresponding to the deep damage caused by the Si beam during IBIEC. The most striking feature in Fig. 52 is that the shape of the Er profiles before and after IBIEC is identical. No segregation has occurred at the moving a -Si/c-Si interface. In this way an Er concentration as high as 1.5×10^{20} cm⁻³ was incorporated into the crystal Si.

2. Optical activation and codoping

a. PL spectra and annealing behavior. Figure 53 shows a PL spectrum (measured at 77 K) of Er-implanted CZ-Si (9×10^{14} Er/cm²) after SPE at 600 °C.¹⁰⁶ The spectrum shows four clear features around 1.131, 1.20, 1.36, and 1.54 μ m, respectively. The first two peaks correspond to phonon-assisted near-band edge (BE) luminescence of Si.¹⁰⁷ The broad band around 1.3 μ m is very similar to defect bands found earlier for ion-damaged Si after annealing.¹⁰⁷ The peak around 1.54 μ m represents the characteristic luminescence from Er³⁺.

A spectrum for the sample regrown by SPE and subsequently annealed at 1000 °C for 15 s is also shown in Fig. 53. As can be seen, the defect band has now disappeared and both the Er and the band edge luminescence have increased. PL decay measurements were performed and they show a slight nonexponential behavior.¹⁰⁸ The typical $1/e$ decay time for both samples in Fig. 53 was 0.8 ms.

The data in Fig. 53 show that the Er PL intensity can be increased five-fold by subsequent thermal annealing at 1000 °C. Anneals were also performed at other temperatures

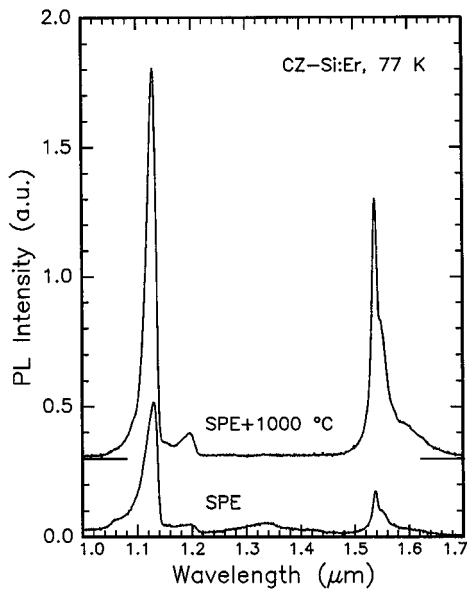


FIG. 53. PL spectra taken at 77 K for Er-implanted CZ-Si (9×10^{14} Er/cm², 250 keV) after SPE at 600 °C and after subsequent annealing at 1000 °C for 15 s. The upper spectrum was shifted upward for clarity. ($\lambda_{\text{pump}} = 514.5$ nm, power = 160 mW, spectral resolution = 6 nm.) From Ref. 106.

in the range 600–1300 °C (15 s) and it was found that annealing at 1000 °C results in the optimum Er PL intensity at 1.54 μm .

b. Er excitation. Erbium may be excited in Si either by direct absorption or through a photocarrier mediated process. To distinguish between the two mechanisms, photoluminescence excitation (PLE) spectroscopy was performed using a Ti-sapphire laser tuned at wavelengths in the range 925–1030 nm. Note that the Si band gap energy at 77 K corresponds to a wavelength of 1063 nm. Figure 54 shows the 1.535 μm luminescence intensity as a function of pump wavelength for the Er-implanted CZ-Si sample (SPE

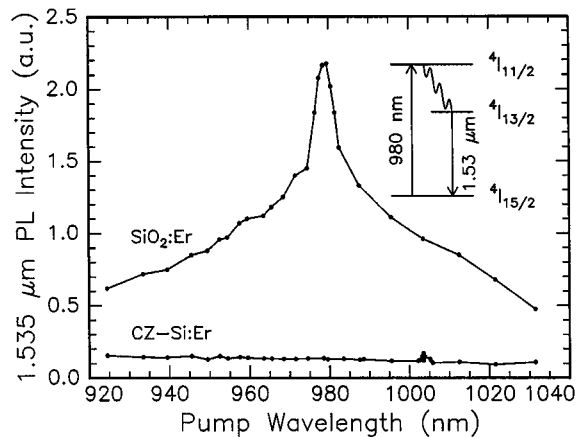


FIG. 54. PL excitation spectrum of Er-implanted CZ-Si (9×10^{14} Er/cm², 250 keV, 600 °C, 15 min + 1000 °C, 15 s) at 77 K and of an Er-implanted SiO₂ film (500 keV, 1.8×10^{15} Er/cm² + 900 °C, 30 min) at 77 K. The PL intensity at 1.53 μm is measured as a function of the pump wavelength. The pump power was 10 mW. The inset shows the Er energy level diagram. (From Ref. 106.)

+1000 °C). The pump power was fixed at 10 mW at each wavelength and the data were taken at 77 K. As can be seen, the Er luminescence signal is a slightly monotonically decreasing function of pump wavelength.

For comparison, a PLE spectrum of an Er-implanted SiO₂ film (500 keV, 1.7×10^{15} Er/cm², annealed at 900 °C for 30 min) is also shown; it was measured using the same pump power of 10 mW. The peak in this spectrum corresponds to the $^4I_{15/2} \rightarrow ^4I_{11/2}$ absorption transition in Er³⁺. After excitation to this level, the ion first decays nonradiatively to the $^4I_{13/2}$ level whereupon it decays to the ground state by emission of a 1.54 μm photon (see inset in Fig. 54). From the fact that the peak at 980 nm is not observed in the spectrum for Er-doped Si, it is concluded that the luminescence from Er in Si is due to a photocarrier mediated process, rather than to direct absorption. This implies that the minority carrier lifetime in the Si host is a crucial factor that determines the Er excitation efficiency. This is important in the analysis of Fig. 53, where it can be seen that the additional 1000 °C anneal increases the band edge luminescence which is a signature of an increase in the minority carrier lifetime. The increased Er luminescence intensity upon annealing is then attributed to a more efficient excitation due to the increased carrier lifetime.

c. Maximum active Er concentration in CZ-Si. In order to study the concentration dependence of the Er luminescence in CZ-Si, samples with four different Er concentrations were made. A surface layer of a CZ-Si(100) wafer was first preamorphized using a 350 keV Si implant at 77 K. Subsequently, 250 keV Er was implanted at fluences of 8×10^{11} , 8×10^{12} , 8×10^{13} , or 8×10^{14} Er/cm². The Er-doped α -Si layers were then all recrystallized by SPE at 600 °C for 15 min and further annealed at 1000 °C for 15 s. SIMS measurements of the Er depth profiles¹⁰⁶ for the four different samples after annealing show trapped Er concentrations in the range of 3×10^{16} – 7×10^{19} Er/cm³.

The Si band edge PL intensity was the same for all four samples, indicating that the minority carrier lifetime was the same in each sample. This shows that the Er ions themselves are *not* the dominant recombination centers for electrical carriers. It implies that only a small fraction of the photogenerated carriers is actually used to excite Er ions, and therefore the internal quantum efficiency for excitation is rather low. The quantum efficiency will be further discussed in Sec. VI A2e.

In order to obtain a measure of the concentration of optically active Er in each sample, the 1.54 μm PL intensity was divided by the PL lifetime for each case. The lifetime varied from 0.7 to 1.1 ms for the four concentrations. The PL intensity/lifetime ratio is plotted in Fig. 55, as a function of Er fluence. All data were taken at 77 K. An initial linear increase with concentration is seen, followed by a leveling off above a fluence of 10^{13} Er/cm².

The data can be analyzed by assuming that there is a maximum Er concentration that can be optically activated in CZ-Si, $[\text{Er}]_{\text{max}}$. Any Er trapped at concentrations above $[\text{Er}]_{\text{max}}$ would then remain inactive. Using measured Er depth profiles for each sample, the total areal density of optically active Er can then be determined by calculating the

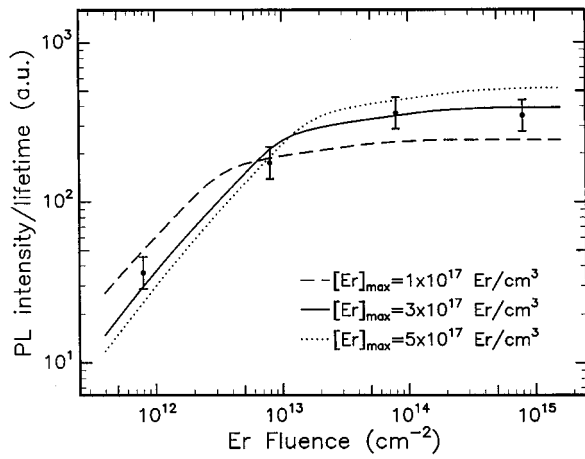


FIG. 55. PL intensity divided by the PL lifetime, which is a relative measure of the total areal density of optically active Er, plotted as a function of the Er implantation fluence at 250 keV. Implants were made into CZ-Si and annealed at 600 °C for 15 min and 1000 °C for 15 s. The lines drawn are calculated from SIMS profiles, using a model in which it was assumed that there is a maximum Er concentration that can be activated in CZ-Si. (From Ref. 106.)

integrated areal density of Er below $[Er]_{\max}$. This areal density should then be proportional to the Er PL data in Fig. 55. Using such a procedure, the details of which are described in Ref. 106, the data in Fig. 55 can be fitted. The continuous lines are results of this procedure using three different values for $[Er]_{\max}$. The best fit for the maximum optically active Er^{3+} concentration is obtained using $[Er]_{\max} = (3 \pm 1) \times 10^{17} \text{ Er/cm}^3$. This is much lower than the maximum Er concentration that can be incorporated into CZ-Si by SPE ($2 \times 10^{20} \text{ Er/cm}^3$).

d. Erbium configuration in Si. EXAFS measurements¹⁰⁴ on Er-implanted CZ-Si have shown that Er forms clusters with four to six O atoms in the first neighbor shell. Using this coordination number and the known O content in the CZ material used above, $(1.7 \pm 0.5) \times 10^{18} \text{ O/cm}^3$, and assuming that in the Er-doped region all Er is bound to oxygen, we can derive a separate estimate of $[Er]_{\max} = 2\text{--}6 \times 10^{17} \text{ Er/cm}^3$. This number is in good agreement with the number found from Fig. 55. One can consider Er a microscopic getter in Si that binds with any O within a relatively large distance. The effective solubility of Er in Si, (Ref. 109) is then determined by the O background level in the wafer. Experiments have shown that the addition of oxygen to Er-implanted CZ-Si can enhance the Er PL intensity.^{108,110,111} This enhancement may then, at least partly, be attributed to an increase in the density of O-coordinated (“optically active”) Er. The addition of O also reduces the PL quenching at elevated temperatures as will be shown.

It is interesting to compare these data on the optical activation of Er in CZ-Si with those on electrical activation. Er exhibits donor behavior in Si and it was found^{112,113} that the maximum carrier concentration in CZ-Si was reached for an Er concentration of $(4\text{--}7) \times 10^{17} \text{ Er/cm}^3$, very similar to the value found above for optical activation. These data suggest that the optically and electrically active Er sites in Si may be the same. Such a correlation between optically and electri-

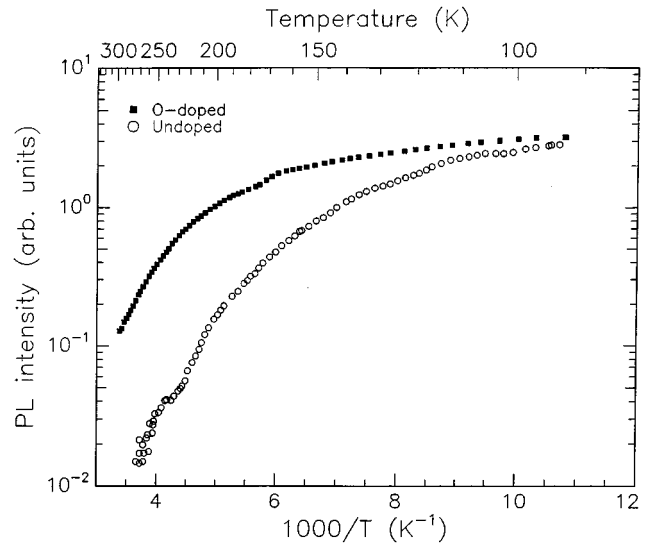


FIG. 56. Arrhenius plot of the 1.54 μm PL intensity for Er-doped CZ-Si ($9 \times 10^{14} \text{ Er/cm}^2$, 250 keV + 600 °C + 900 °C) and Er and O codoped CZ-Si ($1 \times 10^{19} \text{ Er/cm}^3$, $1 \times 10^{20} \text{ O/cm}^3$). ($\lambda_{\text{pump}} = 514.5 \text{ nm}$, power = 200 mW.) From Ref. 108.

cally active sites also follows from O codoping experiments^{112,113} that showed that O enhances both the optically and electrically active fraction.

More measurements will be required to determine the nature of the large optically (and electrically) inactive fraction of Er in CZ-Si. X-ray absorption spectroscopy measurements on samples in which only 1% of the Er is optically active show that all Er is in the trivalent charge state.¹¹⁴ This suggests that the inactive Er has either a very small luminescence quantum efficiency (short luminescence lifetime) or a small excitation efficiency, and therefore does not contribute to the PL spectra.

e. Quantum efficiency. Using the data in Fig. 55 a rough estimate can be made of the internal quantum efficiency for carrier-mediated excitation of Er in Si. Comparing the PL intensities for the Er-doped Si and SiO₂ samples at a pump wavelength of 980 nm and taking into account the known cross sections and collection efficiencies, a lower limit for the internal quantum efficiency of $Q = 3 \times 10^{-6}$ is found.¹⁰⁶ This is a small number, and indicates that the main carrier recombination route is not through Er ions. Clearly, the structural defects remaining after SPE, such as, for example, end-of-range dislocations, dominate the electrical characteristics in these samples. Future work should focus on reduction or passivation of these defects. The quantum efficiency could be further increased if the Er active fraction could be increased. By coimplanting additional oxygen and by increasing the Er depth using MeV implantation energies, the quantum efficiency may possibly be improved to $10^{-3}\text{--}10^{-2}$.

f. Luminescence quenching. Figure 56 shows the temperature dependence of the 1.54 μm PL intensity in Er-implanted CZ-Si.¹⁰⁸ The sample was prepared by 250 keV Er implantation at a fluence of $9 \times 10^{14} \text{ Er/cm}^2$, recrystallized at 600 °C, and subsequently annealed at 900 °C for 15 s. A continuous PL quenching is observed for all temperatures

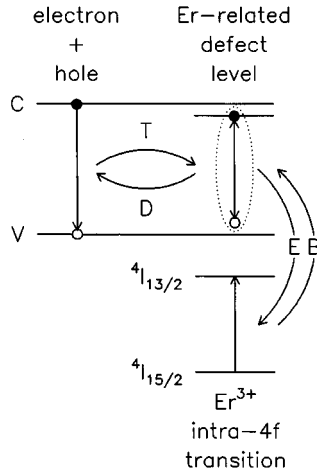


FIG. 57. Model for the excitation and deexcitation of Er in Si.

above 90 K and no measurable signal is found at room temperature.

Measurements were also performed on a sample coimplanted with O. In this case multiple energy Er and O implants were performed on CZ-Si, leading to uniform depth profiles of 1×10^{19} Er/cm² and 1×10^{20} O/cm³ in the depth range between 0.3 and 2 μ m. The temperature dependence for the O codoped sample shows quite different behavior. Up to 150 K a gentle decrease in intensity is found, characterized by an activation energy of up to 20 meV. Above 150 K, a more rapid quenching is observed with an activation energy of roughly 150 meV. A small PL signal can be observed at room temperature.

The temperature quenching can be understood by taking into account an excitation and deexcitation model that is sketched in Fig. 57. It is assumed that an Er-O complex provides a defect level in the Si band gap. Indeed, deep level transient spectroscopy (DLTS) measurements have indicated the presence of such levels.^{112,115} An electron may then be trapped (*T* in Fig. 57) at the level, a hole may subsequently be bound, and if the electron-hole pair recombines, the energy may be transferred through an Auger process to the Er³⁺ ion which then becomes excited (*E* in Fig. 57). The Er ion can then decay by the emission of a 1.54 μ m photon.

There are two possible quenching processes in this model: (1) the bound electron-hole complex may dissociate (*D* in Fig. 57) before the energy is transferred to the Er or (2) the Er ion, once excited, decays by a nonradiative process, for example, a backtransfer process (*B* in Fig. 57) in which the Er decays to the ground state and an electron from the Si valence band is promoted to the defect level. Both quenching processes require the annihilation of one or more phonons and therefore become more probable at high temperature.

In order to study both quenching processes, combined intensity and lifetime measurements were made. The dissociation process will lead to a decrease in PL intensity but will not affect the PL lifetime, while the backtransfer process will decrease both intensity and lifetime. Implants of 1.6×10^{14} 1.46 MeV Er/cm² and 1×10^{15} 750 keV N/cm² were made in CZ-Si(100) and lead to Er and N peak concentra-

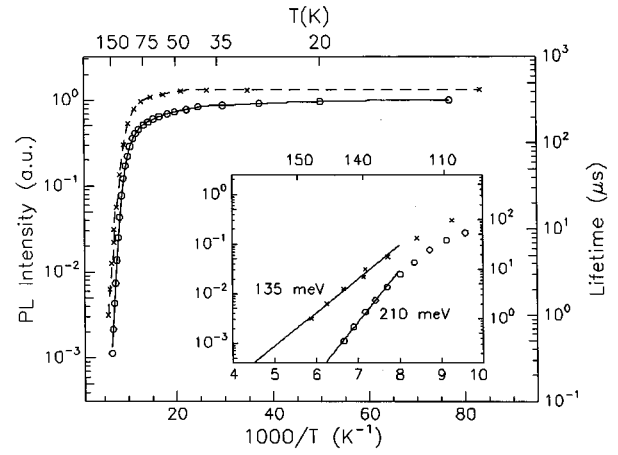


FIG. 58. Arrhenius plot of the integrated Er³⁺ PL intensity (open circles) and lifetime (crosses) for Er and N-implanted CZ-Si (1.6×10^{14} Er/cm² at 1.46 MeV, 1×10^{15} N/cm² at 225 keV, both annealed at 600 °C). The lines through the data are guides for the eye. The inset shows the high temperature data in detail. ($\lambda_{\text{pump}} = 514.5$ nm.) From Ref. 116.

tions after SPE of 5×10^{18} Er/cm³ and 6×10^{19} N/cm³, respectively.¹¹⁶

Figure 58 shows the 1.54 μ m integrated Er³⁺ luminescence intensity as a function of temperature. As can be seen, the PL intensity quenches by three orders of magnitude between 12 and 150 K.

The luminescence lifetime, which is also plotted in Fig. 58, decreases from 420 μ s at 12 K to 1 μ s at 170 K. In fact, the quenching behavior for lifetime and intensity show a similar trend. This shows that lifetime quenching, i.e., a backtransfer process (see Fig. 57), plays a significant role in the intensity quenching.

Priolo *et al.*¹¹⁷ worked out a rate equation model based on the processes indicated in Fig. 57. Including a temperature dependence of the lifetime in this model, the Er PL intensity as a function of temperature is given by

$$I_{\text{PL}}(T) \propto \frac{W_{\text{tr}}}{[1 + A \exp(-E_T/kT)]} \frac{W_{\text{rad}}}{W(T)} N_{\text{Er}},$$

$$W(T) = W_{\text{rad}} + W_B \exp(-E_B/kT), \quad (6)$$

$$A = \frac{\sigma_n N_c}{\sigma_p G_L \tau_c},$$

with $W(T)$ = the measured Er decay rate ($1/\tau$), W_{rad} the radiative decay rate, W_{tr} the transfer rate for process *T* in Fig. 57, σ_n and σ_p the electron and hole trapping cross sections, respectively, N_c the effective density of states at the bottom of the conduction band, G_L the optical carrier generation rate, and τ_c the minority carrier lifetime. E_T is the dissociation activation energy (process *D*, in Fig. 57), and W_B is a prefactor for the backtransfer process that is characterized by an activation energy E_B .

The inset of Fig. 58 shows the quenching behavior for high temperatures in more detail. According to Eq. (6) the slope for the high temperature lifetime data should yield E_{BT} and the slope for the intensity data should yield $E_{BT} + E_T$. Linear fits to the five highest temperature data points

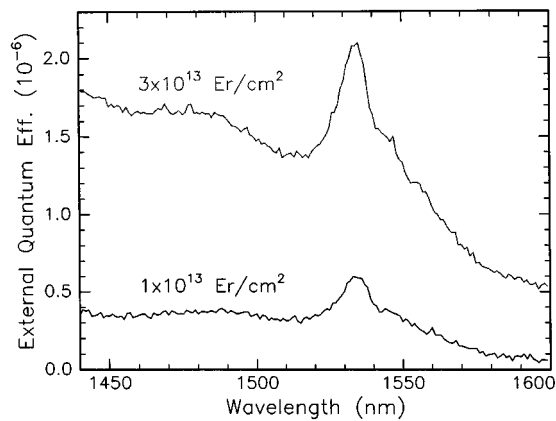


FIG. 59. Spectral response at 300 K of Er-implanted (1×10^{13} Er/cm² or 3×10^{13} Er/cm², 3.5 MeV) PERL crystal Si solar cells, annealed at 1000 and 1060 °C. (From Ref. 118.)

result in $E_B = 135 \pm 5$ meV and $E_B = 75 \pm 10$ meV. Fitting the lifetime data yields an estimate of $W_B = 10^8 - 10^{10} \text{ s}^{-1}$. Below 75 K the intensity shows a very small quenching characterized by an activation energy of 1–10 meV, which is not seen in the lifetime quenching and is attributed to a second detrapping process, possibly the dissociation of the weakly bound hole.

The energy difference between the Si band gap (1.12 eV) and the Er excitation energy (0.81 eV) is around 300 meV. However, in this experiment the observed activation energies add up to only $E_{BT} + E_T = 215 \pm 10$ meV. This suggests that the excitation and deexcitation processes involve different defect levels. Also, it is possible that the levels are broader than indicated in Fig. 57.

In order to study the backtransfer process in more detail, crystal Si solar cells were doped with Er by ion implantation.¹¹⁸ In these experiments, passivated emitter, rear locally (PERL) diffused solar cells were used, which (when not implanted with Er) show the highest efficiency reported for Si solar cells.¹¹⁹ These cells show a near-unity internal quantum efficiency; all carriers generated in the cell are collected by the metal contacts.

Figure 59 shows spectral response measurements at 300 K of PERL solar cells implanted with either 1×10^{13} Er/cm² or 3×10^{13} Er/cm² at 3.5 MeV, and subsequently annealed at 1060 °C for 60 min and 1000 °C for 75 min. In these measurements the short circuit current was measured as a function of the illumination wavelength and converted to quantum efficiency, defined as the number of electron-hole pairs created per absorbed photon. A spectral shape typical for Er absorption is observed for wavelengths around 1.54 μm . The dashed lines indicate a background that is also seen in Si-implanted solar cells and is attributed to implantation defects.¹¹⁸ These data indicate that optically excited Er generates free carriers that are collected in the solar cell. This is direct experimental evidence for the existence of a nonradiative quenching process in which excited Er decays by the generation of a free electron-hole pair at room temperature.

These spectral response measurements can be used to

estimate the efficiency of the backtransfer process, taking into account the Er density and a typical absorption cross section for Er. It was found¹¹⁶ that the probability for deexcitation of an excited Er³⁺ ion at room temperature through a backtransfer process may be as high as 50%.

More measurements are needed to systematically study the relative strength of dissociation and backtransfer processes in Er-implanted Si codoped with different impurities at different concentrations. Comparing the existing data for N-codoped CZ-Si (lifetime quenching by a factor of 500 between 10 and 200 K, see above) and O-codoped CZ-Si (lifetime quenching by a factor of 10),¹⁰⁸ it can already be seen that backtransfer is very much dependent on the impurity and hence local environment of the Er. Future work should focus on impurity and defect engineering to reduce the lifetime quenching.

Recent measurements by Libertino *et al.*¹¹⁵ have shown that an equally important effect of impurity codoping is to remove deep traps in the Si band gap created by the Er implantation itself. Codoped samples will therefore show longer minority carrier lifetimes. This will lead to a reduction in the A parameter in Eq. (6), and hence less temperature quenching of the luminescence.¹¹⁷

3. Electroluminescence

Er-doped p - n diode structures were made¹²⁰ by implanting 5×10^{15} 40 keV B/cm², and 5×10^{15} 2 MeV P/cm² into an epitaxial n -type Si layer on a highly n -type (0.01 $\Omega \text{ cm}$) Si substrate. Constant depth profiles of 1×10^{19} Er/cm³ and 1×10^{20} O/cm³ were made by multiple energy Er and O implantation into the 0.3–2.0 μm depth region. The implanted layer was recrystallized by SPE at 620 °C and subsequently annealed at 900 °C for 30 min in N₂ with a partial O₂ pressure to grow a thin surface oxide passivation layer. Aluminum contacts were made on the front and bottom. The diode area was 0.25 cm². The device showed good electrical characteristics in both forward and reverse bias, with Zener breakdown occurring in reverse bias above -5 V. Details of the device geometry and electrical characteristics are given in Ref. 120.

Figure 60 shows electroluminescence (EL) measurements of the Er-doped diodes measured at room temperature. Measurements are shown both in forward bias (0.7 V, 600 mA) and in reverse bias (-5.2 V, 600 mA).

The EL signal under forward bias is attributed to electron-hole recombination resulting in excitation of Er³⁺. In contrast, the reverse bias signal, which is observed only under breakdown conditions, is attributed to impact excitation of Er³⁺ by hot electrons accelerated across the junction. The electric field in the space charge region under breakdown is estimated to be 1.8 MV/cm. Assuming an electron mean free path of 5 nm, this implies that the electrons can acquire an energy of typically 0.9 eV, sufficient to excite Er³⁺ to the first excited state. The internal quantum efficiency of this Er-doped Si light-emitting diode (LED) is estimated to be 10^{-4} .

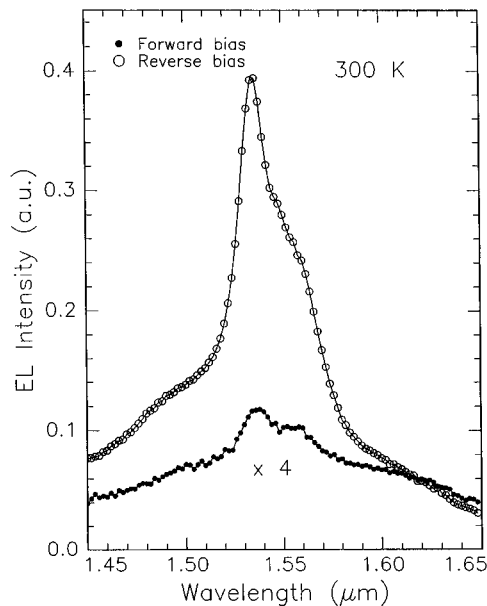


FIG. 60. Room-temperature EL spectra under forward bias and reverse bias for an Er- and O-doped p - n diode structure. The current was 600 mA in both cases. (Spectral resolution=6 nm, from Ref. 120.)

B. Amorphous Si

1. Optical activation

Amorphous silicon (a -Si) is also a promising host material for Er. Being amorphous, it allows one to side step the problem of limited solubility of Er in crystalline Si and to incorporate more of the impurities such as oxygen and carbon that are known to enhance the luminescence. Experiments on Er doping of pure amorphous Si have shown luminescence only at low temperature (77 K).¹²¹ The disadvantage of this material is that its electrical quality is rather poor, so it is therefore more interesting to investigate amorphous materials with better electrical quality. Hydrogenated amorphous Si (a -Si:H) is a well characterized, mature semiconductor that has possibility of being directly deposited on optical materials. Er implantation of two types of a -Si:H will be discussed next; they are made by low-pressure chemical vapor deposition (LPCVD) and plasma enhanced CVD (PECVD).

a. LPCVD a -Si. a -Si:H layers 340 nm thick were deposited¹²² on Si(100) by LPCVD from SiH_4 and N_2O at 620 °C. The H and O contents in these films were 10 at. % and 31 at. %, respectively. This material is sometimes referred to as semi-insulating polycrystalline Si (SIPOS), although the material used in the present experiments had an amorphous structure. Erbium was implanted at 500 keV to a dose of 1×10^{15} Er/cm². The peak Er concentration, at a depth of 150 nm, was 0.2 at. %.

Figure 61 shows a room-temperature PL spectrum for the Er-implanted LPCVD film annealed at 400 °C. The spectrum shows the characteristic Er^{3+} luminescence, peaked at 1.54 μm . Implanted films were also annealed at temperatures below or above 400 °C, but all showed less (PL) intensity than the one annealed at 400 °C. Figure 62(a) shows the temperature dependence of the 1.54 μm PL intensity of this

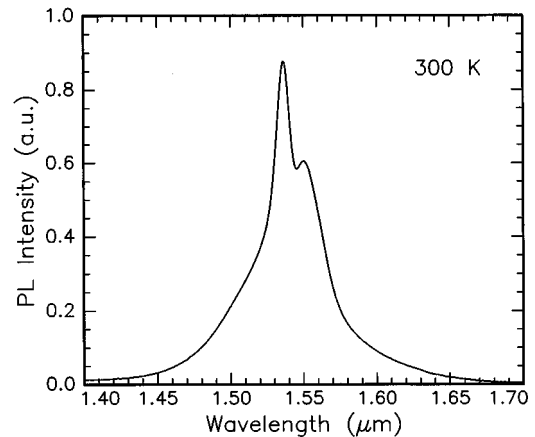


FIG. 61. Room-temperature PL spectrum of Er-implanted (1×10^{15} Er/cm², 500 keV; peak concentration 0.2 at %) LPCVD a -Si:H, annealed at 400 °C. ($\lambda_{\text{pump}} = 515$ nm, spectral resolution=6 nm; from Ref. 122.)

sample (pump power 50 mW). A very weak temperature quenching by only a factor of 3 is observed. For comparison, the quenching in Er-implanted crystal Si samples from Fig. 56 (with and without codoping with 0.2 at. % O, pump power 200 mW) is also shown. Clearly, the amorphous film shows higher PL intensities over the whole temperature range and with much less quenching.

Luminescence lifetime measurements at 1.54 μm were also made. The decay curves showed a double exponential

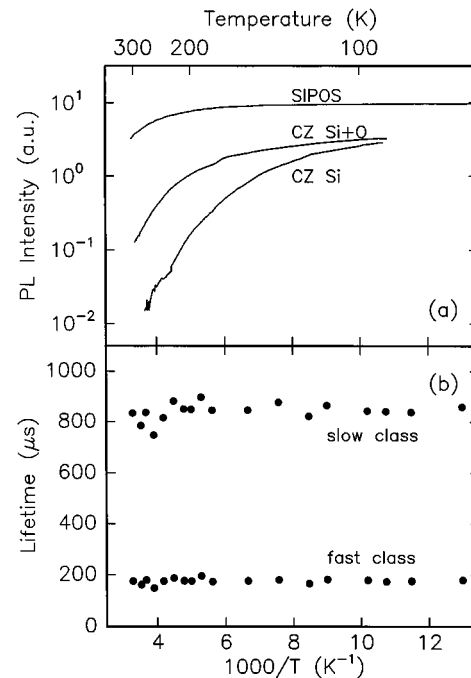


FIG. 62. (a) Arrhenius plot of the 1.54 μm PL intensity of Er-implanted (1×10^{15} Er/cm², 500 keV, peak concentration 0.2 at %, annealed at 400 °C) LPCVD a -Si:H (pump power 50 mW), compared to that for Er-implanted CZ-Si and Er and O coimplanted CZ-Si (pump power 200 mW). (b) Temperature dependence of the two lifetime components in the luminescence decay measurement for LPCVD a -Si:H. ($\lambda_{\text{pump}} = 514.5$ nm; from Ref. 122.)

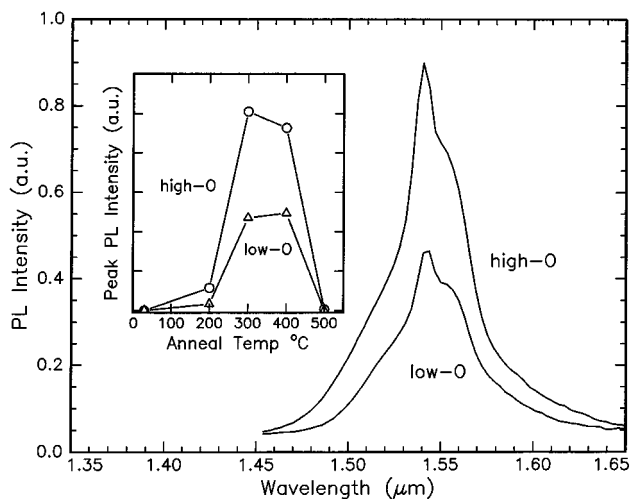


FIG. 63. Room-temperature PL spectra of Er-implanted (4×10^{14} Er/cm², 125 keV, peak concentration 0.2 at. %) PECVD *a*-Si:H (0.3 and 1.3 at. % O), annealed at 400 °C. The inset shows the 1.54 μ m PL intensity as a function of annealing temperature. (From Ref. 124.)

behavior with lifetimes of around 160 and 800 μ s,¹²² independent of temperature in the range 77–300 K, as can be seen in Fig. 62(b). This lifetime behavior is quite different from that of O or N codoped crystal Si which showed a lifetime quenching by a factor of 10 or 500, respectively, between 10 and 200 K (see Figs. 56 and 58).^{108,116}

The small lifetime quenching data for LPCVDs *a*-Si:H indicates that there is no nonradiative deexcitation (process *B* in Fig. 57) of excited Er³⁺ at higher temperatures. This may be associated to the fact that this material, due to its high O content, has a large band gap (2.0 eV),¹²³ and as a result a large energy mismatch gap has to be bridged for a deexcitation process to defect levels near the conduction band. The small (factor of 3) quenching in the intensity measured in Fig. 62 is then attributed to a small decrease in the excitation rate due to carrier detrapping as the temperature is increased. The fact that this effect is small implies that the Er-related level is positioned relatively deep in the forbidden band.

b. PECVD a-Si. *a*-Si:H films were also prepared by PECVD of SiH₄ on glass (Corning 7059) at 230 °C.¹²⁴ The H content in the 250-nm-thick films was 10 at. %, and a background concentration of 0.3 at. % O was also present. Erbium was implanted at 125 keV to a dose of 4×10^{14} Er/cm², corresponding to a peak concentration (at a depth of roughly 35 nm) of 0.2 at. %. In some samples, additional O was implanted at 25 keV to a dose of 7×10^{15} O/cm², resulting in a total O peak concentration of 1.3 at. %, which overlaps with the Er profile.

Figure 63 shows the room-temperature PL spectra of the Er-implanted PECVD *a*-Si:H films annealed at 400 °C displaying characteristic Er³⁺ luminescence at 1.54 μ m. The inset shows the Er³⁺ luminescence intensity at 1.54 μ m as a function of the annealing temperature. As can be seen, samples annealed at 300–400 °C display the optimum Er³⁺ luminescence. No erbium-related luminescence can be observed from either the as-implanted samples nor from the

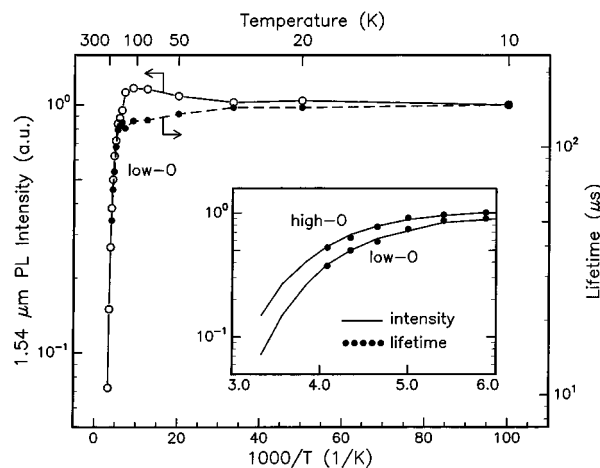


FIG. 64. Arrhenius plot of the normalized, integrated PL intensity (open circles and solid line) and lifetime (solid circles and dashed line) of Er-implanted (4×10^{14} Er/cm², 125 keV) PECVD *a*-Si:H:O (0.3 at. % O) annealed at 400 °C. The inset shows the curves in a smaller temperature range. Data for the high-O sample (1.3 at. % O) are also shown in the inset. (From Ref. 124.)

samples annealed at 500 °C. The increasing and decreasing trends in the inset are attributed to the competing effects of the removal of irradiation-induced defects and of outdiffusion of hydrogen as the annealing temperature is increased.

Figure 64 shows the temperature dependence of both the integrated Er³⁺ PL intensity and the lifetime for the Er-implanted low-O PECVD *a*-Si:H film (0.3 at. % O) annealed at 400 °C. The inset shows the data above 160 K in detail, as well as data for the high-O sample (1.3 at. % O). All intensity data are normalized to the value at 10 K. Between 10 and 110 K, the integrated Er³⁺ PL intensity shows a slight increase as the temperature increases. At the same time, the lifetime decreases. Above 110 K, a 15-fold reduction in the Er³⁺ luminescence intensity is observed as the temperature is increased to 300 K. Up to 250 K, the temperature quenching of the Er³⁺ luminescence intensity correlates well with that of the lifetime (see inset of Fig. 64). No lifetime measurements could be made at temperatures above 250 K as the luminescence lifetime became shorter than the system response time (30 μ s). However, extrapolating the lifetime data to higher temperatures, it becomes clear that most of the intensity quenching above 160 K can be attributed to lifetime quenching. The high-O sample shows less quenching (only a factor of 7 between 10 and 300 K), and again the trend in the intensity is correlated with the change in lifetime.

The lifetime quenching for PECVD *a*-Si:H observed in Fig. 64 indicates that in this material nonradiative deexcitation of Er can take place at elevated temperature. Indeed, this material has a smaller band gap (1.6 eV) than the LPCVD material and as a result the nonradiative deexcitation of an excited Er³⁺ ion may involve a smaller energy mismatch. The magnitude of the lifetime quenching accounts for most of the intensity quenching, which implies that the detrapping rate of carriers is only slightly temperature dependent. This also implies that in the PECVD material the Er-related level is positioned relatively deep in the forbidden band.

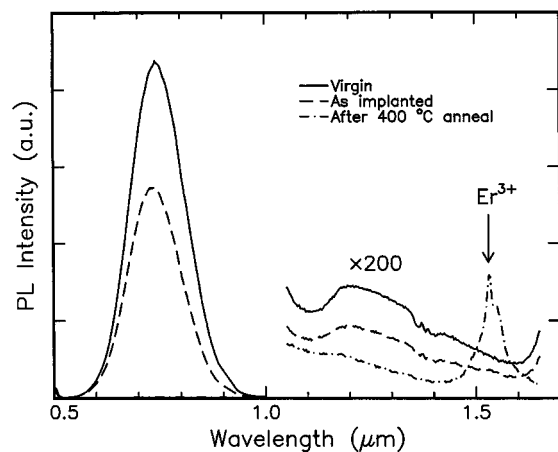


FIG. 65. Room-temperature PL spectra of virgin porous Si and Er-implanted (1×10^{15} Er/cm², 250 keV) porous Si before and after annealing at 400 °C. [$\lambda_{\text{pump}} = 455$ nm, power = 5 mW (spectrum < 1 μm) or 50 mW (spectrum > 1 μm), spectral resolution = 6 nm; from Ref. 129.]

The fact that in both LPCVD and PECVD *a*-Si:H the excitation rate is only slightly temperature dependent (i.e., carrier detrapping is not very efficient) is in contrast to the behavior of Er in crystalline Si, where it was shown that the carrier detrapping effect is important (see Sec. VI Af). The present data also correlate with previous work on III–V and II–VI semiconductors doped with Er (Ref. 125) that has shown the trend that the luminescence quenching is reduced as the band gap is increased.

c. Porous Si. Porous Si (*p*-Si) has been extensively investigated in the past five years since it can quite efficiently emit light under optical excitation, presumably due to a quantum confinement effect in the Si crystal nanograins present in *p*-Si.¹²⁶ It is a disordered material that also contains amorphous regions and high concentrations of oxygen and hydrogen.

It has been suggested that *p*-Si would be a good host for Er since spatial confinement of carriers in the Si nanograins could cause them to recombine near the incorporated Er and thus result in very efficient excitation of Er³⁺ in *p*-Si.^{127,128}

A 5–10- μm -thick *p*-Si layer was produced¹²⁹ by anodic etching of a silicon wafer in a 2:3:5 HF/H₂O/2-propanol solution for 10 min at a current density of 20 mA/cm². The resulting porosity was 65%. The Si:O ratio, as measured by RBS, was 1:1. The *p*-Si film was then implanted with 1×10^{15} Er/cm² at an energy of 250 keV, and annealed in vacuum at 400 °C for 2 h.

Figure 65 shows a room-temperature PL spectrum of the virgin *p*-Si layer and the implanted layer before and after annealing. A 455 nm pump was used. Prior to implantation, the spectrum peaks around 740 nm. In fact, visible luminescence is clearly seen by the naked eye, confirming the good quality of the *p*-Si layer. No Er-related luminescence is seen from the as-implanted sample. However, after annealing at 400 °C, a clear Er-related peak around 1.54 μm is observed.

Additional studies were performed on Er-implanted *p*-Si, including its dependence on annealing temperature, its PL intensity quenching as a function of temperature, and its dependence on excitation wavelength,¹²⁹ and they all showed

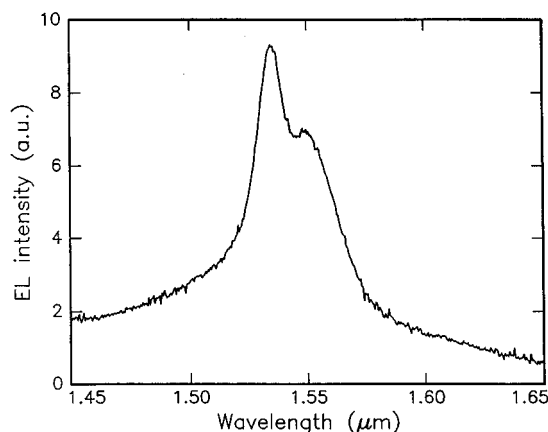


FIG. 66. Room-temperature EL spectrum in reverse bias of an Er-implanted (5×10^{14} Er/cm², 35 keV) LPCVD *a*-Si:H/O/*c*-Si diode structure annealed at 400 °C (−20 V, 260 mA). (From Ref. 130.)

very similar results to those of Er-implanted LPCVD *a*-Si:H/O (see Sec. VI B1a). Given the fact that *p*-Si contains similarly high O and H concentrations as the LPCVD *a*-Si material, this seems plausible. It must then be assumed that—at least in the *p*-Si materials used in the present study—the Er-related luminescence is from Er located in amorphous regions in the porous layer, and is *not* related to quantum confinement effects in the Si nanograins. This is supported by the fact that the annealing behavior of the visible and Er-related luminescence did not show any correlation. In addition, the PL quenching behavior of the visible and Er-related luminescence also showed no correlation.¹²⁹

2. Electroluminescence

Electroluminescence measurements were made on Er-implanted *a*-Si:H/O films made by LPCVD (SIPOS, see above). A *p*-type Si(100) wafer doped with B by ion implantation on both sides was used as a substrate. A 30-nm-thick *a*-Si:H/O sample was then deposited on one side, and implanted with 35 keV Er under an angle 60° off the surface normal, at a total fluence of 5×10^{14} Er/cm². The Er peak concentration was 1.5 at. %. After implantation, the sample was annealed at 400 °C, and metal contacts were deposited. The light was coupled out through a 0.16 mm² hole in the backside contact. Details of the LED geometry are given in Ref. 130.

Figure 66 shows a room-temperature EL spectrum of the diode under reverse bias (−20 V, negative voltage on the Si substrate side) at a current of 260 mA. A clear Er³⁺-related emission around 1.54 μm is observed. No signal was observed in forward bias for this particular diode. Diodes annealed at 500–600 °C did show weak forward bias EL, but these diodes showed much weaker reverse bias EL than the ones annealed at 400 °C.

Detailed analyses were made of the electrical characteristics of the diode.¹³⁰ It was found that in large reverse bias the electric field is shared by the *a*-Si:H/O/Si junction and the Si. For a reverse bias above ≈ 14 V, the field in the Si reaches 1 MV/cm, and breakdown will take place by a combination of avalanche and Zener mechanisms. This results in

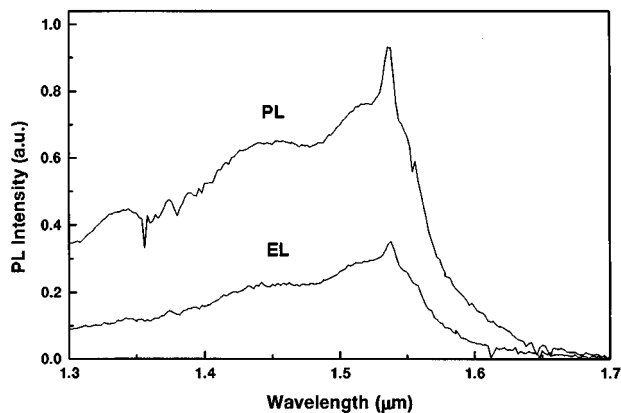


FIG. 67. Room-temperature EL spectrum in forward bias (4.45 V, 19 mA) of an Er-implanted PECVD *a*-Si:H *p-i-n* diode coimplanted with 1.0 at. % O.

the creation of a large density of hot electrons on the Si crystal side of the junction, and the hot electrons are then accelerated towards and into the Er-doped *a*-Si:H,O layer. The Er is then excited through impact excitation. An estimate of the impact excitation cross section was made: $\sigma_i > 6 \times 10^{-16} \text{ cm}^2$ and the internal quantum efficiency of the Er-doped LED was around 10^{-4} .

Electroluminescence measurements were also made on PECVD deposited *a*-Si:H films.¹³¹ A layer structure, consisting of 20-nm-thick *p*-type *a*-Si:H/500 nm intrinsic (*i*) *a*-Si:H/20 nm *n*-type *a*-Si:H was deposited onto a barium-borosilicate glass substrate covered with a transparent conducting oxide layer. Next 700 keV Er was implanted into the layer structure at a fluence of $5 \times 10^{14} \text{ Er/cm}^2$. Oxygen was coimplanted at 80 keV ($3.2 \times 10^{15} \text{ O/cm}^2$) and 120 keV ($5.5 \times 10^{15} \text{ O/cm}^2$), resulting in a roughly constant O concentration of 1.0 at. % at the Er projected range in the middle of the intrinsic layer. The diode structure was annealed in vacuum at 400 °C for 30 min, and Ag contacts were evaporated. The light was coupled out through the transparent conducting layer and the glass substrate.

Figure 67 shows a room-temperature EL spectrum measured under forward bias (4.45 V, 19 mA). A clear Er^{3+} luminescence peak is seen at $1.54 \mu\text{m}$, superimposed on a broad background that is attributed to defect electroluminescence from *a*-Si:H. A PL spectrum measured at a pump power of 40 mW is shown for reference in Fig. 67. It also shows the Er^{3+} luminescence on top of a defect background signal.

VII. OTHER MATERIALS AND OTHER RARE-EARTH IONS

This review paper described the work by the author and collaborators on erbium-implanted thin film photonic materials. Several other groups have contributed to this field of research, and references to the main achievements are given in Sec. VII. Only materials made by ion implantation are discussed. It should be noted that, specifically in the area of optical waveguide synthesis, several techniques other than implantation are also being used.

A. Er-implanted waveguide films

Er implantation of LiNbO_3 for optical purposes was pioneered by Buchal *et al.* Single mode Ti-diffused channel waveguides were made on a 300 keV Er-implanted and annealed LiNbO_3 wafer, and optical amplification was demonstrated.¹³² They also made careful studies of the diffusion of Er implanted in LiNbO_3 ,¹³³ information that was later used in the optimization of Er-indiffused LiNbO_3 waveguide lasers.

Other perovskite-type materials have also been implanted with rare-earth ions: Nd-implanted SrTiO_3 showed characteristic photoluminescence of Nd^{3+} at 1.05–1.08 μm ,¹³⁴ while Tb-implanted $\text{Y}_3\text{Al}_5\text{O}_{12}$ (YAG) showed cathodoluminescence at 544, 590, and 620 nm. Sapphire single crystals implanted with Eu showed photoluminescence at 622 nm, particularly after additional laser annealing.¹³⁵

Si_3N_4 thin films were also doped with Er by ion implantation.^{15,136} This material has a relatively high refractive index ($n = 1.97$), and therefore waveguides with small dimensions and highly confined optical modes can be made. PL from Er^{3+} was observed after annealing and had luminescence lifetimes at $1.54 \mu\text{m}$ of 7 ms at low Er concentration. Combined Er and Yb implantations were performed into silicon oxynitride waveguides. In such codoped waveguides, the aim is to take advantage of the relatively high absorption cross section of the Yb^{3+} ion, which can then resonantly transfer its energy to Er^{3+} .¹³⁷

Cavity quantum electrodynamic effects on the spontaneous emission rate of Er^{3+} were studied by Vredenberg *et al.*,^{138,139} who implanted Er into a Fabry–Pérot microcavity. By varying the thickness of the SiO_2 active layer in the cavity, the cavity resonance was tuned on or off the Er^{3+} emission wavelength. Luminescence lifetimes of 9.8 and 14.8 ms were found for on-resonance and off-resonance cavities, respectively. Due to the high cavity quality factor, the Er^{3+} emission intensity could be significantly enhanced and the spectral width reduced.

Finally, we mention the work by Townsend and co-workers who have used light ion irradiation to modify the refractive index in the near-surface region of virtually any material.¹⁴⁰ Using masked ion implantation, channel waveguides were written in an Er-doped YAG laser crystal, and waveguide lasing was then achieved.¹⁴¹ Ion irradiation serves as a useful tool in making waveguides in materials for which no simpler waveguide fabrication methods (such as diffusion, deposition, or ion exchange) exist.¹⁴²

B. Er-implanted Si

Work on rare-earth-doped semiconductors was pioneered by Ennen *et al.*, who reported in 1983 and in 1985 the first (low temperature) photoluminescence¹⁴³ and electroluminescence¹⁴⁴ spectra of Er in Si that was grown by molecular beam epitaxy with *in situ* ion implantation. Due to the lack of room-temperature emission from Er in Si at that time, this field of study remained silent for several years, until it was re-inspired by the successful experiments on Er implantation into SiO_2 .¹⁵

Groups at AT&T Bell Laboratories and later at Massachusetts Institute of Technology studied the enhancement of the luminescence of Er-implanted Si by codoping with it impurities such as oxygen, nitrogen, fluorine, and carbon,^{111,145} and also studied the solubility¹⁰⁹ and phase diagram of Si-Er,¹⁴⁶ the electrical properties,¹¹² and the quenching behavior of Er in Si.¹⁴⁷ Optimized Er and O doped Si LEDs were made and they showed room-temperature electroluminescence at 1.54 μm .^{147,148} These light-emitting diodes were then integrated into a Si-based waveguide modulator structure, and a modulation frequency of 20 kHz was achieved.¹⁴⁹

Simultaneously, a group at Catania University studied the effect of codoping on the quenching of Er luminescence,^{108,117} and on the electrical properties of the Si host.^{103,117,150} Room-temperature electroluminescence was achieved¹²⁰ as was reported earlier in this article. Recently, this group found that the modulation frequency of the LEDs was not fundamentally limited by the Er^{3+} spontaneous emission rate, as free carriers in the depletion layer of the device cause an effective shortening of the lifetime, presumably due to an Auger quenching effect.^{147,151} This effect may be further optimized and may lead to LED modulation frequencies in the MHz range.

Several other groups have studied the lattice location and site symmetry of Er in crystal Si,^{152,153} IBIEC of Er-doped *a*-Si,¹⁵⁴ the effect of impurity codoping,^{110,155,156} the local environment,¹⁰⁴ excitation mechanisms,¹⁵⁷ as well as the theory of excitation of Er in Si.¹⁵⁸⁻¹⁶¹ It should be noted that the work on Er implantation into Si has also triggered further work on growth using molecular beam epitaxy.¹¹ Room-temperature electroluminescence at 1.54 μm was recently achieved in Si:Er grown by molecular beam epitaxy.¹⁶²

Er doping of *a*-Si was first reported by Oestereich *et al.*¹⁶³ and later by others. Some experiments involve Er doping by implantation,^{121,164} but other techniques have also been used.¹⁶⁵ Finally, the surprising increase in the number of papers published on Er-doped porous Si, many of which can be found in Ref. 11, should be mentioned.

VIII. CONCLUSIONS

In conclusion, the different Er-implanted thin film photonic materials described in this article each have very characteristic optical and structural properties. Each of these can be used in an advantageous way. Optimization of Er-doped silica films may lead to the development of fiber-compatible planar optical waveguide amplifiers. Er-doped silica is also ideally suited for further fundamental studies related to quantum-electrodynamical effects on spontaneous emission. Optimum optical gain performance is observed in Er-implanted Al_2O_3 channel waveguides, with which the world's smallest (1 mm^2) Er-doped optical amplifier, operating at the lowest pump power (9 mW), is made. Efficient cooperative upconversion is observed in Er-implanted Y_2O_3 films, and green, blue, or UV waveguide lasers may be made in this material. In LiNbO_3 , a new method is discovered to incorporate high Er concentrations using rapid thermal annealing. And, Er-doped Si *p-n* diodes show room-

temperature electroluminescence at 1.54 μm . The emission efficiency may be increased by optimization of the local environment of the Er^{3+} .

ACKNOWLEDGMENTS

This work was part of the research program of the Foundation of Research on Matter (FOM) and was made possible by financial support from the Dutch Organization for the Advancement of Research (NWO), The Netherlands Technology Foundation (STW), the IC Technology Program (IOP Electro-Optics) of the Ministry of Economic Affairs, and the ESPRIT program (SCOOP) of the European Community. It is a great pleasure to acknowledge all co-workers who have contributed to the work described in this review article: Edwin Snoeks, Gerlas van den Hoven, Erik Radius, Pieter Kik, Mark Brongersma, Jon Custer, Rosalia Serna, Jung Shin, Michiel de Dood, Lenneke Slooff, Ad Lagendijk, and Frans Saris at FOM-AMOLF, Cor van Dam, Koos van Uffelen, and Meint Smit at the Technical University in Delft, Wilfried van Sark and Arjen Vredenberg at Utrecht University, Paul Alkemade at DIMES in Delft, Tsjerk Hoekstra and Paul Lambeck at the Technical University Twente, Salvo Coffa, Francesco Priolo, Giorgia Franzò, Salvo Lombardo, and Ugo Campisano at the University and CNR-IMETEM in Catania, John Poate, Dale Jacobson, Greg Blonder, Matthew Marcus, and Dave Eaglesham at AT&T Bell Laboratories/Lucent Technologies, Chris Buchal and Martin Fleuster at Research Center, Jülich, and Ben Hendriksen and Mart Diemeer at PTT Research in Leidschendam.

¹ S. Hüfner, *Optical Spectra of Transparent Rare-earth Compounds* (Academic, New York, 1978).

² P. J. Mears, L. Reekie, I. M. Jauncey, and D. N. Payne, *Electron. Lett.* **23**, 1026 (1987).

³ E. Desurvire, R. J. Simpson, and P. C. Becker, *Opt. Lett.* **12**, 888 (1987).

⁴ E. Desurvire, *Sci. Am. (Int. Ed.)* **266**, 96 (1992).

⁵ A. M. Glass, *Phys. Today* **46**, 34 (1993).

⁶ E. Desurvire, *Phys. Today* **47**, 20 (1994).

⁷ R. E. Tench, presented at the OSA Conference on Optical Amplifiers and their Applications, Monterey, CA, 1996.

⁸ N. Bergano, *Optical Amplifiers and their Applications*, 1996 Technical Digest Vol. 11 (Optical Society of America, Washington, DC, 1996), p. 6.

⁹ Recent new results may be found on the following Internet site: <http://www.amolf.nl>

¹⁰ S. Coffa, *Mat. Sci. Eng. Rep.* (to be published).

¹¹ *Rare Earth Doped Semiconductors II*, edited by S. Coffa, A. Polman, and R. N. Schwartz, *Mater. Res. Soc. Symp. Proc.* **422**, (1996).

¹² A. Polman, D. C. Jacobson, D. J. Eaglesham, R. C. Kistler, and J. M. Poate, *J. Appl. Phys.* **70**, 3778 (1991).

¹³ J. P. Biersack and L. J. Haggmark, *Nucl. Instrum. Methods* **174**, 257 (1980).

¹⁴ E. Radius, Ms. thesis, FOM-Institute for Atomic and Molecular Physics, Amsterdam, 1994.

¹⁵ A. Polman, D. C. Jacobson, D. J. Eaglesham, R. C. Kistler, and J. M. Poate, *J. Appl. Phys.* **70**, 3778 (1991).

¹⁶ E. Snoeks, T. Weber, A. Cacciato, and A. Polman, *J. Appl. Phys.* **78**, 4723 (1995).

¹⁷ C. Shi, M. Tan, T. A. Tombrello, *J. Non-Cryst. Solids* **104**, 85 (1988).

¹⁸ U. Katzenkamp, H. Karge, and R. Prager, *Radiat. Eff.* **48**, 31 (1980).

¹⁹ G. W. Arnold and P. Mazzoldi, in *Ion Beam Modification of Insulators*, edited by P. Mazzoldi and G. W. Arnold (Elsevier, Amsterdam, 1987), Chap. 5.

²⁰ A. Polman, D. C. Jacobson, A. Lidgard, J. M. Poate, and G. W. Arnold, *Nucl. Instrum. Methods Phys. Res. B* **59/60**, 1313 (1991).

²¹ A. Polman and J. M. Poate, *J. Appl. Phys.* **73**, 1669 (1993).

²² E. P. Eernisse and C. B. Norris, *J. Appl. Phys.* **45**, 5196 (1974).

- ²³ S. Chengru, M. Tan, and T. A. Tombrello, *J. Non-Cryst. Solids* **104**, 85 (1988).
- ²⁴ R. A. B. Devine, *Nucl. Instrum. Methods Phys. Res. B* **46**, 244 (1990).
- ²⁵ M. Antonini, P. Camagni, P. N. Gibson, and A. Manara, *Radiat. Eff.* **65**, 41 (1982).
- ²⁶ W. Primak and R. Kampwirth, *J. Appl. Phys.* **39**, 5651 (1968).
- ²⁷ H. Matzke, in Ref. 19, p. 501.
- ²⁸ D. L. Griscom and E. J. Friebele, *Radiat. Eff.* **65**, 63 (1982).
- ²⁹ S. Karasawa, N. Horiuchi, and T. Takada, *Nucl. Instrum. Methods Phys. Res. B* **47**, 404 (1990).
- ³⁰ H. Böck, J. Siehs, and N. Vana, *Radiat. Eff.* **65**, 75 (1982).
- ³¹ C. H. Henry, G. E. Blonder, and R. F. Kazarinov, *J. Lightwave Technol.* **7**, 1530 (1989).
- ³² R. V. Ramaswamy and R. Srivastava, *J. Lightwave Technol.* **6**, 984 (1988).
- ³³ E. Snoeks, G. N. van den Hoven, and A. Polman, *J. Appl. Phys.* **73**, 8179 (1993).
- ³⁴ E. Snoeks, Ph.D. thesis, FOM-Institute for Atomic and Molecular Physics, Amsterdam, 1995.
- ³⁵ W. J. Miniscalco, *J. Lightwave Technol.* **9**, 234 (1991).
- ³⁶ J. C. Wright, in *Radiationless Processes in Molecules and Condensed Phases*, edited by F. K. Fong (Springer, Heidelberg, 1976), Chap. 4.
- ³⁷ F. P. Auzel, in *Radiationless Processes*, edited by B. DiBartolo (Plenum, New York, 1980).
- ³⁸ E. Snoeks, P. G. Kik, and A. Polman, *Opt. Mater.* **5**, 159 (1996).
- ³⁹ Y. Yan, A. J. Faber, and H. de Waal, *J. Non-Cryst. Solids* **181**, 283 (1995).
- ⁴⁰ A. J. Bruce, W. A. Reed, A. E. Neeves, L. R. Copeland, W. H. Grodkiewicz, and A. Lidgard, *Mater. Res. Soc. Symp. Proc.* **244**, 157 (1992).
- ⁴¹ F. F. Morehead and B. L. Crowder, *Radiat. Eff.* **6**, 27 (1970).
- ⁴² D. L. Griscom, G. H. Sigel, Jr., and G. L. Ginther, *J. Appl. Phys.* **47**, 960 (1976).
- ⁴³ M. A. Marcus and A. Polman, *J. Non-Cryst. Solids* **136**, 260 (1991).
- ⁴⁴ E. Snoeks, G. N. van den Hoven, A. Polman, B. Hendriksen, M. B. J. Diemeer, and F. Priolo, *J. Opt. Soc. Am. B* **12**, 1470 (1995).
- ⁴⁵ N. H. G. Baken, M. B. J. Diemeer, J. M. van Splunter, and H. Blok, *J. Lightwave Technol.* **8**, 576 (1990).
- ⁴⁶ L. Cognolato, D. de Bernardi, M. Ferraris, A. Gnazzo, S. Morasca, and D. Scarano, *CSELT Tech. Rep.* **XIX**, 277 (1991); W. J. Miniscalco, *J. Lightwave Technol.* **9**, 234 (1991).
- ⁴⁷ J. J. G. M. van der Tol, J. W. Verhoof, M. B. J. Diemeer, and E. C. M. Pennings, *Electron. Lett.* **27**, 379 (1991).
- ⁴⁸ A. M. Vredenberg (private communication).
- ⁴⁹ J. Nilsson, P. Blixt, B. Jaskorzynska, and J. Babonas, *J. Lightwave Technol.* **13**, 341 (1995).
- ⁵⁰ J. E. Román, M. Hempstead, C. C. Ye, P. Camy, P. Laborde, and C. Lermينياux, *Appl. Phys. Lett.* **67**, 470 (1995).
- ⁵¹ E. Snoeks, G. N. van den Hoven, and A. Polman, *IEEE J. Quantum Electron.* **32**, 1680 (1996).
- ⁵² M. J. F. Digonnet, *IEEE J. Quantum Electron.* **26**, 1788 (1990).
- ⁵³ E. Snoeks, A. Lagendijk, and A. Polman, *Phys. Rev. Lett.* **74**, 2459 (1995).
- ⁵⁴ M. K. Smit, Ph.D. thesis, Delft University of Technology, The Netherlands, 1991.
- ⁵⁵ E. C. M. Pennings, G. H. Manhoudt, and M. K. Smit, *Electron. Lett.* **24**, 998 (1998).
- ⁵⁶ C. W. White, C. J. McHargue, P. S. Sklad, L. A. Boatner, and G. C. Farlow, *Mater. Sci. Rep.* **4**, 41 (1989).
- ⁵⁷ Y. Chen, M. M. Abraham, and D. F. Pedraza, *Nucl. Instrum. Methods Phys. Res. B* **59/60**, 1163 (1991).
- ⁵⁸ M. K. Smit, G. A. Acket, and C. J. van der Laan, *Thin Solid Films*, *Electron. Opt.* **138**, 171 (1986).
- ⁵⁹ G. N. van den Hoven, E. Snoeks, A. Polman, C. van Dam, J. W. M. van Uffelen, and M. K. Smit, *Appl. Phys. Lett.* **62**, 3065 (1993).
- ⁶⁰ G. N. van den Hoven, Ph.D. thesis, FOM-Institute for Atomic and Molecular Physics, Amsterdam, 1996.
- ⁶¹ D. E. McCumber, *Phys. Rev. A* **136**, 954 (1964).
- ⁶² W. J. Miniscalco and R. S. Quimby, *Opt. Lett.* **16**, 258 (1991).
- ⁶³ G. N. van den Hoven, J. A. van der Elksen, A. Polman, C. van Dam, J. W. M. van Uffelen, and M. K. Smit, *Appl. Opt.* (in press).
- ⁶⁴ W. L. Barnes, R. I. Laming, E. J. Tarbox, and P. R. Morkel, *IEEE J. Quantum Electron.* **27**, 1004 (1991).
- ⁶⁵ G. N. van den Hoven, E. Snoeks, A. Polman, C. van Dam, J. W. M. van Uffelen, and M. K. Smit, *J. Appl. Phys.* **79**, 1258 (1995).
- ⁶⁶ H. Schober, D. Strauch, and B. Dörner, *Z. Phys. B* **92**, 273 (1993).
- ⁶⁷ S. A. Pollack and D. B. Chang, *J. Appl. Phys.* **64**, 2885 (1988).
- ⁶⁸ T. H. Hoekstra, P. V. Lambeck, H. Albers, and Th. J. A. Popma, *Electron. Lett.* **29**, 581 (1993).
- ⁶⁹ T. H. Hoekstra, Ph.D. thesis, University of Twente, The Netherlands, 1994.
- ⁷⁰ W. F. Krupke, *Phys. Rev.* **145**, 325 (1966).
- ⁷¹ H. Schober, D. Strauch, and B. Dörner, *Z. Phys. B* **92**, 273 (1993).
- ⁷² A. J. Silversmith, W. Lenth, and R. M. Macfarlane, *Appl. Phys. Lett.* **51**, 1977 (1987).
- ⁷³ S. A. Pollack and D. B. Chang, *J. Appl. Phys.* **64**, 2885 (1988).
- ⁷⁴ D. C. Yeh, W. A. Sibley, I. Schneider, R. S. Afzal, and I. Aggarwal, *J. Appl. Phys.* **69**, 1648 (1991).
- ⁷⁵ P. Xie and S. C. Rand, *Opt. Lett.* **17**, 1198 (1992).
- ⁷⁶ M. P. Hehlen, G. Frei, and H. U. Güdel, *Phys. Rev. B* **50**, 16 264 (1994).
- ⁷⁷ A. C. Tropper, J. N. Carter, R. D. T. Lauder, D. C. Hanna, S. T. Davey, and D. Szebesta, *J. Opt. Soc. Am. B* **11**, 886 (1994).
- ⁷⁸ M. Lui, R. A. Macfarlane, D. Yap, and D. Lederman, *Electron. Lett.* **29**, 172 (1993).
- ⁷⁹ L. Zhang, P. D. Townsend, P. J. Chandler, and A. J. Silversmith, *Electron. Lett.* **30**, 1063 (1994).
- ⁸⁰ G. N. van den Hoven, A. Polman, C. van Dam, J. W. M. van Uffelen, and M. K. Smit, *Appl. Phys. Lett.* **68**, 1886 (1996).
- ⁸¹ L. B. Soldano and E. C. M. Pennings, *J. Lightwave Technol.* **13**, 615 (1995), and references therein.
- ⁸² G. N. van den Hoven, A. Polman, C. van Dam, J. W. M. van Uffelen, and M. K. Smit, *Opt. Lett.* **21**, 577 (1996).
- ⁸³ G. Nykolak, M. Haner, P. C. Becker, J. Shmulovich, and Y. H. Wong, *IEEE Photonics Technol. Lett.* **5**, 1185 (1993).
- ⁸⁴ K. Hattori, T. Kitagawa, M. Oguma, Y. Ohmori, and M. Horiguchi, *Electron. Lett.* **30**, 856 (1994).
- ⁸⁵ M. Hempstead, J. E. Román, C. C. Ye, J. S. Wilkinson, P. Camy, P. Laborde, and C. Lermينياux, *Proceedings of the 7th European Conference on Integrated Optics, Delft, April 1995*, p. 233.
- ⁸⁶ D. Barbier, P. Gastaldo, B. Hyde, J. M. Jouanno, and A. Kevorkian, in Ref. 85, p. 241.
- ⁸⁷ E. C. M. Pennings, R. J. Deri, A. Scherer, R. Bhat, T. R. Hayes, N. C. Andreadakis, M. K. Smit, L. B. Soldano, and R. J. Hawkins, *Appl. Phys. Lett.* **59**, 1926 (1991).
- ⁸⁸ R. Adar, C. H. Henry, R. F. Kazarinov, R. C. Kistler, and G. R. Weber, *J. Lightwave Technol.* **10**, 46 (1992).
- ⁸⁹ R. M. Jenkins, J. M. Heaton, D. R. Wight, J. T. Parker, J. C. H. Birbeck, G. W. Smith, and K. P. Hilton, *Appl. Phys. Lett.* **64**, 684 (1994).
- ⁹⁰ M. Bachmann, P. A. Besse, and H. Melchior, *Appl. Opt.* **33**, 3905 (1994).
- ⁹¹ E. Yablonoitch, *J. Opt. Soc. Am. B* **11**, 283 (1993).
- ⁹² R. Brinkmann, W. Sohler, and H. Suche, *Electron. Lett.* **27**, 415 (1991).
- ⁹³ P. Becker, R. Brinkmann, M. Dinand, W. Sohler, and H. Suche, *Appl. Phys. Lett.* **61**, 1257 (1992).
- ⁹⁴ M. Fleuster, Ch. Buchal, E. Snoeks, and A. Polman, *Appl. Phys. Lett.* **65**, 225 (1994).
- ⁹⁵ M. Fleuster, Ch. Buchal, E. Snoeks, and A. Polman, *J. Appl. Phys.* **75**, 173 (1994).
- ⁹⁶ M. Fleuster, Ph.D. thesis, Forschungszentrum Jülich, Jülich, Germany, 1994.
- ⁹⁷ L. Rebouta, M. F. da Silva, J. C. Soares, J. A. Sanz-Garcia, E. Dieguez, and F. Augullo-Lopez, *Nucl. Instrum. Methods Phys. Res. B* **64**, 189 (1992).
- ⁹⁸ T. Gog, M. Griebenow, and G. Materlik, *Phys. Lett. A* **181**, 417 (1993).
- ⁹⁹ Y.-H. Xie, E. A. Fitzgerald, and Y. J. Mii, *J. Appl. Phys.* **70**, 3223 (1991).
- ¹⁰⁰ A. Polman, J. S. Custer, E. Snoeks, and G. N. van den Hoven, *Appl. Phys. Lett.* **62**, 507 (1993).
- ¹⁰¹ J. S. Custer, A. Polman, and H. M. van Pinxteren, *J. Appl. Phys.* **75**, 2809 (1994).
- ¹⁰² A. Polman, J. S. Custer, P. M. Zagwijn, A. M. Molenbroek, and P. F. A. Alkemade, *J. Appl. Phys.* **81**, 150 (1997).
- ¹⁰³ S. Coffa, F. Priolo, G. Franzò, V. Bellani, A. Carnera, and C. Spinella, *Phys. Rev. B* **11**, 782 (1993).
- ¹⁰⁴ D. L. Adler, D. C. Jacobson, D. J. Eaglesham, M. A. Marcus, J. L. Benton, J. M. Poate, and P. H. Citrin, *Appl. Phys. Lett.* **61**, 2181 (1992).
- ¹⁰⁵ J. S. Custer, A. Polman, E. Snoeks, and G. N. van den Hoven, *Mater. Res. Soc. Symp. Proc.* **301**, 101 (1993).
- ¹⁰⁶ A. Polman, G. N. van den Hoven, J. S. Custer, J. H. Shin, R. Serna, and P. F. A. Alkemade, *J. Appl. Phys.* **77**, 1256 (1995).
- ¹⁰⁷ G. Davies, *Phys. Rep.* **176**, 83 (1989).

- ¹⁰⁸ S. Coffa, G. Franzò, F. Priolo, A. Polman, and R. Serna, *Phys. Rev. B* **49**, 16 313 (1994).
- ¹⁰⁹ D. J. Eaglesham, J. Michel, E. A. Fitzgerald, D. C. Jacobson, J. M. Poate, J. L. Benton, A. Polman, Y.-H. Xie, and L. C. Kimerling, *Appl. Phys. Lett.* **58**, 2797 (1991).
- ¹¹⁰ P. N. Favenec, H. L'Haridon, D. Moutonnet, M. Salvi, and M. Gauneau, *J. Appl. Phys.* **29**, L524 (1990).
- ¹¹¹ J. Michel, J. L. Benton, R. F. Ferrante, D. C. Jacobson, D. J. Eaglesham, E. A. Fitzgerald, Y.-H. Xie, J. M. Poate, and L. C. Kimerling, *J. Appl. Phys.* **70**, 2672 (1991).
- ¹¹² J. L. Benton, J. Michel, L. C. Kimerling, D. C. Jacobson, Y.-H. Xie, D. J. Eaglesham, E. A. Fitzgerald, and J. M. Poate, *J. Appl. Phys.* **70**, 2667 (1991).
- ¹¹³ F. Priolo, S. Coffa, G. Franzò, C. Spinella, A. Carnera, and V. Bellani, *J. Appl. Phys.* **74**, 4936 (1993).
- ¹¹⁴ J. B. Goedkoop and A. Polman (unpublished).
- ¹¹⁵ S. Libertino, S. Coffa, G. Franzò, and F. Priolo, *J. Appl. Phys.* **78**, 3867 (1995).
- ¹¹⁶ P. G. Kik, M. J. A. de Dood, K. Kikoin, and A. Polman, *Appl. Phys. Lett.* **70**, 1721 (1997).
- ¹¹⁷ F. Priolo, G. Franzò, S. Coffa, A. Polman, S. Libertino, R. Barklie, and D. Carey, *J. Appl. Phys.* **78**, 3874 (1995).
- ¹¹⁸ M. J. Keevers, F. W. Saris, G. C. Zhang, J. Zhao, M. A. Green, and R. Elliman, *Proceedings of the 13th European Photovoltaic Solar Energy Conference, Nice, October 1995*, p. 1215.
- ¹¹⁹ A. Wang, J. Zhao, and M. A. Green, *Appl. Phys. Lett.* **57**, 602 (1990).
- ¹²⁰ G. Franzò, F. Priolo, S. Coffa, A. Polman, and A. Carnera, *Appl. Phys. Lett.* **64**, 2235 (1994).
- ¹²¹ J. S. Custer, E. Snoeks, and A. Polman, *Mater. Res. Soc. Symp. Proc.* **235**, 51 (1992).
- ¹²² G. N. van den Hoven, Jung H. Shin, A. Polman, S. Lombardo, and S. U. Campisano, *J. Appl. Phys.* **78**, 2642 (1995).
- ¹²³ G. Compagnini, S. Lombardo, R. Reitano, and S. U. Campisano, *J. Mater. Res.* **10**, 885 (1995).
- ¹²⁴ J. H. Shin, R. Serna, G. N. van den Hoven, A. Polman, W. G. J. H. M. van Sark, and A. M. Vredenberg, *Appl. Phys. Lett.* **68**, 997 (1996).
- ¹²⁵ P. N. Favenec, H. L'Haridon, D. Moutonnet, M. Salvi, and M. Gauneau, *Mater. Res. Soc. Symp. Proc.* **301**, 181 (1993).
- ¹²⁶ L. T. Canham, *Appl. Phys. Lett.* **57**, 1046 (1990).
- ¹²⁷ F. Namavar, *III-V Rev.* **7**, 10 (1994).
- ¹²⁸ T. Kimura, A. Yokoi, H. Horiguchi, R. Saito, T. Ikoma, and A. Sato, *Appl. Phys. Lett.* **65**, 983 (1994).
- ¹²⁹ J. H. Shin, G. N. van den Hoven, and A. Polman, *Appl. Phys. Lett.* **66**, 2379 (1995).
- ¹³⁰ S. Lombardo, S. U. Campisano, G. N. van den Hoven, and A. Polman, *J. Appl. Phys.* **77**, 6504 (1995).
- ¹³¹ L. H. Slooff, Ms. thesis, FOM-Institute for Atomic and Molecular Physics, Amsterdam, 1996.
- ¹³² Ch. Buchal, R. Brinkmann, W. Sohler, and H. Suche, *Mater. Res. Soc. Symp. Proc.* **201**, 307 (1991).
- ¹³³ Ch. Buchal and S. Mohr, *J. Mater. Res.* **6**, 134 (1991).
- ¹³⁴ M. G. Tenner, Y. A. R. R. Kessener and M. H. F. Overwijk, *Nucl. Instrum. Methods Phys. Res. B* **80/81**, 1185 (1993).
- ¹³⁵ N. Can, P. D. Townsend, D. E. Hole, and C. N. Afonso, *J. Appl. Phys.* **78**, 6737 (1995).
- ¹³⁶ O. Lumholt, G. Grand, H. Bernas, J. Chaumont, and S. Valette, *Proceedings of the European Conference on Optical Communication, September 1992*.
- ¹³⁷ A. V. Chelnokov, J.-M. Lourtioz, Ph. Boucard, H. Bernas, J. Chaumont, and T. Plowman, *Electron. Lett.* **31**, 636 (1995).
- ¹³⁸ A. M. Vredenberg, N. E. J. Hunt, E. F. Schubert, D. C. Jacobson, J. M. Poate, and G. J. Zydzik, *Phys. Rev. Lett.* **71**, 517 (1993).
- ¹³⁹ E. F. Schubert, A. M. Vredenberg, N. E. J. Hunt, Y. H. Wong, P. C. Becker, J. M. Poate, D. C. Jacobson, L. C. Feldman, and G. J. Zydzik, *Appl. Phys. Lett.* **61**, 1381 (1992).
- ¹⁴⁰ P. D. Townsend, *Nucl. Instrum. Methods Phys. Res. B* **65**, 243 (1992).
- ¹⁴¹ S. J. Field, D. C. Hanna, D. P. Shephard, A. C. Tropper, P. J. Chandler, P. D. Townsend, and L. Zhang, *IEEE J. Quantum Electron.* **27**, 428 (1991).
- ¹⁴² See for example, P. D. Townsend, *Optical Effects of Ion Implantation* (Cambridge University Press, Cambridge, 1994).
- ¹⁴³ H. Ennen, J. Schneider, G. Pomrenke, and A. Axmann, *Appl. Phys. Lett.* **43**, 943 (1983).
- ¹⁴⁴ H. Ennen, G. Pomrenke, A. Axmann, K. Eisele, W. Haydl, and J. Schneider, *Appl. Phys. Lett.* **46**, 381 (1985).
- ¹⁴⁵ J. Michel, F. Y. G. Ren, B. Zheng, D. C. Jacobson, J. M. Poate, and L. C. Kimerling, *Mater. Sci. Forum* **143-147**, 707 (1994).
- ¹⁴⁶ F. Y. G. Ren, J. Michel, Q. Sun-Paduan, B. Zheng, H. Kitigawa, C. C. Jacobson, J. M. Poate, and L. C. Kimerling, *Mater. Res. Soc. Symp. Proc.* **301**, 87 (1996).
- ¹⁴⁷ J. Palm, F. Gan, B. Zheng, J. Michel, and L. C. Kimerling, *Phys. Rev. B* **54**, 17 603 (1996).
- ¹⁴⁸ B. Zheng, J. Michel, F. Y. G. Ren, L. C. Kimerling, D. C. Jacobson, and J. M. Poate, *Appl. Phys. Lett.* **64**, 2842 (1994).
- ¹⁴⁹ J. Michel, *Mater. Res. Soc. Symp. Proc.* **422**, 317 (1996).
- ¹⁵⁰ S. Libertino, S. Coffa, F. Priolo, and G. Franzò, *Mater. Res. Soc. Symp. Proc.* **422**, 113 (1996).
- ¹⁵¹ S. Coffa, G. Franzò, and F. Priolo, *Appl. Phys. Lett.* **69**, 2077 (1996).
- ¹⁵² H. Przybylinska, G. Hendorfer, M. Bruckner, L. Palmetschofer, and W. Jantsch, *Appl. Phys. Lett.* **66**, 490 (1995).
- ¹⁵³ W. Jantsch, C. Skierbiszewski, and L. Palmetschofer, *Mater. Res. Soc. Symp. Proc.* **422**, 101 (1996).
- ¹⁵⁴ F. Fortuna, P. Nédellec, M. O. Ruault, H. Bernas, X. W. Lin, and P. Boucaud, *Nucl. Instrum. Methods Phys. Res. B* **106**, 206 (1995).
- ¹⁵⁵ P. Liu, J. P. Zhang, R. J. Wilson, G. Curello, S. S. Rao, and P. L. F. Hemment, *Appl. Phys. Lett.* **66**, 3158 (1995).
- ¹⁵⁶ A. J. Kenyon, P. F. Trwoga, M. Federighi, and C. W. Pitt, *J. Phys., Condens. Matter.* **6**, L319 (1994).
- ¹⁵⁷ T. Gregorkiewicz, I. Tsimperides, and C. A. J. Ammerlaan, *Mater. Res. Soc. Symp. Proc.* **422**, 207 (1996).
- ¹⁵⁸ S. Schmitt-Rink, C. M. Varma, and A. F. J. Levi, *Phys. Rev. Lett.* **66**, 2782 (1991).
- ¹⁵⁹ M. Needles, M. Schlüter, and M. Lannoo, *Phys. Rev. B* **47**, 15533 (1993).
- ¹⁶⁰ I. N. Yassievich and L. C. Kimerling, *Semicond. Sci. Technol.* **8**, 718 (1993).
- ¹⁶¹ C. Delerue and M. Lannoo, *Mater. Sci. Forum* **143-147**, 699 (1994).
- ¹⁶² J. Stimmer, A. Reittinger, J. F. Nützel, G. Abstreiter, H. Holzbrecher, and Ch. Buchal, *Appl. Phys. Lett.* **68**, 3290 (1996).
- ¹⁶³ T. Oestereich, C. Swiatowski, and I. Broser, *Appl. Phys. Lett.* **56**, 446 (1990).
- ¹⁶⁴ M. Kechouane, N. Beldi, T. Mohammed-Brahim, H. L'Haridon, M. Salvi, and M. Gauneau, *Mater. Res. Soc. Symp. Proc.* **301**, 133 (1993).
- ¹⁶⁵ M. S. Bresler, O. B. Gusev, V. Kh. Kudoyarova, A. N. Kuznetsov, P. E. Pak, E. I. Terukov, I. N. Yassievich, and B. P. Zakharchenya, *Appl. Phys. Lett.* **67**, 3599 (1995).